Hellenic Journal of Nuclear Medicine

The Journal of the Hellenic Society of Nuclear Medicine
Aristotelous 24A, PC 546 23, Thessaloniki, Macedonia, Greece

The 1st hellenic journal of nuclear medicine

WEB SITE: http://www.nuclmed.gr, e-mail: hjnm@nuclmed.gr
Facebook: https://www.facebook.com/eepigr, Instagram: https://www.instagram.com/eletpiia/

Indexed/abstracted by: MEDLINE, Science Citation Index Expanded, Journal Citation Reports/Science Edition, EMBASE, Thomson-Reuters, Scopus Info and Index Copernicus. Listed by the International Centre for Scientific Research

Editor in Chief: T. Kalathas

Co-editors: V. Chatzipavlidou, Thessaloniki - C. Anagnostopoulos, Athens - S. Frangos, Cyprus - T. Spyridonidis, Patra

Printed by
LK Digital Printing, 27, Mitropoleos Str., P.C. 54624, tel: +30 2310 236149, e-mail: graphic@lkprinting.gr

The Board of the Hellenic Society of Nuclear Medicine-Thessaloniki (2024-2026)
President: V. Chatzipavlidou, Vice President: I. Iakovou, Secretary: E. Giannoula, Treasurer: T. Kalathas, Members: N. Papadopoulos

Subscription for 2025-For 3 issues of HJNM postage included-Does not refer to Supplements

Members of the H.S.N.M. with annual subscription	30€	Students:	20€
Non-members of the Hell. Soc. Nucl. Med.:	50€	Single PDF article copywrite:	20€
Institutions - Libraries:	200€	For each printed Supplement:	60€

To the Bank Account of the Hellenic Society of Nuclear Medicine, in ALPHA BANK:

IBAN:GR2001404740474002002002777, BIC:CRBAGRAAXXX

For Instructions to Authors please refer to: www.nuclmed.gr ⟶ Instructions to Authors

Authors **are responsible for the integrity and accuracy of their paper**

Study of serum vitamin D levels in patients with diabetic polyneuropathy using radioimmunoassay method

Anastasia Pistola[1] BS,
Evangelos Karathanos[2] MD,
Theocharis Konstantinidis[3] MD,
Dimitrios Papazoglou[4] MD,
Christina Tsigalou[5] MD,
Athanasios Zissimopoulos[1] MD

1. Nuclear Medicine Department, University General Hospital of Alexandroupolis
2. Nuclear Medicine Department, Sotiria Hospital, Athens.
3. School of Medicine Democritus University of Thrace, Medical Biopathology Lab. University General Hospital of Alexandroupolis
4. School of Medicine Democritus University of Thrace, 2nd Department of Internal Medicine University General Hospital of Alexandroupolis
5. School of Medicine Democritus University of Thrace, Laboratory of Hygiene and Environmental Protection

Keywords: 25(OH)D
- Diabetic polyneuropathy
- Type 2 diabetes
- Radioimmunoassay

Corresponding author:
Anastasia Pistola BS,
Nuclear Medicine Department,
University General Hospital of
Alexandroupolis, Greece
anasia3@gmail.com

Received:
23 Jun 2025
Accepted revised:
10 Jul 2025

Abstract

Objective: Diabetic polyneuropathy (DPN) is a common and disabling complication of type 2 diabetes mellitus (T2DM). Vitamin D deficiency has been implicated as a potential modifiable risk factor. This study aimed to investigate the relationship between serum 25-hydroxyvitamin D [25(OH)D] levels and DPN using the radioimmunoassay (RIA) method. **Subjects and Methods:** One hundred twenty T2DM patients (80 with DPN and 40 without neuropathy) have been enrolled, while 40 healthy volunteers served as group control. Neuropathy diagnosis was based on clinical assessment (through Michigan neuropathy screening instrument (MNSI) - both questionnaire and examination) and nerve conduction studies. Serum 25(OH)D levels were quantified using RIA. **Results:** Vitamin D levels were significantly lower in DPN patients (mean 13.2ng/mL) compared to diabetic (18.3ng/mL) and healthy controls (31.2ng/mL, $P<0.001$). Vitamin D deficiency (<10ng/mL) was found in 72.5% of DPN patients. Apart from severe neuropathy, other factors (age, body mass index -BMI- and HbA1c) have all been mildly inversely correlated to Vitamin D levels. **Conclusions:** Vitamin D deficiency is significantly associated with the presence and severity of DPN. These findings support the clinical value of assessing and potentially improving vitamin D status in diabetic patients, particularly in those with severe neuropathy.

Hell J Nucl Med 2025; 28(2): 90-95 *Epub ahead of print: 4 August 2025*

Introduction

Diabetic polyneuropathy (DPN) represents a prevalent, debilitating complication and strong source of morbidity of diabetes mellitus. Approximately 50% of T2DM patients develop it, resulting in foot ulcers, amputation, pain, motor, and sensory deficits [1]. Pathogenic pathway is not completely understood and among proposed factors, dominant conditions include chronic hyperglycemia, oxidative stress, inflammatory processes, and other vascular and metabolic mechanisms [2].

Recently, vitamin D has gained attention not only for bone and calcium metabolism but also for potential neuroprotective and anti-inflammatory effects. Vitamin D deficiency has been observed in patients with various neurodegenerative and demyelinating diseases, such as multiple sclerosis, Alzheimer's, and Parkinson's, suggesting contribution to pathogenesis [3]. Emerging evidence indicate a remarkable but still not proven correlation between low Vitamin D levels and diabetic neuropathy [4, 5], as deficiency seems to modulate insulin sensitivity, inflammation, and neurotrophins expression, apart from its protective role on bone formation and body fat ratio through biochemical receptors [6]. Patients with certain neuropathic symptoms such as: burning pain, tingling, and numbness, usually exhibit low 25-hydroxyvitamin D [25(OH)D] serum [7]. Vitamin D supplementation has been reported to lead to meaningful improvement in neuropathic symptoms, including reduced pain and enhanced nerve conduction parameters [8, 9].

Despite these association, the exact Vitamin D deficiency mechanism in DPN remains under investigation. Several studies support that vitamin D may exert anti-inflammatory effects through cytokine Il-6 and TNF - α downregulation [10]. In addition, Vitamin D appears to influence both insulin sensitivity and blood glucose regulation, essential factors in diabetes-related disorders pathophysiology [11].

Given the increasing global burden of diabetes and its complications, early identification of modifiable risk factors such as vitamin D deficiency, is crucial. Radioimmunoassay method (RIA) is a dependable and commonly used technique for measuring serum 25(OH)D, due to its strong analytical sensitivity and specificity [12]. Assessment of vitamin D levels in clinical settings typically relies on measuring serum concentrations of 25(OH)D, the major circulating form of vitamin [13].

The study aimed to evaluate serum 25(OH)D concentrations in patients with DPN using the RIA method, and to investigate its association with severe neuropathy. Our hypothesis is that patients with DPN exhibit significantly lower vitamin D levels, compared to those without neuropathy, and that lower levels are associated with more severe symptoms.

Subjects and Methods

Study design and participants

This cross-sectional observational study was carried out at Nuclear Medicine Department (Alexandroupolis University Hospital) within a 11-month period (between February and December 2019), in collaboration with the 2nd Department of Internal Medicine and the Blood Donation Department. A total of 120 diabetic patients, aged between 40 and 75 years, were recruited from outpatient endocrinology clinics. All of them had established T2DM, confirmed by medical history and standard biochemical criteria. Based on presence or absence of clinical and electrophysiological signs of neuropathy, participants were stratified into two groups. The DPN group consisted of 80 patients who fulfilled the Toronto consensus criteria for diabetic polyneuropathy, including characteristic symptoms, clinical signs, and abnormal findings on nerve conduction studies. The control group included 40 patients with T2DM but no signs or symptoms of neuropathy.

In addition to the Toronto clinical neuropathy scoring system, the diagnosis of DPN in participants was further confirmed using both the Michigan neuropathy screening instrument (MNSI) and nerve conduction studies (NCS). The MNSI was applied in its standard form, including both the symptom questionnaire and clinical examination, with a total score of ≥2.5 points on the physical examination component considered indicative of peripheral neuropathy. Nerve conduction studies were conducted in accordance to standard electrophysiological protocols of sensory nerve conduction velocities, amplitudes, and distal latencies in the lower limbs. Abnormalities in at least two nerves, one of which had to be sensory, were required to confirm the diagnosis. The combined use of clinical scoring and electrophysiological testing enhances diagnostic accuracy and aligns with internationally recognized criteria for DPN.

Besides the diabetic cohort, a third group consisting of 40 healthy volunteer blood donors (both men and women), aged 26 to 55 years, was included as a non-diabetic control group. These individuals had no history of diabetes, cardiovascular disease, or other chronic or acute medical conditions. All were deemed to be in good general health based on recent clinical and laboratory evaluations. Importantly, none of the healthy volunteers had received vitamin D supplementation during the last six months, ensuring that measured serum levels reflected true endogenous vitamin D status.

The inclusion criteria for all participants were deliberately stringent to minimize potential confounding variables. Eligible diabetic patients were required to have a minimum 5-year history of T2DM and maintain relatively stable metabolic control, defined as a recent glycated hemoglobin (Hb A1c) level below 9%. Patients with type 1 diabetes, impaired renal function (estimated glomerular filtration rate <60mL/min/1.73m^2), hepatic dysfunction, active infectious or inflammatory condition at the time of assessment, as well as individuals under medication with known interference to Vitamin D metabolism (such as glucocorticoids, antiepileptics, or antifungal agents) have been excluded.

Ethical standard criteria have been applied (each participant was fully informed about study's objectives and provided with written consent before any procedure). Protocol review board approval (502/31-05-2018) was in accordance to Helsinki Declaration of ethical conduct in human research. Using clear inclusion and exclusion criteria, and standardized clinical and electrophysiological tools, the study ensured both internal validity and potential application of its findings to similar patient populations.

Serum Vitamin D measurement

After overnight fast, morning blood sampling was collected for both diabetic and non-diabetic blood donor volunteers. Serum was separated and stored at -80°C until analysis. Serum levels of 25(OH)D were measured using the RIA method. Initially, calibrators, control sera, and samples were incubated with a stripping solution in antibody-coated tubes. This step effectively released both 25(OH)D_2 and 25(OH)D_3 from the Vitamin D binding protein (DBP), thereby allowing them to interact freely with the assay components. Following this, without any intermediate wash steps, a specific amount of 25(OH)D labeled with iodine-125 (^{125}I) was introduced. This radiolabeled tracer competed with the endogenous 25(OH)D_3 and 25(OH)D_2 from the samples, calibrators, or control sera for a limited number of binding sites on a monoclonal antibody that was immobilized on the inner surface of the reaction tubes. Following an adequate incubation period (allowing best equilibrium binding), tube contents were aspirated, washed for unbound tracer removal, and the remaining radioactivity bound to the antibody was measured using a gamma counter. A standard calibration curve was constructed using calibrator samples, and the total concentration of 25(OH)D (both D_2 and D_3 forms) in each sample was determined by interpolation against this curve. This method, widely used in clinical research and diagnostics, offers sufficient specificity and sensitivity for assessing vitamin D status in patients. All samples were analyzed duplicate to ensure consistency, and all procedures adhered strictly to the manufacturer's instructions for the assay kit used (DiaSorin). Results were expressed in ng/mL.

Vitamin D status was categorized as:

- Deficient: 10ng/mL
- Insufficient: 10-29ng/mL
- Sufficient: >30-150ng/mL
- Toxicity: >150ng/mL

Participant characteristics

The study population included 160 individuals divided into three groups: 80 patients with DPN, 40 diabetic patients without neuropathic symptoms (diabetic control group), and 40 healthy individuals (non-diabetic control group). All baseline characteristics for the three study groups are presented in Table 1.

These data highlight that while age, body mass index (BMI), and HbA1c were comparable between the diabetic groups, the longer duration of diabetes in the DPN group may be a critical factor associated with development of neuropathy. Additional analyses involving vitamin D levels in these groups will further elucidate the potential link between hypovitaminosis D and diabetic neuropathy.

***Table 1.** Baseline characteristics of participants.*

Characteristic	DPN group (n=80)	Diabetic group (n=40)	Control group (n=40)
Age (years)	63.4±9.1	61.7±8.6	40.5±14.5
Male/Female	46/34	17/23	24/16
Duration of diabetes (years)	12.3±4.5	9.1±3.9	-
BMI (kg/m²)	28.1±3.7	27.5±4.2	26.9±5.6
HbA1c (%)	7.4±0.9	7.1±0.8	5.3±0.4

Among the 80 patients included in the DPN group, a range of clinical symptoms consistent with diabetic polyneuropathy was observed, which are presented in Table 2. Electrophysiological testing supported clinical diagnosis, with most patients showing evidence of both sensory and motor nerve involvement. Reduced nerve conduction velocities and amplitudes were observed, consistent with chronic sensorimotor axonal neuropathy.

These findings highlight the clinical burden of DPN in the affected group and set the foundation for further analysis of biochemical correlations, particularly with vitamin D levels, in the subsequent sections.

Results

Serum Vitamin D levels

A marked difference was observed in 25(OH)D serum concentrations among the three study groups. Patients in the DPN group (n=80) exhibited significantly lower mean serum levels of 25(OH)D (13.2±8.5ng/mL) compared to both diabetic control group (n=40), (mean level:18.3±7.5ng/mL), and healthy control group who had the highest mean level (31.2± 6.5ng/mL). The differences between the DPN group and each of the two control groups were statistically significant (P< 0.001), suggesting a strong correlation between vitamin D deficiency and diabetic polyneuropathy.

In terms of vitamin D status categories, a high proportion of patients in the DPN group (72%, or 58 out of 80) were found to have deficient levels of 25(OH)D (<10ng/mL). This percentage was notably lower in the diabetic control group (33%, or 13 out of 40), and even lower in the health control group, where only 5 % (2 out of 40) had deficient levels (Table 3).

These findings provide additional support for the hypothesis that lower vitamin D status is associated with an increased likelihood of developing diabetic neuropathy. The substantial difference in the distribution of vitamin D categories between the two groups may reflect underlying pathophysiological differences or potential modifiable risk factors.

***Table 2.** Symptomatology in patients with diabetic polyneuropathy (n= 80).*

Symptom	Number of patients (n)	Percentage (%)
Distal numbness	60	75%
Paresthesia (tingling, pins & needles)	55	68.8%
Neuropathic pain (burning, stabbing)	48	60%
Lower limb muscle weakness	28	35%
Gait disturbances (ataxia, imbalance)	23	28.7%
Postural hypotension	10	12.5%
Gastrointestinal symptoms (constipation, gastroparesis)	5	6.2%
Diabetic foot (ulceration/infection)	3	3.75%

Statistical analysis

A comprehensive statistical analysis was performed to evaluate the relationship between serum 25(OH)D levels and the presence and severity of DPN. Both descriptive and inferential statistics were used.

Descriptive statistics

Age: The DPN group had a higher mean age (63.4±9.1 years) compared to the diabetic control group (61.7±8.6 years) and the healthy control group (40.5±14.5 years). The differences were statistically significant (ANOVA, P<0.001), particularly between the DPN group and the healthy control group.

Duration of diabetes: Patients with DPN had a significantly longer duration of diabetes (12.3±4.5 years) than diabetic

***Table 3.** Vitamin D status distribution.*

Vitamin D status	DPN group (n=80)	Diabetic group (n=40)	Control group (n=40)
Deficiency (<10 ng/mL)	58(72.5%)	13(32.5%)	2(5%)
Insufficiency (10-29 ng/mL)	14(17.5%)	22(55%)	12(30%)
Sufficiency (>30 ng/mL)	8(10%)	5(12.5%)	26(65%)
Mean (± SD) ng/mL	13.2±8.5ng/mL	18.3±7.5ng/mL	31.2±6.5ng/mL
P-value	P<0.001*		

**P-value for comparison of DPN group vs control group*

patients without neuropathy (9.1±3.9 years) (P<0.01, independent samples t-test), indicating disease duration as a potential risk factor for neuropathy.

HbA1c and BMI: No statistically significant differences were found in glycemic control (HbA1c) or BMI between the diabetic groups (P>0.05), suggesting these factors alone did not account for the presence of neuropathy.

Comparison of Vitamin D levels

There were statistically significant differences in mean serum 25(OH)D levels among the three groups (One-way ANOVA: F (2, 157)=87.95, P<0.001, η^2=0.51), indicating a large effect size. Post-hoc Tukey tests confirmed that all pairwise group comparisons were significant (P<0.001), with the largest difference observed between the DPN and control groups (mean difference= –18.00ng/mL, 95% CI: –21.17 to –14.83):

- **DPN group:** 13.2±8.5ng/mL
- **Diabetic controls:** 18.3±7.5ng/mL
- **Healthy controls:** 31.2±6.5ng/mL

Distribution of Vitamin D status

Chi-square test revealed statistically significant differences in the distribution of vitamin D status across the groups (P< 0.001), particularly highlighting a high prevalence of deficiency in DPN patients.

Correlation between Vitamin D levels and age, BMI, HbA1c in DPN group

In the DPN group, serum vitamin D levels were correlated with age, BMI and HbA1c. Specifically, Spearman's correlation coefficients (n=80) revealed moderate inverse associations between vitamin D and age (r= –0.52), BMI (r= –0.49), and HbA1c (r= –0.46). These results suggest that older age, higher BMI, and poorer glycemic control are all linked to lower vitamin D levels in DPN patients, reinforcing the multifactorial contributors to vitamin D deficiency in this population. Comparative correlation diagrams for age, BMI and HbA1c are also provided for the diabetic and control groups, in addition to the DPN group, to further illustrate group-specific patterns.

Correlation between Vitamin D levels and sex in DPN group

To explore the relationship between serum vitamin D levels and sex, a subgroup analysis was conducted within the DPN cohort as well as in diabetic and healthy control groups. In the DPN group, male participants exhibited slightly lower mean vitamin D levels (12.5±8.4ng/mL) compared to females (14.1±8.6ng/mL), with the difference reaching statistical significance (P=0.03), suggesting that gender may influence vitamin D status in neuropathic diabetic patients. In contrast, the sex-based differences in the diabetic control group (males: 19.5±7.1ng/mL vs. females: 17.4±7.8ng/mL, P=0.22) and in the healthy control group (males: 32.5±6.2ng/mL vs. females: 29.8±6.7ng/mL, P=0.18) were not statistically significant.

Correlation between Vitamin D and neuropathy symptoms

A moderate negative correlation was observed between serum 25(OH)D levels and the severity of neuropathic symptoms (e.g., numbness, paresthesia, neuropathic pain, motor deficits). Spearman's rank correlation coefficient showed r= -0.48, P<0.001. This suggests that lower vitamin D levels are associated with increased symptom burden and severity.

Discussion

This study reinforces the growing evidence that vitamin D deficiency may contribute to the development and severity of DPN in individuals with T2DM. Importantly, by incorporating a third group-healthy non-diabetic blood donors- we were able to compare serum vitamin D levels across a wider physiological spectrum. This approach enabled a more nuanced understanding of the interplay between vitamin D status and neuropathic manifestations.

Our findings demonstrated that patients with DPN had significantly lower 25(OH)D levels not only in comparison to diabetic individuals without neuropathy but also when contrasted with healthy controls. The mean serum vitamin D concentration among the healthy control group was more than double that of the DPN group, indicating a striking divergence in vitamin D status that may reflect both metabolic burden and neuropathic degeneration.

The inclusion of a healthy control group is crucial, as it allows us to distinguish between vitamin D deficiency that may result from chronic disease processes and deficiency that exists independently of any overt pathology. Comparable study designs have been used in previous research exploring vitamin D status across populations stratified into three distinct clinical categories. For instance, Kheyami et al. (2019) [19] and Toth et al. (2014) [20] both included healthy, diabetic without neuropathy and DPN groups in their analyses and reported comparable trend vitamin D levels were lowest in DPN patients and highest in healthy individuals, with diabetic controls falling in between. These patterns underscore a potential gradient of risk, with hypovitaminosis D worsening along with neuropathic progression.

From a pathophysiological standpoint, this gradient may reflect cumulative effects of chronic hyperglycemia, inflammation, and neurodegeneration on vitamin D metabolism or receptor responsiveness. Peripheral neurons and glial cells express vitamin D receptors, suggesting a potential role for the vitamin in modulating neurotrophic signaling, calcium dynamics, and inflammatory pathways [14, 15]. Its deficiency, therefore, may directly impair nerve function or exacerbate inflammatory damage to axons.

Furthermore, the correlation observed between vitamin D levels and neuropathic symptom severity strengthens the biological plausibility of this association. More pronounced and multifaceted neuropathic symptoms have been observed in patients with vitamin D deficiency, reflecting evidence from trials showing symptomatic and electrophysiological benefits following vitamin D supplementation [16, 17].

The prevalence of deficiency in the DPN group-over 70%-contrasted sharply with the 5% observed in the healthy controls, emphasizing that vitamin D insufficiency in this context is not merely incidental. Rather, it may represent a modifiable factor within a broader therapeutic strategy aimed at minimizing neuropathic complications.

While this study cannot establish causality due to its cross-sectional nature, its findings are in line with previous prospective and interventional data suggesting that addressing vitamin D deficiency may slow or mitigate the course of diabetic neuropathy [18, 5]. Nevertheless, future studies with larger cohorts and longitudinal follow-up are warranted to determine whether routine supplementation could be recommended as standard care for high-risk diabetic populations.

Lastly, the choice of RIA as the measurement method ensures high specificity and sensitivity, minimizing potential biases due to assay variability and reinforcing the credibility of our biochemical data [12].

In conclusion, this study not only confirms earlier associations between vitamin D deficiency and DPN but also extends them by contextualizing these findings within a healthy population baseline. Our findings suggest a strongly inverse association between serum vitamin D levels and DPN severity. Patients with DPN had significantly lower 25(OH)D concentrations as measured by RIA, and these levels correlated with clinical and electrophysiological markers of neuropathy. This triadic comparison highlights the potential role of vitamin D as both a biomarker of neuropathic risk and a possible therapeutic target, an insight that should inform future research and clinical guidelines alike.

The authors declare that they have no conflicts of interest.

Bibliography

1. Callaghan BC, Cheng HT, Stables CL et al. Diabetic neuropathy: Clinical manifestations and current treatments. *The Lancet Neurology* 2012; 11(6): 521-34.
2. Vincent AM, Russell JW, Low P, Feldman EL. Oxidative stress in the pathogenesis of diabetic neuropathy. *Endocr Rev* 2004; 25(4): 612-28.
3. Peterson CA, Nair D. Vitamin D deficiency and depression in adults: Systematic review and meta-analysis. *Br J Psychiatry* 2010; 197(2): 100-6.
4. Shehab D, Al-Jarallah K, Abdella N et al. Does vitamin D deficiency play a role in peripheral neuropathy in Type 2 diabetes? *Diab Med* 2012; 29(1): 43-9.
5. Zubair M, Malik A, Ahmad J. The role of vitamin D in diabetic foot ulcer: A prospective case-control study. *J Diab Compl* 2018; 32(12): 1082-5.
6. Toth C, Martyn C, Lichtenstein JD. Vitamin D and neuropathy. *In C. Casellanos (Ed.), Handbook of Clinical Neurology* 2014;(Vol. 126, pp. 171-190). Elsevier.
7. Putz Z, Tabák ÁG, Tóth N et al. Vitamin D deficiency is associated with neuropathic symptoms in patients with type 2 diabetes. *Diab Med* 2021; 38(1): e14430.
8. Sheikh A, Saeed Z, Javed MU, Baig S. Vitamin D supplementation and neuropathic pain in type 2 diabetes mellitus patients: A clinical trial. *Pain Med* 2022; 23(6): 1102-9.
9. Jin H, Sun Y, Zhang H, Zhang M. Effects of vitamin D supplementation on peripheral neuropathy in patients with type 2 diabetes: A randomized controlled trial. *Nutr Neuroscience* 2023; 26(7): 489-97.
10. Yammine K, Wehbe R, Assi C. A systematic review on the efficacy of vitamin D supplementation on diabetic peripheral neuropathy. *Clin Nutr* 2020; 39(10): 2970-4.
11. Pittas AG, Dawson-Hughes B, Sheehan P et al. Vitamin D supplementation for prevention of type 2 diabetes mellitus: A randomized controlled trial. *New Engl J Med* 2020; 381: 520-30.
12. Hollis BW. Measuring 25-hydroxyvitamin D: Analytical challenges and clinical implications. *Clin Chem* 2008; 54(11): 1981-3.
13. Hollis BW. Circulating 25-hydroxyvitamin D levels indicative of vitamin D sufficiency: Implications for establishing a new effective dietary intake recommendation for vitamin D. *J Nutr* 2005; 135(2): 317-22.
14. Eyles DW, Smith S, Kinobe R et al. Distribution of the vitamin D receptor and 1α-hydroxylase in human brain. *J Chem Neuroanatomy* 2005; 29(1): 21-30.
15. Alam U, Malik R A. Vitamin D and diabetic neuropathy: Pathophysiology and implications for therapy. *J Clin Pharm Therapeutics* 2014; 39(6): 766-9.
16. Sheikh A, Saeed Z, Javed H, Iqbal R. Association of vitamin D deficiency with diabetic neuropathy. *Cureus* 2022; 14(2): e22294.
17. Jin H, Kim Y, Lee J et al. The effect of vitamin D supplementation on diabetic peripheral neuropathy: A randomized, double-blind, placebo-controlled trial. *Diab Metabol J* 2023; 47(1): 72-80.
18. Putz Z, Tabák ÁG, Tóth N et al. Vitamin D deficiency is associated with autonomic neuropathy in type 2 diabetes. *Diab Med* 2021; 38(4): e14468.

19. Kheyami AM, Al-Bashir A, Al-Yafei F et al. Vitamin D deficiency and neuropathy in patients with type 2 diabetes mellitus: A comparative study with healthy controls. *Qatar Med J* 2019; (3): 10.
20. Toth C, Voll C, Wherrett D et al. Association of low vitamin D with peripheral neuropathy in type 2 diabetes mellitus. *Diab/Metabol Res Rev* 2014; 30(3): 291-6.

Salivary scintigraphy as a pre-treatment diagnostic tool to predict gland dysfunction following ^{131}I therapy

Hui Zhu[1,2] **MD,**
Wei Shen[2] **MD,**
Yuan Zhu[2] **MD,**
Zhao Liu[2] **MD,**
Zhiyong Li[2] **MD,**
Xiancun Hou[2*] **MD,**
Yuetao Wang[1,3*] **MD**

1. Department of Nuclear Medicine, The Third Affiliated Hospital of Soochow University, Changzhou 213003, Jiangsu Province, China
2. Department of Nuclear Medicine, Affiliated Hospital of Xuzhou Medical University, Xuzhou 221002, Jiangsu Province, China
3. Institute of Clinical Translation of Nuclear Medicine and Molecular Imaging, Soochow University, Changzhou 213003, Jiangsu Province, China

Keywords: Differentiated thyroid cancer - Radioiodine therapy
- Salivary dysfunction
- Salivary gland scintigraphy
- Xerostomia

Corresponding author:
Yuetao Wang MD,
Department of Nuclear Medicine, the Third Affiliated Hospital of Soochow University, Changzhou 213003, Jiangsu Province, China, Institute of Clinical Translation of Nuclear Medicine and Molecular Imaging, Soochow University, Changzhou 213003, Jiangsu Province, China
yuetao-w@163.com

Xiancun Hou MD,
Department of Nuclear Medicine, Affiliated Hospital of Xuzhou Medical University, Xuzhou 221002, Jiangsu Province, China
houxiancun@sina.com

Received:
13 January 2025
Accepted revised:
5 May 2025

Abstract

Objective: To evaluate whether pre-treatment salivary gland scintigraphy (SGS) with technetium-99m pertechnetate ($^{99m}TcO_4^-$) can predict the risk of moderate to severe salivary gland dysfunction and xerostomia in differentiated thyroid cancer (DTC) patients following their first radioiodine-131 (^{131}I) therapy. **Subjects and Methods:** We retrospectively enrolled 149 DTC patients (107 females, 42 males; mean age 46.6 ± 12.7 years) who underwent total thyroidectomy between October 2022 and March 2024. All subjects received pre-treatment SGS to measure the uptake index (UI) and excretion fraction (EF) of bilateral parotid and submandibular glands. Patients then underwent ^{131}I therapy (1.85-5.55GBq) and repeat SGS 6-12 months later under identical conditions. Xerostomia severity was assessed using the xerostomia inventory (XI) score, categorizing patients into no/mild (XI 11-23) versus moderate-extreme xerostomia (XI 24-55). **Results:** Post-therapy, all glands exhibited significant declines in UI (parotid and submandibular glands, $P<0.001$) and EF ($P\leq0.004$). There was no significant correlation between administered ^{131}I dose and percentage changes in UI (ΔUI%) or EF (ΔEF). However, higher ^{131}I doses were associated with increased rates of moderate-severe xerostomia ($P=0.015$) and higher mean XI scores ($P=0.008$). Receiver operating characteristic (ROC) analysis demonstrated that pre-treatment UI reliably predicted moderate to severe functional decline (ΔUI% > 20%) with areas under the curve (AUC) of 0.866 for the right parotid, 0.793 for the left parotid, 0.769 for the right submandibular, and 0.816 for the left submandibular glands (all $P<0.001$). Additionally, ΔUI% in both submandibular glands differed significantly between patients with no/mild and moderate–extreme xerostomia (right: $P=0.004$; left: $P=0.012$). **Conclusions:** Pre-treatment $^{99m}TcO_4^-$ SGS uptake index is a dependable predictor of moderate to severe salivary gland dysfunction and xerostomia following ^{131}I therapy in DTC patients, enabling early identification of individuals at high risk and guiding tailored preventive strategies.

Hell J Nucl Med 2025; 28(2): 96-114

Introduction

Thyroid cancer is the most common endocrine malignancy, with its incidence gradually increasing over the past decade [1]. Radioactive iodine (RAI) therapy is typically administered following thyroidectomy in patients with differentiated thyroid carcinoma (DTC) [2]. After oral administration of ^{131}I, it concentrates not only in residual thyroid tissues and thyroid cancer metastases but also in other tissues, such as the salivary glands, due to their expression of the sodium/iodide symporter (NIS), similar to the thyroid gland [3]. Therefore, ^{131}I treatment may lead to potential salivary gland dysfunction, which increases the risk of dental caries, periodontal disease, and other oral health complications [4]. Due to differences in research methods, including clinical symptoms and the time of salivary dysfunction, the incidence of salivary dysfunction is still unclear, ranging from 2% to 67% [5].

Additionally, due to the different iodine uptake abilities of the salivary glands and the different protective measures that may be taken after oral administration of ^{131}I, the activity given to patients may not accurately reflect the dose received by the salivary glands. At the same time, inherent differences between patients can also affect the overall pharmacokinetics of ^{131}I [6]. Some risk factors for salivary dysfunction are still unclear, and there is still a lack of reliable methods to predict the incidence of salivary gland dysfunction.

Technetium-99m-pertechnetate ($^{99m}TcO_4^-$) is commonly used in clinical settings, exploiting the shared ability of salivary and thyroid glands to actively concentrate $^{99m}TcO_4^-$ through the NIS; this mechanism mirrors the concentration processes of chloride (Cl^-) and iodide (I^-) [7, 8]. Within 20 minutes of intravenous administration, $^{99m}TcO_4^-$ accumulates in the salivary glands and is excreted with saliva, followed by acid stimulation to assess the salivary glands' secretory and excretory functions. This semi-quantitative method can evaluate glandular dysfunction after RAI therapy [9]. Clinicians can use the salivary gland scintigraphy (SGS)-based functional score as an objective metric to assess salivary gland dysfunction in DTC patients following RAI therapy, thereby facilitating prompt and effective management of complications [9]. However, its potential to predict salivary gland dysfunction before ^{131}I treatment has not yet been explored.

In this study, we enrolled a moderate-sized patient cohort and conducted SGS before and 6-12 months after ^{131}I therapy. We evaluated the changes in scintigraphy of each salivary gland before and after RAI, subjective symptoms, and factors influencing the development of salivary gland dysfunction in patients who received their first ^{131}I treatment. This study aimed to assess whether $^{99m}TcO_4^-$ SGS before treatment predicted salivary gland dysfunction in DTC patients following ^{131}I treatment. Increasing understanding of these factors and effectively predicting salivary gland dysfunction will help identify patients at higher risk of developing salivary dysfunction, which may aid in adjusting treatment and protective measures.

Subjects and Methods

Patients and clinical data collection

From October 2022 to March 2024, all patients underwent total thyroidectomy at Xuzhou Medical University, with a pathological diagnosis of DTC. A total of 149 patients who underwent $^{99m}TcO_4^-$ salivary gland scintigraphy were retrospectively reviewed. According to relevant guidelines [2], patients requiring ^{131}I treatment were selected following a joint assessment by surgeons and nuclear medicine physicians. Four to six weeks post-surgery, patients received their first RAI therapy, with doses ranging from (1.85 to 5.55GBq), guided by intraoperative findings and pathological results [10]. The research protocol was approved by the Ethical Committee of Xuzhou Medical University Affiliated Hospital (approval no. XYFY2023-KL443-01). A comprehensive overview of the study procedures was presented to all participants, who subsequently provided their written informed consent. Exclusion criteria included patients previously treated with chemotherapy or radiotherapy for any other malignancies, as well as those with concurrent conditions such as Sjogren's syndrome, salivary gland tumors, human immunodeficiency virus infection, autoimmune diseases, or a history of sialadenitis.

Before RAI, patients adhered to a low-iodine diet for at least three weeks and underwent SGS. Two hours after oral ^{131}I administration, patients were allowed to consume food, encouraged to drink plenty of water, and began taking vitamin C tablets to stimulate salivary gland secretion. Vitamin C was taken every four hours, except during sleep, at a dose of 0.1g for five consecutive days. Salivary gland scintigraphy was repeated 6-12 months after ^{131}I treatment under identical conditions to evaluate glandular uptake and excretion function changes. The flowchart of population selection is shown in Figure 1.

Salivary gland scintigraphy

Imaging was conducted using the GE Infinia VC Hawkeye 4 singly photon emission computed tomography/computed tomography (SPECT/CT) system, equipped with a low-energy, high-resolution parallel-hole collimator set to a 140keV peak and a 20% window width. Technetium-99m-pertechnetate was provided by Beijing Atom HighTech Co., Ltd. Before imaging, patients in a state of hypothyroidism who had fasted for over 4 hours were administered an intravenous dose of 0.37GBq of $^{99m}TcO_4^-$. Imaging of the salivary glands was conducted by covering the head and cervical area (zoom 2.5, one frame per minute). This study captured salivary gland counts 20 minutes post-injection to reflect uptake function, followed by the administration of 0.1g of vitamin C chewed as an acidic stimulant to enhance salivary gland secretion, with data collection continuing for an additional 10 minutes.

Image analysis

Elliptical regions of interest (ROI) were manually delineated in the bilateral parotid and submandibular gland areas, with equivalent areas of uniform background, also marked in the adjacent bilateral temporal-orbital regions for the parotid glands and in the neck areas for the submandibular glands. Special attention was given to avoiding regions containing residual thyroid tissue and oral areas. The uptake and excretion metrics for $^{99m}TcO_4^-$ were derived from the radioactive counts per minute generated within these ROI. Based on these radioactive counts, the salivary gland function of each gland was calculated, and the uptake index (UI) and excretion fraction (EF) of the parotid and submandibular glands were quantified using formulas referencing previous studies by Upadhyaya, Upadhyaya A et al. (2017) [11] and Fallahi B et al. (2013) [12]. The following functional indices were derived for each salivary gland by the following modified formulas:

$\Delta UI\% = [(\text{pre-treatment UI}) - (\text{post-treatment UI})] / (\text{pre-treatment UI}) \times 100\%$

$\Delta EF = (\text{pre-treatment EF}) - (\text{post-treatment EF})$

Variations in UI (ΔUI%) and EF (ΔEF) across these glands from pre-treatment SGS to post-treatment SGS were analyzed.

Assessment of salivary gland dysfunction

Patients' salivary gland status was followed up to 6-12 months after RAI. The study employed an XI to assess the severity of xerostomia in patients; according to the total score of XI, patients are divided into three categories (11-23 points: no to mild xerostomia, 24-39 points: moderate to severe xerostomia, 40-55 points: severe to extreme xerostomia), Selvakumar T et al. (2018) previously used this XI in their research [13]. Functional assessment determined a mild decrease in EF was defined as a decrease in EF of 11%-20%, a moderate decrease was 21%-30%, and a severe decrease was more than 30%, according to the literature [14], this study also defined mild UI decrease as a decrease of 11%-20% in UI,

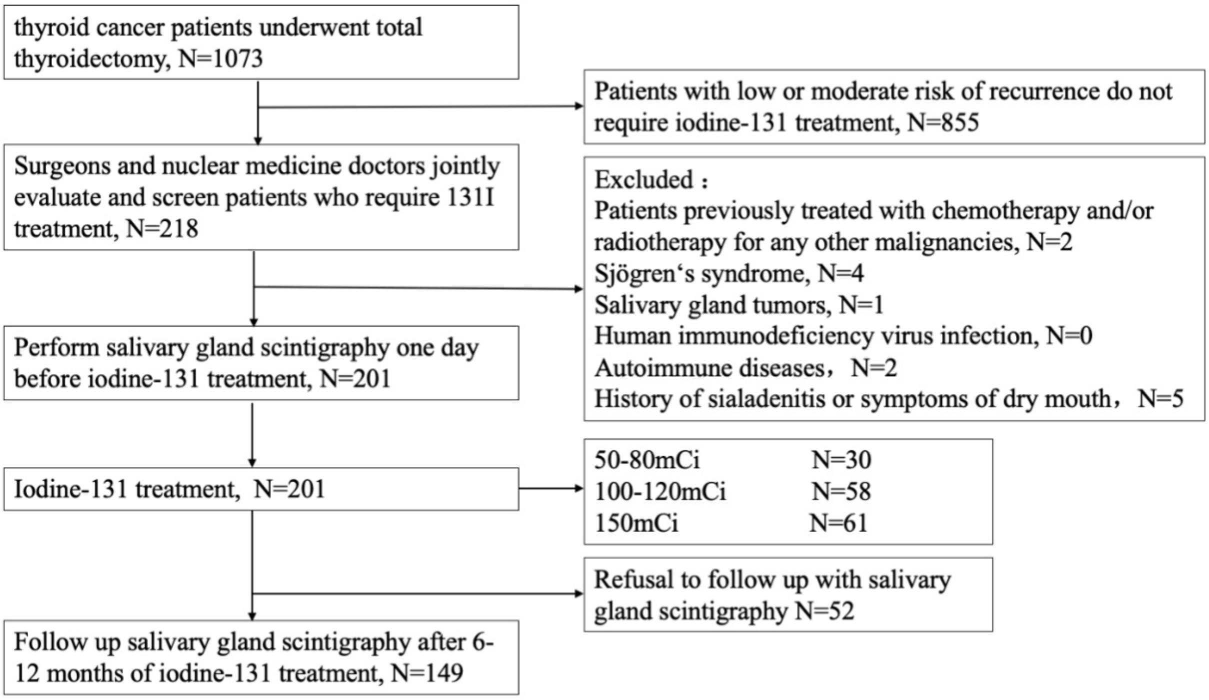

Figure 1. Shows the flowchart of population selection.

moderate decrease of 21%-30%, and severe decrease exceeding 30%. Each salivary gland was independently categorized into two groups based on its individual ΔUI% (≤20% or >20%) to assess differences in pre-treatment UI and EF values. This gland-specific approach ensures that variations in functional impairment are analyzed at the level of individual glands rather than aggregated across patients, allowing for a more detailed exploration of glandular responses to ^{131}I therapy. Image analysis was independently conducted by two experienced nuclear medicine physicians who, blind to original clinical reports and patient information, re-evaluated all studies to reach a consensus on findings.

Statistical analysis

Data were processed using SPSS 26.0. Normally distributed quantitative data are presented as mean±standard error of the mean (SEM), and comparisons between groups of continuous data adhering to a normal distribution were performed using analysis of variance (ANOVA). Non-normally distributed continuous data are expressed as median [interquartile range (Q1-Q3)] and analyzed using the Mann-Whitney U test, chi-square test, or Fisher's exact test as appropriate. The sensitivity and specificity of pre-UI in predicting moderate to severe functional impairment in salivary glands after ^{131}I treatment was evaluated using receiver operating characteristic (ROC) curves. Due to salivary gland dysfunction can be influenced by multiple factors, we need consider factors such as age, sex, T stage, risk classification, dose of ^{131}I therapy, pre-UI, and pre-EF to assess their associations with salivary gland dysfunction. However, in our analysis, these variables may lead to unreliable estimates, given the lack of sufficient variability across categories. Such as the TNM staging (N stage, M stage, and overall TNM stage), their highly skewed distribution in our cohort limited their statistical utility. To ensure robust and interpretable results, we focused on the factors with more balanced distributions. To assess the impact of follow-up duration on salivary gland dysfunction, a sensitivity analysis was conducted using linear regression, with the relationship between follow-up interval and ΔUI% analyzed and R^2 and P-values computed for statistical significance. P-value <0.05 was considered statistically significant.

Results

Characteristics and symptom evaluation of patients

Data from 596 salivary glands of 149 DTC patients who underwent RAI were fully collected. (107 females, 42 males; mean age 46.58±12.67 years; range, 21-74 years). Thirty patients (20.1%) received low-dose (1.85-2.96GBq), 57 patients (38.3%) received moderate dose (3.7-4.44GBq), and 61 patients (41.6%) received high-dose (5.55GBq) ^{131}I treatment. The clinical monitoring range after ^{131}I treatment is 6-12 months. During this period, no ^{131}I therapy or head and neck radiotherapy was administered. The demographic characteristics of the patients are detailed in Table 1.

Alterations in salivary gland functionality

Building upon the patient characteristics, salivary gland function was assessed before and after RAI treatment. Following RAI therapy, all salivary glands exhibited significant decreases in both UI and EF compared to pre-treatment levels (Table 2 and Figure 2). Chi-square analysis revealed a significant association between gland type and the degree of UI reduction, with submandibular glands more likely to experience reductions exceeding 30% compared to parotid glands. Furthermore, pairwise comparisons demonstrated that the >30% UI reduction category significantly differed from the ≤10%, 11%-20%, and 21%-30% reduction categories within each gland type (Table 3 and Figure 3). In contrast, the distribution of EF reductions did not differ significantly among the glands.

Table 1. *Characteristics of patients.*

Variables	Values
Total number of patients	149
Age (years)	46.58±12.67
Median/Range	48 (21-74)
Sex (Percentage%)	
Male	42 (28.2%)
Female	107 (71.8%)
T stage (Percentage%)	
Tx	2 (1.3%)
T1	69 (46.4%)
T2	26 (17.4%)
T3	29 (19.5%)
T4	23 (15.4%)
N stage (Percentage%)	
N0	5 (3.4%)
N1	140 (93.9%)
Nx	4 (2.7%)
M stage (Percentage%)	
M0	149 (100%)
M1	0 (0%)
TNM Stage (Percentage%)	
I	112 (75.2%)
II	26 (17.4%)
III	11 (7.4%)
Risk classification (Percentage%)	
Low	14 (9.4%)
Intermediate	75 (50.3%)
High	60 (40.3%)
Dose of ^{131}I therapy (GBq) (Percentage%)	
1.85-2.96	30 (20.1%)
3.7-4.44	57 (38.3%)
5.55	62 (41.6%)
Median / Range	3.7 (1.85-5.55)

(continued)

Mean±SEM; Bq, Becquerel

Association between the dosage of administered ^{131}I, salivary gland function and xerostomia severity

To further investigate the potential influence of radioactive iodine dosage on salivary gland function, we examined the association between the administered ^{131}I dose and salivary gland outcomes. The 149 DTC patients were categorized into three dosage groups: low-dose (1.85-2.96 GBq, n=30, 20.1%), moderate-dose (3.7-4.44 GBq, n=57, 38.3%), and high-dose (5.55GBq, n=61, 41.6%). There were no significant differences in age or gender distribution among the dosage groups, and the distribution of disease stages approached statistical significance (P=0.068). Pre-treatment UI and EF did not differ significantly across dosage groups. Post-treatment analyses revealed no significant differences in UI, EF, ΔUI%, or ΔEF% among the different dosage groups (Table 4), and the distribution of ΔUI% and ΔEF% changes did not vary significantly across dosage levels (Table S1). These findings indicate that the administered ^{131}I dose was not associated with variations in salivary gland function outcomes.

However, comparison of xerostomia severity scores across different ^{131}I dose groups revealed that patients in the high-dose group experienced significantly higher rates of moderate to severe xerostomia (50.0%) compared to those in the low-dose (23.3%) and moderate-dose (31.6%) groups (Table 4 and Table S2). Additionally, the mean XI score was significantly higher in the high-dose group compared to the low-dose groups (Figure 4). These results suggest that higher doses of ^{131}I are associated with more severe subjective symptoms of xerostomia, despite the lack of significant differences in objective salivary gland function indicators.

***Table 2.** Salivary gland function before and after RAI.*

	Uptake Index			P value	Excretion Fraction			P value
	Before	After	ΔUI		Before	After	ΔEF	
RPG	2.35±0.76	1.71±0.51	0.64±0.79	**<0.001**	0.56±0.29	0.46±0.32	0.10±0.34	**0.004**
LPG	2.32±0.69	1.74±0.51	0.57±0.72	**<0.001**	0.56±0.29	0.45±0.32	0.11±0.28	**0.001**
RSMG	1.32±0.63	0.81±0.31	0.51±0.50	**<0.001**	0.39±0.29	0.35±0.24	0.05±0.31	**0.038**
LSMG	1.34±0.66	0.83±0.31	0.51±0.52	**<0.001**	0.37±0.41	0.33±0.24	0.04±0.39	**0.031**

Mean±SEM; Group comparisons were conducted using the Mann-Whitney U test. The statistically significant P values are highlighted in bold. UI, Uptake Index; EF, Excretion Fraction; RPG, right parotid gland; LPG, left parotid gland; RSMG, right submandibular gland; LSMG, left submandibular gland.

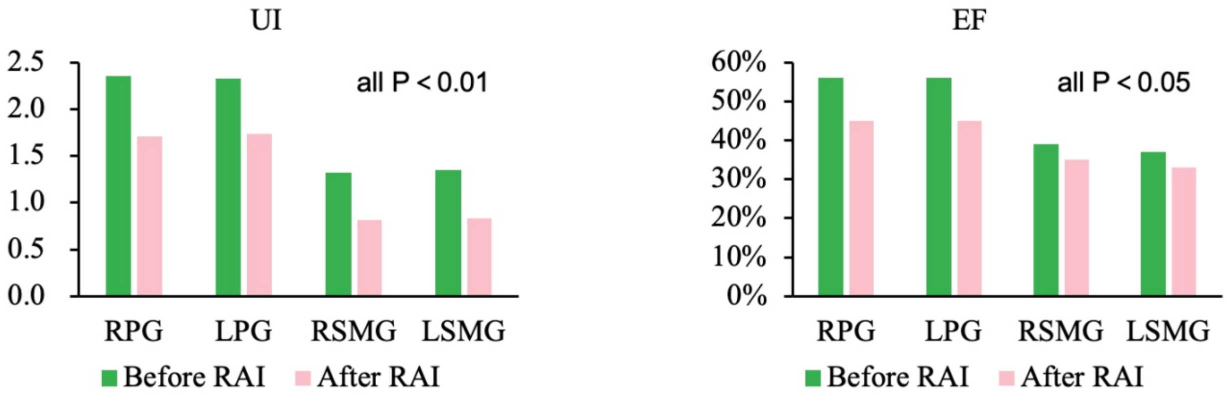

Figure 2. Salivary gland function before and after RAI.

***Table 3.** Distribution of salivary gland dysfunction by degree of reduction in ΔUI% and ΔEF after RAI (N=149).*

Parameter	≤10% decrease	11%-20% decrease	21%-30% decrease	>30% decrease	P value
ΔUI%					<0.001
RPG (N)	50a	20a	29a	50b	
LPG (N)	53a	20a,b	20a,b	56b	
RSMG (N)	32a	13a,b	20a,b	84b	
LSMG (N)	34a	14a,b	12a	89b	
ΔEF					0.584
RPG (N)	71	17	13	48	
LPG (N)	63	22	15	49	
RSMG (N)	72	15	6	56	
LSMG (N)	68	19	9	53	

UI, Uptake Index; EF, Excretion Fraction; RPG, right parotid gland; LPG, left parotid gland; RSMG, right submandibular gland; LSMG, left submandibular gland. Group comparisons were conducted using the chi-square test. The statistically significant P values are highlighted in bold. P values represent the statistical significance of differences across all subgroups (≤10%, 11%-20%, 21%-30%, >30%) within each salivary gland. Groups marked with the same letter (e.g., a) are not significantly different from each other, whereas groups with different letters (e.g., a and b) indicate statistically significant differences (P < 0.05) in the pairwise comparisons.

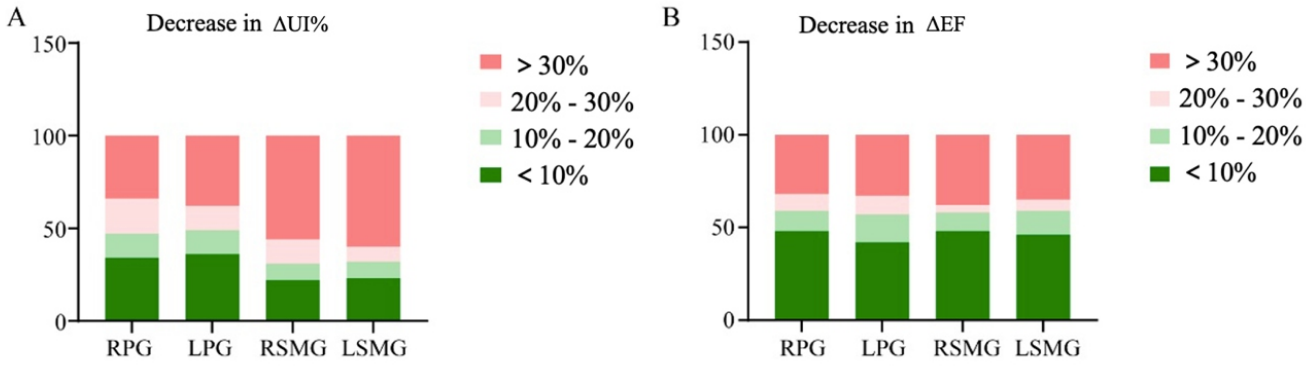

Figure 3. Percentage decrease in thyroid uptake and excretion after ^{131}I therapy. A) Percentage decrease in thyroid uptake. B) Percentage decrease in thyroid excretion. Different colors indicate different change ranges: dark green represents no decrease or a decrease of ≤10%, light green indicates a decrease of 11% to 20%, light pink indicates a decrease of 20% to 30%, and dark pink indicates a decrease of >30%.

Table 4. *Comparison of salivary gland function in different dose groups of ^{131}I.*

	Dose of ^{131}I therapy (GBq)			**P value**
	(1.85-2.96)	(3.7-4.44)	(5.55)	
Sex				0.353[a]
Male	6 (20.0%)	15 (26.3%)	21 (33.9%)	
Female	24 (80.0%)	42 (73.7%)	41 (66.1%)	
disease stage				0.068 [b]
I	27 (90.0%)	44 (77.2%)	41 (66.1%)	
II	3 (10.0%)	11 (19.3%)	13 (21.0%)	
III	0 (0.0%)	2 (3.5%)	8 (12.9%)	
xerostomia inventory				**0.015**[a]
No to mild xerostomia	23(76.7%)	39(68.4%)	29(46.8%)	
Moderate to severe xerostomia	7(23.3%)	18(31.6%)	31(50.0%)	
Age (years)	46.33±11.33	46.28±12.67	46.98±13.45	0.931[a]
Pre-RPG-UI	2.38±0.86	2.37±0.75	2.33±0.72	0.948 [c]
Pre-LPG-UI	2.41±0.73	2.32±0.81	2.27±0.55	0.682 [c]
Pre-RSMG-UI	1.48±0.62	1.28±0.64	1.29±0.62	0.248 [c]
Pre-LSMG-UI	1.45±0.61	1.30±0.69	1.32±0.64	0.309 [c]
Pre-RPG-EF	0.51±0.33	0.59±0.25	0.56±0.31	0.595 [c]

(continued)

Pre-LPG-EF	0.57±0.27	0.58±0.29	0.54±0.30	0.534 [c]
Pre-RSMG-EF	0.40±0.20	0.37±0.37	0.41±0.23	0.737 [c]
Pre-LSMG-EF	0.44±0.19	0.33±0.62	0.38±0.21	0.490 [c]
Post-RPG-UI	1.88±0.62	1.69±0.42	1.65±0.52	0.167 [c]
Post-LPG-UI	1.84±0.51	1.72±0.50	1.72±0.54	0.391 [c]
Post-RSMG-UI	0.87±0.31	0.80±0.30	0.80±0.32	0.516 [c]
Post-LSMG-UI	0.80±0.23	0.82±0.32	0.85±0.34	0.868 [c]
Post-RPG-EF	0.52±0.30	0.50±0.28	0.41±0.37	0.368 [c]
Post-LPG-EF	0.47±0.35	0.46±0.28	0.42±0.34	0.730 [c]
Post-RSMG-EF	0.37±0.20	0.34±0.20	0.34±0.28	0.678 [c]
Post-LSMG-EF	0.38±0.26	0.33±0.18	0.32±0.27	0.478 [c]
RPG-ΔUI%	0.15±0.25	0.23±0.25	0.24±0.26	0.290 [c]
LPG-ΔUI%	0.19±0.25	0.21±0.23	0.21±0.27	0.893 [c]
RSMG-ΔUI%	0.35±0.24	0.30±0.26	0.32±0.22	0.408 [c]
LSMG-ΔUI%	0.38±0.22	0.28±0.27	0.30±0.23	0.144 [c]
RPG-ΔEF	0.00±0.31	0.10±0.33	0.15±0.35	0.195 [c]
LPG-ΔEF	0.09±0.27	0.12±0.31	0.12±0.26	0.926 [c]
RSMG-ΔEF	0.02±0.19	0.03±0.43	0.08±0.22	0.464 [c]
LSMG-ΔEF	0.06±0.22	0.01±0.56	0.06±0.23	0.964 [c]
XI score	19.57±4.88	20.54±4.75	23.29±6.57	**0.008 [c]**

Pre-UI, pre-treatment Uptake Index; Pre-EF, pre-treatment Excretion Fraction; RPG, right parotid gland; LPG, left parotid gland; RSMG, right submandibular gland; LSMG, left submandibular gland; ΔUI, changes in Uptake Index; ΔEF, changes in Excretion Fraction; XI score, xerostomia inventory score; Mean ± SEM; a: Fisher's exact test was employed to compare the groups. b: The chi-square test was employed to compare the groups, c: The Kruskal-Wallis H test was utilized to compare the groups, and the statistically significant P values are highlighted in bold.

***Table S1.** Distribution of ΔUI% and ΔEF changes across different ^{131}I therapy doses in salivary glands.*

Salivary Gland	Metric	Change Category	1.85-2.96GBq	3.7-4.44GBq	5.55GBq	P value
RPG	ΔUI%	-10%＜	43.3	31.6	30.6	0.191
		-20% to - 11%	10.0	15.8	12.9	
		-30% to - 21%	23.3	19.3	17.7	
		＜-30%	23.3	33.3	38.7	
	ΔEF	-10%＜	16.7	26.3	22.6	0.100
		-20% to - 11%	3.3	14.0	8.1	
		-30% to - 21%	13.3	5.3	8.1	
		＜-30%	66.7	54.4	61.3	
LPG	ΔUI%	-10%＜	36.7	31.6	38.7	0.838
		-20% to - 11%	13.3	19.3	8.1	
		-30% to - 21%	16.7	12.3	12.9	
		＜-30%	33.3	36.8	40.3	
	ΔEF	-10%＜	46.7	40.4	41.9	0.972
		-20% to - 11%	6.7	15.8	17.7	
		-30% to - 21%	13.3	10.5	8.1	
		＜-30%	33.3	33.3	32.3	
RSMG	ΔUI%	-10%＜	23.3	22.8	19.4	0.919
		-20% to - 11%	3.3	12.3	8.1	
		-30% to - 21%	10.0	14.0	14.5	
		＜-30%	63.3	50.9	58.1	
	ΔEF	-10%＜	56.7	43.9	48.4	0.794
		-20% to - 11%	10.0	5.3	14.5	
		-30% to - 21%	0.00	10.5	0.00	
		＜-30%	33.3	40.4	37.1	

(continued)

LSMG	ΔUI%	-10%＜	16.7	26.3	22.6	0.789
		-20% to - 11%	3.3	14.0	8.1	
		-30% to - 21%	13.3	5.3	8.1	
		＜-30%	66.7	54.4	61.3	
	ΔEF	-10%＜	53.3	45.6	41.9	0.576
		-20% to - 11%	10.0	8.8	17.7	
		-30% to - 21%	6.7	5.3	6.5	
		＜-30%	30.0	40.4	33.9	

RPG, right parotid gland; LPG, left parotid gland; RSMG, right submandibular gland; LSMG, left submandibular gland. Categories of change (≤-10%, -20% to -11%, -30% to -21%, and ＜-30%) represent the magnitude of functional decline. P-values indicate whether the observed differences in functional change across different ^{131}I therapy doses (1.85-2.96GBq, 3.7-4.44GBq and 5.55GBq) are statistically significant.

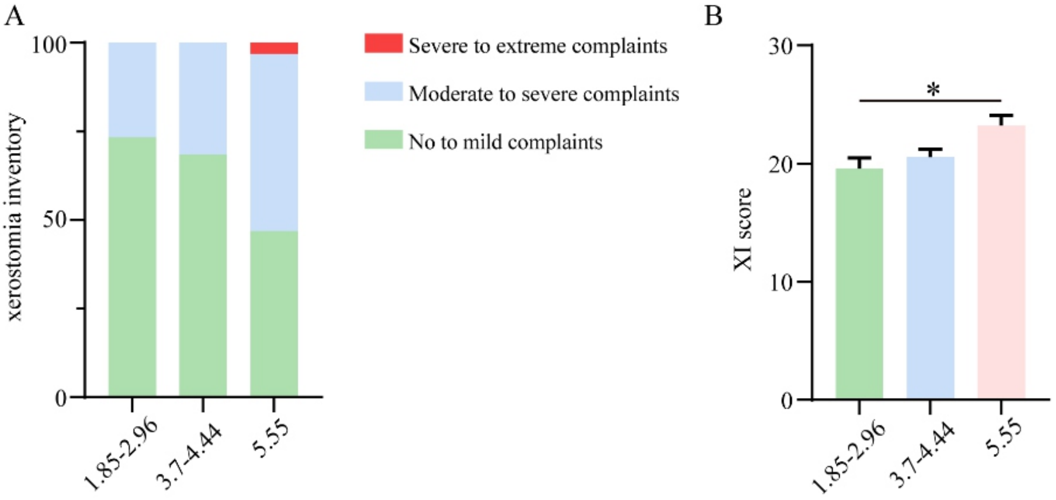

Figure 4. Comparison of xerostomia complaints and XI scores among DTC patients receiving different doses of ^{131}I therapy. A) Distribution of xerostomia complaints: no to mild (green), moderate to severe (blue), and severe to extreme (red). B) Mean XI scores across dosage groups (Kruskal-Wallis H test). *P<0.05.

Table S2. *Comparison of xerostomia severity scores across different ^{131}I dose groups.*

	Dose of ^{131}I therapy (GBq)			P value
	(1.85-2.96)	(3.7-4.44)	(5.55)	
Xerostomia inventory				0.015^{d}
No to mild xerostomia	23 (76.7%)a	39 (68.4%)a	29 (46.8%)b	
Moderate to severe xerostomia	7 (23.3%)a	18 (31.6%)a	31 (50.0%)b	

Group comparisons for xerostomia severity were conducted using the chi-square test, with superscripts (e.g., a, b) indicating pairwise comparisons. Groups with the same letter are not significantly different, while different letters indicate statistical significance (P < 0.05). Statistically significant values are highlighted in bold.

Predictive value of Pre-UI for moderate to severe damage to salivary gland function

To assess the predictive potential of the pre-treatment uptake index (Pre-UI) for moderate to severe salivary gland dysfunction, each gland was categorized based on its percentage change in uptake index (ΔUI%) into two groups: ≤20% decrease and >20% decrease. The ≤20% decrease category represents mild or no dysfunction, whereas the >20% decrease category indicates moderate to severe dysfunction. Glands with ΔUI% > 20% exhibited significantly higher Pre-UI values compared to those with ΔUI% ≤ 20% across all gland types (Table 5). In contrast, pre-treatment excretion fraction (Pre-EF) did not consistently differ between the two ΔUI% groups across all glands. Univariate analyses confirmed that Pre-UI is a significant predictor of moderate to severe salivary gland dysfunction in all glands (Table S3-6).

Table 5. *Comparison of Pre-UI in salivary glands between and ΔUI% ≤ 20% and ΔUI%>20% after RAI.*

	20%	**ΔUI%>20%**	**P value**
Pre-RPG-UI	1.92±0.54	2.53±0.76	**<0.001**
Pre-LPG-UI	2.10±0.60	2.41±0.71	**0.007**
Pre-RSMG-UI	1.07±0.65	1.39±0.65	**0.002**
Pre-LSMG-UI	1.07±0.43	1.40±0.66	**<0.001**
Pre-RPG-EF	0.57±0.27	0.56±0.30	0.990
Pre-LPG-EF	0.57±0.30	0.56±0.29	0.837
Pre-RSMG-EF	0.37±0.17	0.38±0.45	0.657
Pre-LSMG-EF	0.39±0.20	0.39±0.31	0.536

Pre-RPG-UI, pre-treatment right parotid gland uptake; Pre-RPG-EF, pre-treatment right parotid gland excretion; Pre-LPG-UI, pre-treatment left parotid gland uptake; Pre-LPG-EF, pre-treatment left parotid gland excretion; Pre- RSMG - UI, pre-treatment right submandibular gland uptake; Pre-RSMG-EF, pre-treatment right submandibular gland excretion; Pre-LSMG-UI, pre-treatment left submandibular gland uptake; Pre- LSMG-EF, pre-treatment left submandibular gland excretion; ΔUI, changes in Uptake Index; Mean ± SEM. Group comparisons were conducted using the Mann-Whitney U test. The statistically significant P values are highlighted in bold.

Table S3. *Univariate analysis of risk factors associated with RPG.*

	Univariate		
Variables	**OR**	**95% CI**	**P value**
Age	0.990	0.954-1.026	0.572
Sex	0.714	0.279-1.831	0.483
T stage			0.443
T1	0.992	0.013-74.000	0.997
T2	0.872	0.113-6.762	0.896
T3	2.615	0.255-26.777	0.418
T4	0.535	0.110-2.612	0.440
Risk classification			0.385

(continued)

Intermediate	0.204	0.021-1.973	0.170
High	0.471	0.084-2.641	0.392
Dose of ^{131}I therapy			0.540
3.7-4.44	0.432	0.092-1.998	0.283
5.55	0.792	0.247-2.543	0.695
Pre-RPG-UI	5.884	2.651-13.061	0.000
Pre-RPG-EF	0.545	0.120-2.481	0.433

Pre-RPG-UI, pre-treatment right parotid gland uptake; Pre-RPG-EF, pre-treatment right parotid gland excretion.

Table S4. *Univariate analysis of risk factors associated with LPG.*

Variables	Univariate		P value
	OR	**95% CI**	
Age	0.989	0.957-1.023	0.529
Sex	0.491	0.213-1.135	0.096
T stage			0.330
T1	0.197	0.007-5.839	0.348
T2	0.223	0.039-1.277	0.092
T3	0.293	0.043-2.023	0.213
T4	0.213	0.049-0.934	0.040
Risk classification			0.891
Intermediate	1.046	0.122-8.956	0.967
High	0.772	0.188-3.164	0.720
Dose of ^{131}I therapy			0.469
3.7-4.44	2.419	0.552-10.591	0.241
5.55	1.707	0.572-5.093	0.338
Pre-LPG-UI	2.571	1.277-5.173	0.008
Pre-LPG-EF	0.928	0.226-3.810	0.917

Pre-LPG-UI, pre-treatment left parotid gland uptake; Pre-LPG-EF, pre-treatment left parotid gland excretion

Additionally, to ensure that the follow-up interval did not confound the observed associations, a sensitivity analysis using linear regression was performed. This analysis assessed the relationship between the follow-up interval (treated as a continuous variable) and ΔUI% for each gland. The results indicated no significant associations between follow-up duration and ΔUI% across all glands with minimal R^2 values (Table S7). Receiver operating characteristic (ROC) curve analyses further demonstrated that Pre-UI effectively predicts moderate to severe salivary gland dysfunction. The Pre-RPG-UI achieved an area under the curve (AUC) of 0.866 with a cut-off value of 2.30, sensitivity of 79.7%, and specificity of 81.4% (Figure 5A). Similarly, the Pre-LPG-UI yielded an AUC of 0.793, a cut-off value of 2.13, sensitivity of 84.2%, and specificity of 67.1% (Figure 5B). The Pre-RSMG-UI demonstrated an AUC of 0.769, a cut-off value of 0.87, sensitivity of 84.9%, and specificity of 55.8% (Figure 5C). Lastly, the Pre-LSMG-UI showed an AUC of 0.816, a cut-off value of 0.86, sensitivity of 90.1%, and specificity of 64.6% (Figure 5D). These ROC analyses confirm that Pre-UI is a reliable predictor of significant salivary gland dysfunction following ^{131}I therapy.

Table S5. *Univariate analysis of risk factors associated with RSMG.*

Variables	Univariate		P value
	OR	**95% CI**	
Age	1.026	0.985-1.069	0.217
Sex	0.523	0.173-1.586	0.252
T stage			0.630
T1	306205465.2	0.000	0.999
T2	1.125	0.177-7.160	0.900
T3	0.419	0.058-3.046	0.390
T4	1.144	0.233-5.617	0.869
Risk classification			0.486
Intermediate	0.252	0.019-3.338	0.296
High	0.868	0.160-4.698	0.869
Dose of ^{131}I therapy			0.561
1.85-2.96	2.020	0.322-12.667	0.453
3.7-4.44	2.007	0.538-7.495	0.300
Pre-RSMG-UI	3.552	1.220-10.340	0.020
Pre-RSMG-EF	0.834	0.127-5.462	0.850

Pre-RSMG-UI, pre-treatment right submandibular gland uptake; Pre-RSMG-EF, pre-treatment right submandibular gland excretion

Table S6. *Univariate analysis of risk factors associated with LSMG.*

Variables	Univariate OR	Univariate 95% CI	P value
Age	1.005	0.969-1.043	0.781
Sex	0.409	0.145-1.151	0.090
T stage			0.972
T1	2405814504	0.000	0.999
T2	1.201	0.215-6.712	0.835
T3	1.051	0.154-7.155	0.959
T4	1.645	0.381-7.098	0.505
Risk classification			0.472
Intermediate	0.217	0.019-2.504	0.221
High	0.564	0.115-2.777	0.482
Dose of ^{131}I therapy			0.453
1.85-2.96	3.015	0.517-17.597	0.220
3.7-4.44	1.655	0.512-5.350	0.400
Pre-LSMG-UI	6.656	2.330-19.012	0.000
Pre-LSMG-EF	0.677	0.188-2.439	0.551

Pre-LSMG-UI, pre-treatment left submandibular gland uptake; Pre- LSMG-EF, pre-treatment left submandibular gland excretion

Predictive value of Pre-UI for xerostomia severity

Building upon the predictive role of Pre-UI in salivary gland dysfunction, we investigated whether Pre-UI also predicts the severity of xerostomia symptoms. Based on XI scores, 38.9% (58/149) of patients experienced moderate to extreme xerostomia. Significant differences were observed between patients with no to mild xerostomia and those with moderate to extreme xerostomia in the Pre-UI of the right submandibular gland and left submandibular gland, as well as in the percentage change in uptake index of the right submandibular gland and left submandibular gland (Table 6). In contrast, there were no significant differences in the Pre-UI, ΔUI%, EF, or ΔEF% of the bilateral parotid glands between the two groups. Further analysis categorized salivary gland dysfunction and xerostomia severity for each gland type based on xerostomia severity (no to mild vs. moderate to extreme xerostomia). The results indicated that dysfunction in RPG, LPG, RSMG, and LSMG was not significantly associated with xerostomia severity (Table 7).

Univariate logistic regression analyses revealed that female sex and high-risk classification were significantly associated with increased severity of xerostomia. In contrast, other variables-including age, T stage, intermediate risk classification, dose of ^{131}I therapy, and pre-treatment uptake indices-did not show significant associations with xerostomia severity (Table S8).

Discussion

Salivary gland dysfunction is a common complication of ^{131}I therapy after thyroidectomy in DTC patients [13]. This dysfunction is attributed to ^{131}I retention within the salivary glands, driven by increased capillary permeability due to inflammatory responses and further exacerbated by inflammatory-induced ductal wall damage and luminal obstruction [15, 16]. Conservative measures such as adequate hydration, salivary stimulation, gland Massage, and the use of

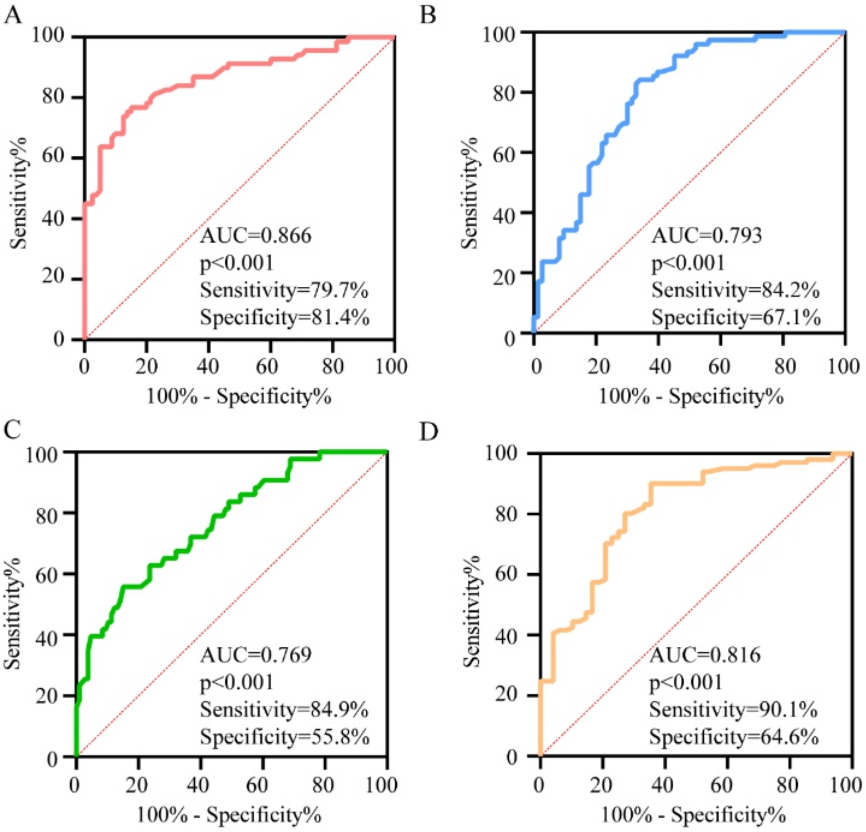

Figure 5. ROC curve analysis for predicting parotid gland dysfunction using pre-UI. A) ROC curve for Pre-RPG-UI in predicting RPG dysfunction. B) ROC curve for Pre-LPG-UI in predicting LPG dysfunction. C) ROC curve for Pre-RSMG-UI in predicting RSMG dysfunction. D) ROC curve for Pre-LSMG-UI in predicting LSMG dysfunction.

Table S7. *Sensitivity analysis of follow-up interval on salivary gland dysfunction using linear regression.*

Variables	**R^2**	**P value**
RPG-ΔUI%	0.001	0.734
LPG-ΔUI%	0.006	0.355
RSMG-ΔUI%	0.001	0.715
LSMG-ΔUI%	0.007	0.313

RPG, right parotid gland; LPG, left parotid gland; RSMG, right submandibular gland; LSMG, left submandibular gland.

NSAID, anticholinergics, or corticosteroid therapy generally alleviate these conditions [17]. However, in refractory cases, invasive methods such as saliva endoscopy treatment have limitations, particularly in patients with small ductal lumens [18]. Therefore, predicting salivary gland dysfunction is crucial for identifying patients who require stringent post-treatment surveillance and for minimizing the impact of dysfunction. Previous studies have utilized SGS to evaluate gland function post-^{131}I therapy in DTC patients, highlighting its non-invasive, convenient nature, capability to quantitatively or semi-quantitatively assess individual gland uptake and secretion functions with high repeatability [19, 20]. This study further demonstrates the potential of $^{99m}TcO_4^-$ SGS before treatment to predict salivary gland dysfunction caused by RAI therapy.

The salivary gland dysfunction incidence rate observed in this study is slightly higher than previously reported [14, 21], potentially due to differences in follow-up durations. For example, Solans et al. (2001) followed-up 79 patients who received ^{131}I therapy, and SGS showed that 50.6% (40/79) of

Table 6. *Comparison of functional parameters between no to mild and moderate to extreme xerostomia.*

	Xerostomia Inventory		P value
	No to mild xerostomia	Moderate to extreme xerostomia	
Pre-RPG-UI	2.29±0.08	2.46±0.10	0.184
Pre-LPG-UI	2.26±0.10	2.40±0.10	0.245
Pre-RSMG-UI	1.18±0.05	1.56±0.09	**<0.001**
Pre-LSMG-UI	1.21±0.05	1.55±0.10	**0.006**
Pre-RPG-EF	0.57±0.03	0.54±0.04	0.663
Pre-LPG- EF	0.57±0.03	0.54±0.04	0.344
Pre-RSMG- EF	0.40±0.03	0.38±0.03	0.591
Pre-LSMG- EF	0.37±0.05	0.38±0.03	0.214
RPG-ΔUI%	0.20±0.03	0.26±0.03	0.070
LPG-ΔUI%	0.18±0.03	0.24±0.02	0.080
RSMG-ΔUI%	0.27±0.02	0.40±0.03	**0.004**
LSMG-ΔUI%	0.27±0.02	0.37±0.03	**0.012**
RPG-ΔEF	0.10±0.04	0.11±0.05	0.483
LPG-ΔEF	0.12±0.03	0.10±0.04	0.898
RSMG-ΔEF	0.04±0.04	0.06±0.03	0.586
LSMG-ΔEF	0.03±0.05	0.06±0.03	0.994

Mean ± SEM. Group comparisons were conducted using the Mann-Whitney U test. The statistically significant P values are highlighted in bold.

the patients had changes in glandular function in the first year after ^{131}I treatment. Only 13.9% (11/79) of the patients had changes in glandular function in the second year [22]. Jeong et al. (2013) followed up about 5 years after RAI ablation[14], and the results showed that only 21.3% of the glands showed a decrease in UI, and 20.3% showed a decrease in glandular EF.

Thyroid remnants are capable of absorbing high radiation doses due to prolonged iodine uptake, whereas salivary glands, lacking iodine organification, can excrete absorbed ^{131}I, particularly under conditions such as acid stimulation or mastication. This excretion process is independent of thyrotropin levels or thyroid function [14]. Differences in NIS-mediated uptake and secretion determine the retention of ^{131}I in salivary glands. This indicates that patients with stronger uptake ability have higher radiation doses, leading to more severe damage [23, 24]. Previous studies have reported that even with relatively low levels of ^{131}I administered, salivary gland damage can still be observed [11, 25]. This study evaluated salivary gland function across different iodine treatment dose groups, revealing no significant differences in Pre-UI and Pre-EF. Similarly, no statistical differences were found in Post-UI and Post-EF or the change in ΔUI% or ΔEF across different dosage groups. Consistent with Son et al. (2019) [3], their logistic reg-

Table 7. *Distribution of salivary gland dysfunction and xerostomia severity across different salivary glands.*

Injury site	Xerostomia Inventory		P value
	No to mild xerostomia (90)	Moderate to extreme xerostomia (59)	
RPG	62	44	0.465
LPG	63	43	0.854
RSMG	74	51	0.649
LSMG	70	47	0.841

RPG, right parotid gland; LPG, left parotid gland; RSMG, right submandibular gland; LSMG, left submandibular gland.

Table S8. *Univariate logistic regression analysis of factors associated with xerostomia severity.*

Variables	Univariate		P value
	OR	95% CI	
Age	0.992	0.962-1.024	0.629
Sex	2.747	1.080-6.985	0.034
T stage			0.844
T1	8336364752	0.000	0.999
T2	2.020	0.451-9.044	0.358
T3	2.720	0.514-14.395	0.239
T4	1.469	0.445-4.845	0.528
Risk classification			0.093
Intermediate	0.395	0.048-3.249	0.388
High	0.211	0.050-0.898	0.035
Dose of ^{131}I therapy			0.391
1.85-2.96	0.359	0.083-1.557	0.171
3.7-4.44	0.667	0.238-1.870	0.442
Pre-RPG-UI	0.957	0.518-1.765	0.887
Pre-LPG- UI	1.214	0.625-2.357	0.567
Pre-RSMG-UI	2.210	0.731-6.678	0.160
Pre-LSMG- UI	1.270	0.443-3.636	0.656

Pre-RPG-UI, pre-treatment right parotid gland uptake; Pre-LPG-UI, pre-treatment left paro-tid gland uptake; Pre-RSMG-UI, pre-treatment right submandibular gland uptake; Pre-LSMG-UI, pre-treatment left submandibular gland uptake.

ression analysis revealed that parotid dysfunction 8 months after treatment was not associated with the ^{131}I dose (OR= 0.9959; P=0.536). Furthermore, no statistically significant differences were observed in the incidence of parotid dysfunction between varying doses of ^{131}I, as indicated by the χ^2 test (P=0.658) and the χ^2 test for trend (P=0.554). They indicated that variables other than dosage contribute to salivary gland dysfunction, such as individual glandular uptake capacity, retention time, gland size, radiosensitivity, and post-therapeutic protective strategies. This study observed a strong correlation between pre-treatment uptake levels and post-treatment decreases, underscoring the critical role of glandular uptake in the mechanism of salivary gland damage. Lee et al. (2013) also found that the initial uptake intensity of ^{131}I in salivary glands was associated with the risk of glandular damage rather than the clearance rate of ^{131}I, which aligns with our research findings [26]. In this study, Pre-UI was used to predict moderate to severe salivary gland dysfunction (ΔUI%>20%) after ^{131}I treatment, and the predictive sensitivity of RPG, LPG, RSMG, and LSMG reached 79.7%, 84.2%, 84.9%, and 90.1%, respectively.

In our study, 6.5% (39/596) of glands exhibited a change from a Pre-EF > 0 to a Post-EF <0, indicating an increase in $^{99m}TcO_4^-$ accumulation following acid stimulation, a phenomenon typically induced by ^{131}I therapy [27]. In human salivary glands, the NIS is predominantly expressed in ductal cells, not in acinar cells [24]. Iodine-131 concentrates in the ductal system, where beta radiation can cause damage leading to ductal narrowing due to luminal fragmentation, potentially resulting in ductal obstruction and subsequent damage [16]. This obstruction may cause retention of secreted saliva within the ducts, triggering salivary gland inflammation. Technetium-99m-pertechnetate uptake and washout reflect the functions of the parenchyma and ducts, respectively [28]. Since radiation primarily damages ductal walls, leading to subsequent vascular fibrosis, salivary excretion could be impaired earlier and more severely than parenchymal uptake at early stages [23]. Previous research suggested the parotid gland is more vulnerable to ^{131}I therapy due to higher concentrations of radiation-sensitive serous cells, unlike the submandibular gland, which contains both mucous and serous cells, possibly offering some radiation protection [14]. Contrary to these findings, this study observed more pronounced uptake function impairment in the submandibular glands, challenging previous conclusions. This difference may be linked to the timing of iodine intake and subsequent activities, including ingestion time, hydration, and spontaneous glandular secretion. In this study, almost all patients always ingested ^{131}I at 4pm and began resting around 10pm; the submandibular gland is responsible for the majority of saliva secretion during rest, might accumulate higher radiation doses due to prolonged periods without stimulation, leading to increased radiation absorption [3, 24, 29]. Jo KS et al. (2014) also found that the submandibular gland accumulated more radioactive ^{131}I after treatment, but the reason is uncertain [23]. The absorbed radiation dose to an organ is directly related to the amount taken up by the organ and the duration of radiation that remains in that organ but is inversely related to the volume of the organ [30]. Therefore, higher NIS expression and the smaller size of the submandibular gland could result in greater radiation exposure than the parotid gland. In addition, the measurement of submandibular gland uptake is easily affected by residual uptake from the strong thyroid gland, which may affect the results of quantitative analysis [26].

In terms of xerostomia, 38.9% (58/149) of patients in this study experienced moderate to extreme xerostomia, a percentage similar to that reported in the literature [31, 32]. Significant differences were observed in xerostomia complaints (P=0.015) and XI scores (P=0.008) among different ^{131}I treatment dose groups, indicating that higher doses of ^{131}I were associated with more severe xerostomia. Hollingsworth B et al. (2016) reported that the mean cumulative ^{131}I activity was (1.702GBq) higher in patients with xerostomia than in patients without xerostomia, and the mean first administration ^{131}I activity was (0.777GBq) higher than in patients without xerostomia [33]. These findings suggest that while general characteristics remain similar, higher doses may lead to increased dry mouth symptoms, highlighting the need for further research to manage these side effects effectively. Notably, there were significant differences in the Pre-UI and ΔUI% of bilateral submandibular glands between patients without mild dry mouth symptoms and those with moderate to severe dry mouth symptoms, suggesting that the uptake function of bilateral submandibular glands before treatment and the degree of their damage may have a significant impact on dry mouth symptoms. This is similar to previous reports that dysfunction of the submandibular gland might be closely related to dry mouth symptoms [14, 34]. In our study, the pre-treatment uptake function of the submandibular gland was an important influencing factor for xerostomia after ^{131}I treatment. The higher the Pre-UI value, the higher the incidence of xerostomia after treatment. This may be related to the significant decrease of submandibular gland uptake function caused by the increase of ^{131}I dose in the gland due to high uptake function. Although most patients with submandibular and parotid gland dysfunction report dry mouth, there are also a few patients who do not have symptoms, and the absence of apparent dry mouth symptoms in these patients may result from the compensatory function of other salivary glands [35]. About 90% of saliva is produced by the three pairs of significant salivary glands (parotid gland, submandibular gland, and sublingual gland). The remaining 10% is produced by hundreds of minor salivary glands widely scattered throughout the oral mucosa [36]. The small (minor) salivary glands produce 70% of the mucin in saliva, crucial for maintaining mucosal lubrication and oral comfort. The sublingual gland and submandibular gland produce the remaining mucin. Evidence shows that although patients receiving radiation therapy for laryngeal cancer have radiation doses exceeding the tolerated dose to their parotid and submandibular glands, their complaints about dry mouth are lower because the function of small oral glands is protected. In comparison, there are more complaints about dry mouth after radiation therapy for oropharyngeal and nasopharyngeal cancer [37]. Future studies should include more sophisticated analyses and control for confounding variables to understand these relationships better. The results also indicated that the lack of a significant change in EF in the submandibular glands between the groups with and without xerostomia might appear to be inconsistent with the observed association between higher UI and increased risk of xerostomia. The reason may be the following: (1) Differentiating uptake and secretion functions: While uptake (UI) and secretion (EF) are closely related, they assess different aspects of salivary gland function. A reduction in uptake capacity may lead to glandular dysfunction, even if secretion remains relatively unaffected. Submandibular glands with higher pre-treatment UI values are more vulnerable to radiation-induced damage, which primarily affects their ability to accumulate iodine (i.e., impaired uptake). However, this dysfunction may not immediately result in a detectable decline in secretion (EF), which is more directly linked to the gland's ability to release saliva in response to stimulation. In this case, a decline in uptake may be an early sign of dysfunction, preceding any noticeable changes in secretion; (2) Impact of radiation on glandular tissue: The impairment in UI suggests that the submandibular glands are absorbing more ^{131}I, which can cause radiation-induced damage to glandular tissue, particularly the ductal system. This damage, often characterized by ductal narrowing and potential blockages, may not be reflected in EF, which primarily measures the gland's secretion capacity under stimulation. Therefore, even though the ability to concentrate on iodine is reduced, this does not necessarily translate into an immediate or measurable decline in saliva secretion, especially in the early post-treatment phase. (3) Threshold effects and compensatory mechanisms: Xerostomia could be related to a threshold effect, where even small or subclinical impairments in glandular function, such as reduced uptake, are sufficient to trigger dry mouth symptoms, even if secretion remains relatively unaffected. Furthermore, other salivary glands may compensate for the loss of function in the submandibular glands, which could help alleviate the subjective experience of xerostomia in the short term. This compensatory effect might mask the early stages of secretion dysfunction, even when there are significant changes in uptake function.

There are certain limitations to the present study. Firstly, in our study, individual gland evaluation is used, because different salivary glands have distinct functional properties, and in clinical practice, there is currently no universally defined metric that combines the function of all salivary glands. Future study could analyze an aggregate metric representing overall salivary gland function may provide a more holistic perspective Secondly, patients with higher pre-therapy uptake index (Pre-UI) values exhibit greater declines in uptake function (ΔUI%) post-therapy. This outcome may be expected, as glands with higher initial uptake are inherently more likely to experience larger proportional decreases. However, we argue that this does not undermine the predictive utility of Pre-UI. In fact, it reinforces its importance as a tool for identifying glands at higher risk of significant damage. By recognizing glands with stronger baseline uptake, clinicians can better stratify risk and implement more targeted interventions to mitigate the impact of RAI therapy. Therefore, while the relationship between Pre-UI and ΔUI% may reflect a natural tendency, it remains a valuable predictor for anticipating salivary gland dysfunction and guiding patient management. Thirdly, the study was conducted at a single center with a small patient cohort, which may introduce selection bias and limit the generalizability of the findings. In our analysis, we conducted univariate regression analyses for each salivary gland, given that only Pre-UI was identified as a significant factor in the univariate analyses, we did not proceed with multivariate logistic regression. To further explore the factors influencing ΔUI% and salivary gland dysfunction, performing a multivariate logistic regression analysis may be better, future study may be needing larger samples and multiple centersto conduct a more stability analysis. Fourthly, the overall low administered radioiodine activities in our cohort might explain the absence of a clear activity-dependent relationship in salivary gland impairment. Finally, the present study did not observe an activity- dependent salivary gland impairment, and the overall low administered activity. Sialagogues stimulate salivary flow, potentially enhancing iodine retention in the glands during the critical period of high radiation exposure, thereby increasing the absorbed dose and exacerbating glandular damage. However, in our study, the timing and frequency of sialagogue use were not systematically recorded, limiting our ability to directly evaluate its impact. This may play a role, it does not fully account for the observed widespread functional decline across all salivary glands. The frequent decline in gland function is likely a result of the interplay between higher baseline uptake capacity and cumulative radiation effects, potentially amplified by the timing of sialagogue use.

In conclusion, our finding that the Pre-UI of the salivary glands correlates with a decrease in ΔUI% after RAI therapy in DTC patients is of clinical significance. This finding indicates that pre-treatment $^{99m}TcO_4^-$ SGS can be a predictive tool for identifying patients at risk of severe salivary gland dysfunction, facilitating close monitoring and proactive preventive strategies. Thus, pre-treatment SGS effectively predicts severe salivary gland dysfunction, allowing for targeted interventions in high-risk DTC patients.

The authors declare that they have no conflicts of interest.

Ethics approval and consent to participate

The research protocol was approved by the Ethical Committee of Xuzhou Medical University Affiliated Hospital. A comprehensive overview of the study procedures was presented to all participants, who subsequently provided their written informed consent.

Funding

This work was supported by Changzhou Clinical Medical Center (Nuclear Medicine) (CZZX202204, PI: Yuetao Wang), Clinical Medical Science and Technology High-end Platform and Transformation Base Construction Project of Soochow University (Characteristic Discipline)-Nuclear Medicine (PI: Yuetao Wang), Outstanding Talent of Changzhou "The 14th Five-Year Plan" High-Level Health Talents Training Project (2022-260, PI: Yuetao Wang).

Bibliography

1. Siegel RL, Miller KD, Fuchs HE et al. Cancer Statistics, 2021. *CA Cancer J Clin* 2021; 71 (1):7-33.
2. Filetti S, Durante C, Hartl D et al. Thyroid cancer: ESMO Clinical Practice Guidelines for diagnosis, treatment and follow-up†. *Ann Oncol* 2019; 30(12): 1856-83.
3. Son SH, Lee CH, Jung JH et al. The Preventive Effect of Parotid Gland Massage on Salivary Gland Dysfunction During High-Dose Radioactive Iodine Therapy for Differentiated Thyroid Cancer: A Randomized Clinical Trial. *Clin Nucl Med* 2019; 44 (8): 625-33.
4. Vazão AR, Claudino L, Pimpinato PP et al. Experimental apical periodontitis alters salivary biochemical composition and induces local redox state disturbances in the salivary glands of male rats. *Clin Oral Investig* 2024; 28 (2): 154.
5. Van Nostrand D. Sialoadenitis secondary to ^{131}I therapy for well-differentiated thyroid cancer. *Oral Dis* 2011; 17(2): 154-61.
6. Baudin C, Lussey-Lepoutre C, Bressand A et al. Salivary Dysfunctions and Consequences After Radioiodine Treatment for Thyroid Cancer: Protocol for a Self-Controlled Study (START Study). *JMIR Res Protoc* 2022; 11(7): e35565.
7. Liu Y, Ding H, Zhang T et al. ^{68}Ga-DOTA-Ibandronic Acid PET/CT in a Patient With Chemotherapy-Induced Salivary Gland Hypofunction. *Clin Nucl Med* 2024; 49(5): 470-1.
8. Campagna G, Anzola LK, Varani M et al. Imaging Activated-T-Lymphocytes in the Salivary Glands of Patients with Sjögren's Syndrome by ^{99m}Tc-Interleukin-2: Diagnostic and Therapeutic Implications. *J Clin Med* 2022; 11(15): 4368.
9. Maruoka Y, Baba S, Isoda T et al. A Functional Scoring System Based on Salivary Gland Scintigraphy for Evaluating Salivary Gland Dysfunction Secondary to ^{131}I therapy in Patients with Differentiated Thyroid Carcinoma. *J Clin Diagn Res* 2017; 11(8): Tc23-Tc28.
10. Haugen BR, Alexander EK, Bible KC et al. 2015 American Thyroid Association Management Guidelines for Adult Patients with Thyroid Nodules and Differentiated Thyroid Cancer: The American Thyroid Association Guidelines Task Force on Thyroid Nodules and Differentiated Thyroid Cancer. *Thyroid* 2016; 26(1): 1-133.
11. Upadhyaya A, Meng Z, Wang P et al. Effects of first radioiodine ablation on functions of salivary glands in patients with differentiated thyroid cancer. *Medicine (Baltimore)* 2017; 96(25): e7164.
12. Fallahi B, Beiki D, Abedi SM et al. Does vitamin E protect salivary glands from ^{131}I radiation damage in patients with thyroid cancer? *Nucl Med Commun* 2013; 34(8): 777-86.
13. Selvakumar T, Nies M, Klein Hesselink MS et al. Long-term effects of radioiodine treatment on salivary gland function in adult survivors of pediatric differentiated thyroid carcinoma. *J Nucl Med* 2018; jnumed. 118.212449.
14. Jeong SY, Kim HW, Lee SW et al. Salivary gland function 5 years after radioactive iodine ablation in patients with differentiated thyroid cancer: direct comparison of pre- and postablation scintigraphies and their relation to xerostomia symptoms. *Thyroid* 2013; 23(5): 609-16.
15. Yang L, Ma J, Lei P et al. Advances in Antioxidant Applications for Combating ^{131}I Side Effects in Thyroid Cancer Treatment. *Toxics* 2023; 11(6): 529.
16. Klein Hesselink EN, Brouwers AH, de Jong JR et al. Effects of Radioiodine Treatment on Salivary Gland Function in Patients with Differentiated Thyroid Carcinoma: A Prospective Study. *J Nucl Med* 2016; 57(11): 1685-91.
17. Kim JW, Han GS, Lee SH et al. Sialoendoscopic treatment for radioiodine induced sialadenitis. *Laryngoscope* 2007; 117(1): 133-6.
18. Kim YM, Choi JS, Hong SB et al. Salivary gland function after sialendoscopy for treatment of chronic radioiodine-induced sialadenitis. *Head Neck* 2016; 38(1): 51-8.
19. Badam RK, Suram J, Babu DB et al. Assessment of Salivary Gland Function Using Salivary Scintigraphy in Pre and Post Radioactive Iodine Therapy in Diagnosed Thyroid Carcinoma Patients. *J Clin Diagn Res* 2016; 10(1): Zc60-62.
20. Wu JQ, Feng HJ, Ouyang W et al. Systematic evaluation of salivary gland damage following ^{131}I therapy in differentiated thyroid cancer patients by quantitative scintigraphy and clinical follow-up. *Nucl Med Commun* 2015; 36(8): 819-26.
21. Clement SC, Peeters RP, Ronckers CM et al. Intermediate and long-term adverse effects of radioiodine therapy for differentiated thyroid carcinoma--a systematic review. *Cancer Treat Rev* 2015; 41(10): 925-34.
22. Solans R, Bosch JA, Galofré P et al. Salivary and lacrimal gland dysfunction (sicca syndrome) after radioiodine therapy. *J Nucl Med* 2001; 42(5): 738-43.
23. Jo KS, An YS, Lee SJ et al. Significance of Salivary Gland Radioiodine Retention on Post-ablation ^{131}I Scintigraphy as a Predictor of Salivary Gland Dysfunction in Patients with Differentiated Thyroid Carcinoma. *Nucl Med Mol Imaging* 2014; 48(3): 203-11.
24. La Perle KM, Kim DC, Hall NC et al. Modulation of sodium/iodide symporter expression in the salivary gland. *Thyroid* 2013; 23(8): 1029-36.
25. Grewal RK, Larson SM, Pentlow CE et al. Salivary gland side effects commonly develop several weeks after initial radioactive iodine ablation. *J Nucl Med* 2009; 50(10): 1605-10.
26. Lee SM, Lee JW, Kim SY et al. Prediction of risk for symptomatic sialadenitis by post-therapeutic dual ^{131}I scintigraphy in patients with differentiated thyroid cancer. *Ann Nucl Med* 2013; 27(8): 700-9.
27. Mandel SJ, Mandel L. Radioactive iodine and the salivary glands. *Thyroid* 2003; 13(3): 265-71.
28. Kim JW, Kim JM, Choi ME et al. Does Salivary Function Decrease in Proportion to Radioiodine Dose? *Laryngoscope* 2020; 130(9): 2173-8.
29. Holmberg KV, Hoffman MP. Anatomy, biogenesis and regeneration of salivary glands. *Monogr Oral Sci* 2014; 24: 1-13.
30. Lee SL. Complications of radioactive iodine treatment of thyroid carcinoma. *J Natl Compr Canc Netw* 2010; 8(11): 1277-1286; quiz 1287.
31. Nakada K, Ishibashi T, Takei T et al. Does lemon candy decrease salivary gland damage after radioiodine therapy for thyroid cancer? *J Nucl Med* 2005; 46(2): 261-6.
32. Christou A, Papastavrou E, Merkouris A et al. Clinical Studies of Non-pharmacological Methods to Minimize Salivary Gland Damage after Radioiodine Therapy of Differentiated Thyroid Carcinoma: Systematic Review. *Evid Based Complement Alternat Med* 2016; 2016: 6795076.
33. Hollingsworth B, Senter L, Zhang X et al. Risk Factors of ^{131}I-Induced Salivary Gland Damage in Thyroid Cancer Patients. *J Clin Endocrinol Metab* 2016; 101(11): 4085-93.
34. Caglar M, Tuncel M, Alpar R. Scintigraphic evaluation of salivary gland dysfunction in patients with thyroid cancer after radioiodine treatment. *Clin Nucl Med* 2002; 27(11): 767-71.
35. Raza H, Khan AU, Hameed A et al. Quantitative evaluation of salivary gland dysfunction after radioiodine therapy using salivary gland scintigraphy. *Nucl Med Commun* 2006; 27(6): 495-9.
36. Adramerinas M, Andreadis D, Vahtsevanos K et al. Sialadenitis as a complication of radioiodine therapy in patients with thyroid cancer: where do we stand? *Hormones (Athens)* 2021; 20(4): 669-78.
37. Wijers OB, Levendag PC, Braaksma MM et al. Patients with head and neck cancer cured by radiation therapy: a survey of the dry mouth syndrome in long-term survivors. *Head Neck* 2002; 24(8): 737-47.

^{18}F-FDG PET/CT parameters as therapy response predictors in patients with diffuse large B-cell lymphoma: A single centre experience

Milica Kotur[1] **MD,**
Nikola Pantić[1] **MD,**
Isidora Grozdić Milojević[1,2] **MD, PhD,**
Amin Mehmedović[2] **MD,**
Nikola Andrejić[2] **MD,**
Milica Stojiljković[1,2] **MD, PhD,**
Jelena Petrović[1,2] **MD, PhD,**
Dragana Šobić Šaranović[1,2] **MD, PhD,**
Vera Artiko[1,2] **MD, PhD,**
Strahinja Odalović[1,2] **MD, PhD**

1. Center for Nuclear Medicine with PET, University Clinical Center of Serbia, Belgrade, Serbia
2. Faculty of Medicine, University of Belgrade, Belgrade, Serbia

Keywords: DLBCL
-^{18}F-FDG PET/CT
- International prognostic index
- Deauville score
- Progression free survival

Corresponding author:
Milica Kotur MD,
University Clinical Center of Serbia, Center for Nuclear Medicine with PET, Višegradska 26, 11000 Belgrade, Serbia
Tel: +381694684866,
Fax: +381113615641
koturmilica99@gmail.com

Received:
13 January 2025
Accepted revised:
5 May 2025

Abstract

Objective: The aim of this study is to determine the importance of different fluorine-18-fluorodeoxyglucose (^{18}F-FDG) positron emission tomography with computed tomography (PET/CT) semi-quantitative and quantitative parameters, as well as various clinical and demographic parameters, in predicting disease outcomes and response to therapy in patients with diffuse large B-cell lymphoma (DLBCL). **Subjects and Methods:** The study included 64 patients diagnosed with DLBCL who underwent ^{18}F-FDG PET/CT imaging between January 2020 and April 2023. Each patient underwent both an initial ^{18}F-FDG PET/CT and an interim ^{18}F-FDG PET/CT after 2 or 4 cycles of chemotherapy. The Deauville score (DS) was calculated for each patient. Progression-free survival (PFS) was defined as the time from the date of diagnosis to the first appearance of metabolic or morphological progression of pre-existing lesions and/or the appearance of new lesions detected on interim ^{18}F-FDG PET/CT or follow-up radiological imaging, as well as in cases of death due to the underlying disease or until the end of the clinical follow-up period. **Results:** Among the clinical-demographic parameters analyzed, the only significant predictive factor was the international prognostic index (IPI) score, categorized by group. Of the ^{18}F-FDG PET/CT parameters examined, DS showed strong statistical significance in both univariate and multivariate analyses. While maximum standardized uptake value (SUVmax) and peak SUV (SUVpeak) were statistically significant in the univariate analysis. Progression-free survival was longer in patients with an IPI ≤2 and DS ≤3, compared to those with higher IPI and DS. **Conclusions:** The results of this study showed that the early metabolic response to therapy assessed on the basis of interim ^{18}F-FDG PET/CT is a significant independent predictive factor for disease outcome in patients with DLBCL.

Hell J Nucl Med 2025; 28(2): 115-123

Introduction

Diffuse large B-cell lymphoma (DLBCL), the most prevalent subtype of non-Hodgkin lymphoma (NHL) accounts for 31% of NHL cases in Western countries, and 37% of all global B-cell tumors [1]. Since 2011, the annual mortality rate for DLBCL has risen by more than 3.5% each year, making it the most prevalent aggressive lymphoma in adults [2, 3].

At the beginning of DLBCL, the International Prognostic Index (IPI) was important for predicting outcomes and deciding on treatments, as it was created to assess risk in aggressive lymphomas before the use of rituximab [4]. The IPI takes into account five clinical criteria: age of the patient, lymphoma stage, Eastern Cooperative Oncology Group (ECOG) score, LDH values, and number of extranodal lesions [4].

Over time, fluorine-18-fluorodeoxyglucose (^{18}F-FDG) positron emission tomography (PET) in combination with computed tomography (CT) has become an essential method for assessing lymphoma at the time of diagnosis and is now regarded as the standard approach [5]. Because of its high sensitivity in identifying both nodal and extranodal manifestations of lymphoma, ^{18}F-FDG PET/CT is highly recommended for staging patients with DLBCL [6]. Using ^{18}F-FDG PET/CT, it is possible to determine the initial stage of the disease, as well as predict the effectiveness of therapy on control ^{18}F-FDG PET/CT imaging after two or four cycles of chemotherapy [7].

According to the Lugano classification, the Deauville five-point scale (DS) is the recommended method for assessing treatment response using ^{18}F-FDG PET/CT [8]. In 2009, DS was introduced to meet the growing need for simple and reproducible ^{18}F-FDG PET/CT interpretation in the setting of early response assessment [9]. By visually comparing the ^{18}F-FDG uptake in lesions to that in the reference regions, such as the mediastinal blood pool and liver, the scale categorizes residual tissue from 1 to 5 [5].

One of the important features of ^{18}F-FDG PET/CT is the determination of semi-quantitative and quantitative parameters: maximum and peak standardized uptake value (SUVmax and SUVpeak); total lesion glycolysis (TLG); metabolic tumor volume (MTV). High SUV values are generally associated with more aggressive types of lymphoma [10].

The aim of this study is to determine the importance of different ^{18}F-FDG PET/CT semi-quantitative and quantitative parameters, as well as various clinical and demographic parameters, in predicting disease outcomes and response to therapy in patients with DLBCL.

Subjects and Methods

Patients

The study included patients diagnosed with DLBCL who underwent ^{18}F-FDG PET/CT imaging between January 2020 and April 2023. Inclusion criteria were: patients who had pathohistologically confirmed DLBCL; without any therapy before initial ^{18}F-FDG PET/CT imaging; underwent initial ^{18}F-FDG PET/CT scan and control one after 2 or 4 cycles of chemotherapy; 18 years of age or older; without another malignant disease; with complete clinical and biochemical records. The criteria for exclusion from the study were patients who received chemotherapy, radiotherapy, or surgical resection before the initial ^{18}F-FDG PET/CT scan; patients in whom no interim ^{18}F-FDG PET/CT imaging was performed; patients who were lost to follow-up. Finally, a total of 64 patients were enrolled in this study. The mean follow-up period was 15.7 months. Clinical and demographic data (age, sex, Ann Arbor staging, IPI score, LDH level, and extranodal involvement) were obtained from the medical records.

This study was conducted in accordance with the 1964 Helsinki declaration for ethical standards. The approval of the ethics committee was obtained by the ethics committee of the University Clinical Center of Serbia. Written informed consent was obtained from each patient included in the study.

^{18}F-FDG PET/CT imaging procedure and data acquisition

All patients underwent ^{18}F-FDG PET/CT examinations on a 64-slice Biograph True64 PET/CT hybrid scanner (Siemens Medical Solutions USA Inc, Malvern, PA, USA). The patients fasted for a minimum of 6 hours before the intravenous application of FDG (5.5MBq/kg of body weight). Before applying ^{18}F-FDG, glycemia was measured in each patient. If the glycemia was above 11mmol/L, the scan was postponed until regulation. This was followed by a rest period of at least 60 minutes from the application of the radiopharmaceutical until the beginning of the acquisition. The patients were first subjected to a low-dose multidetector CT imaging, which was used for attenuation correction and topographical localization. This examination was performed without the application of intravenous contrast agent, with the following CT parameters: voltage 120kV, current strength 45mAs, slice thickness 5mm, pitch 1.5, and rotation time of 0.5s. The PET acquisition followed immediately after that. The acquisition of 3D PET was carried out in the standard "whole-body" modality, from the base of the skull to the proximal third of the femur, pulses were collected from 6-7 bed positions (depending on the height of the patient) for three minutes each.

Qualitative and quantitative ^{18}F-FDG PET/CT analysis

After the low-dose multidetector CT and PET acquisition, the data were reconstructed using the standard statistical reconstruction method (ordered subsets expectation maximization-OSEM), and the obtained data were analyzed on a SYNGO workstation (Syngo 2008B, Siemens, Medical Systems, Erlangen, Germany). When interpreting the findings, individual PET and CT images were analyzed, and then fused PET/CT images were created, along with a rotating view in 3D mode (maximum intensity projection). The images were first analyzed qualitatively, in the form of visual interpretations, and then the following ^{18}F-FDG PET/CT semi-quantitative and quantitative parameters of the most metabolically active lesion were assessed: SUVmax, SUVpeak, MTV, and TLG.

Interim treatment response evaluation

In all patients included in the study, an interim ^{18}F-FDG PET/CT examination was performed under the same conditions as the initial ^{18}F-FDG PET/CT scan. The interim ^{18}F-FDG PET/CT scan was used to assess the morphological and metabolic response to therapy. Deauville five-point scale was calculated for each patient. The DS comprises 5 categories, which are defined as: score 1-no uptake above background; score 2-residual uptake not exceeding mediastinal uptake; score 3-residual uptake above mediastinal but not exceeding liver uptake; score 4-residual uptake above liver uptake; and score 5-residual uptake markedly above liver uptake or new lesions.

Follow-up assessment

In all patients included in the study, follow-up was conducted through clinical reports. Progression-free survival (PFS) was defined as the time from the date of diagnosis (data obtained from medical records) to the date of the first appearance of metabolic or morphological progression of initial lesions and/or the appearance of new lesions detected on interim ^{18}F-FDG PET/CT or follow-up radiological imaging, or death due to the underlying disease, or until the end of the clinical follow-up period. The maximum follow-up period was 18 months.

Statistical analysis

The methods of descriptive and analytical statistics were used in the statistical analysis. A database of patients included in the study was created in the Excel program. Regarding clinical-demographic parameters, all patients were categorized into 2 groups: sex (male/female), age (≤60 and >60), Ann Arbor stage (≤2 and >2), IPI score (≤2 and >2), and LDH (normal/abnormal). For each semi-quantitative and quantitative ^{18}F-FDG PET/CT parameter, the median was calculated, based on which value the patients were divided into two groups: SUVmax (≤13.4 and >13.4), SUVpeak (≤10.2 and >10.2), MTV (≤9.8 and >9.8), and TLG (≤43.2 and >43.2) on initial ^{18}F-FDG PET/CT, as well as DS on interim ^{18}F-FDG PET/CT (≤3 and >3).

Examination of the association between the clinical-demographic parameters, semi-quantitative and quantitative ^{18}F-FDG PET/CT parameters with PFS was performed using Cox regression univariate and multivariate analysis. In determining the difference in PFS between different groups of patients, survival curves were constructed using the Kaplan-Meier method.

All statistical analyses were conducted using the EZR software. All values of $P<0.05$ were considered statistically significant.

Results

Patient characteristics

The clinical and demographic characteristics of 64 patients included in the study are presented in Table 1. The mean age of the patients was 53.8 (range, 20-84).

Initial ^{18}F-FDG PET/CT Imaging

The initial ^{18}F-FDG PET/CT scan revealed pathological accumulation of 18F-FDG in all patients (Figure 1). The most common localizations of intense pathological accumulation of ^{18}F-FDG were the supradiaphragmatic and infradiaphragmatic lymph nodes, followed by the spleen, bones and tonsils, muscles, lungs, and prostate. The site of the most metabolically active lesion was determined based on the SUVmax value (Table 2).

In subsequent analyses, additional semi-quantitative and quantitative parameters (SUVpeak, MTV, TLG) of the most active lesions were assessed. Based on the median values of these parameters, patients were categorized into two groups: those with values equal to or below the median, and those with values above the median for each respective parameter (Table 3).

Interim ^{18}F-FDG PET/CT imaging

All patients included in the study underwent an interim ^{18}F-FDG PET/CT scan after 2 or 4 cycles of chemotherapy (Figure 2). In each patient, the DS value was determined, after which the patients were categorized into two groups based on the value (DS ≤3 and >3). A total of 31 patients had DS ≤3 (DS 1, 2, or 3), while 33 patients had DS >3 (DS 4 or 5) (Table 3).

Univariate and multivariate analysis

Cox regression analysis was used to examine the relationship between clinical-demographic parameters (sex, age, Ann Arbor stage, IPI score, localization, extranodal involvement and LDH) and ^{18}F-FDG PET/CT semi-quantitative and

Table 1. *Demographic and clinical characteristics of the 64 patients with DLBCL.*

Parameter		Number of patients	Percentage (%)
Sex	Female	31	48.4
	Male	33	51.6
Age	(x̄±SD) 53.8±18.1		
	≤60	32	50
	>60	32	50
Ann Arbor	≤2	27	42.2
	>2	37	57.8
IPI	≤2	28	43.8
	>2	36	56.2
Extranodal involvement	Yes	46	71.9
	No	18	28.1
LDH	Normal	24	37.5
	Abnormal	40	62.5

DLBCL: Diffuse large B-cell lymphoma, IPI: International Prognostic Index, LDH: lactate dehydrogenase

Table 2. *Localization of the most metabolically active lesion based on the SUVmax value in 64 patients with DLBCL.*

The location of the most metabolically intensive lesion	Number of patients	Percentage (%)
Lymph nodes	**46**	**71.9**
Head and neck	6	9.4
Mediastinum	20	31.3
Axial	2	3.1
Abdomina/inguinal	18	28.1
Extranodal	**18**	**28.1**
Spleen	5	7.8
Bone	4	6.2
Tonsils	3	4.7
Muscle	3	4.7
Lungs	2	3.1
Prostate	1	1.6

DLBCL: Diffuse large B-cell lymphoma

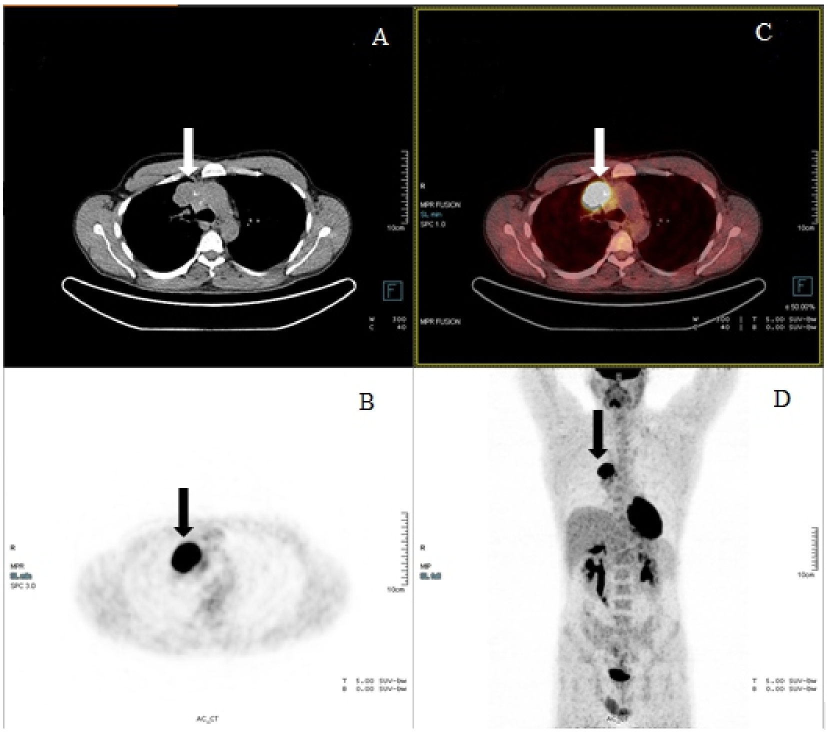

Figure 1. Initial ^{18}F-FDG PET/CT scan in a patient with DLBCL; axial section on non-contrast, low-dose CT (A); PET (B); fusion PET/CT (C) and maximum intensity projection (MIP) (D); in which arrows point to a change in the mediastinum with intensively increased ^{18}F-FDG accumulation, representing active disease.

Table 3. *Categorization of 64 DLBCL patients based on median values of semi-quantitative and quantitative parameters at initial and interim ^{18}F-FDG PET/CT examination.*

^{18}F-FDG PET/CT parameter		Number of patients	Percentage (%)
SUVmax	Med (min-max) 13.4 (4-46.7)		
	≤13.4	33	51.6
	>13.4	31	48.4
SUVpeak	Med (min-max) 10.2 (2.6-39)		
	≤10.2	32	50
	>10.2	32	50
MTV	Med (min-max) 9.8 (2.1-1168.7)		
	≤9.8	32	50
	>9.8	32	50
TLG	Med (min-max) 43.2 (6.1-1560.2)		
	≤43.2	32	50
	>43.2	32	50
DS	≤3	31	48.4
	>3	33	51.6

DLBCL: Diffuse large B-cell lymphoma, ^{18}F-FDG: fluorine-18-fluorodeoxyglucose, PET: Positron Emission Tomography, SUV: Standardized Uptake Value, MTV: Metabolic Tumor Volume, TLG: Total Lesion Glycolysis, DS: Deauville score

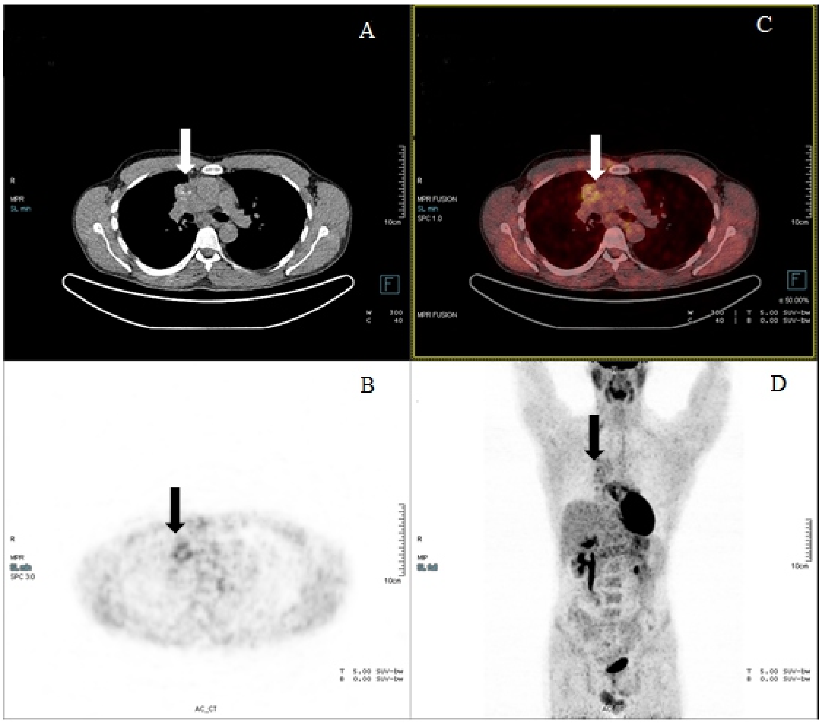

Figure 2. Interim ^{18}F-FDG PET/CT scan in a patient with DLBCL, axial section on non-contrast, low-dose CT (A); PET (B); fusion PET/CT (C) and MIP (D); In which arrows point to a change in the mediastinum with moderately increased ^{18}F-FDG accumulation, with metabolic and morphological regression compared to the initial ^{18}F-FDG PET/CT; DS 3 (shown in Figure 1).

quantitative parameters (SUVmax, SUVpeak, MTV, and TLG of the most active lesions and DS) with PFS in DLBCL patients.

In the univariate analysis, the association between clinical-demographic parameters and PFS in patients with DLBCL was assessed. The effects of the individual IPI score and the IPI score grouped into two categories were analyzed (one group includes patients with an IPI ≤2, and the other consisted of patients with an IPI >2). The results showed that the grouped IPI score was significantly associated with disease progression. Patients with an IPI score of 1 or 2 had a longer PFS compared to those with an IPI score of 3, 4, or 5 ($P=0.003$). In contrast, the individual IPI score, as well as other clinical and demographic parameters, did not show a statistically significant effect on PFS ($P>0.05$) (Table 4). Multivariate analysis also revealed no significant association between the clinical and demographic parameters and disease progression ($P>0.05$) (Table 5).

Univariate analysis was also used to examine the association between ^{18}F-FDG PET/CT parameters and disease progression in patients with DLBCL. The results showed that the SUVmax and SUVpeak parameters were significant predictors of disease progression ($P=0.035$ and $P=0.043$), as well as DS, which demonstrated a strong statistical association with disease progression ($P<0.001$). However, in the multivariate analysis, only DS remained strong statistically significant ($P<0.001$), while SUVmax and SUVpeak lost their significance due to the dominance of DS. The MTV and TLG parameters were not statistically significant in either univariate or multivariate analysis. The results of univariate and multivariate analyses of ^{18}F-FDG PET/CT parameters in 64 patients with DLBCL can be found in Tables 6 and 7.

Analysis of differences in PFS

In the subsequent analysis, differences in PFS between groups of patients divided into groups based on IPI score and DS on interim ^{18}F-FDG PET/CT imaging were evaluated using Kaplan-Meier survival analysis and log-rank test. Disease progression was observed in 29 (45.3%) patients. The mean time to disease progression was 12.9 months. The mean time PFS in patients who had an IPI ≤2 was 16.7, and in patients who had an IPI >2 was 14.9 months. Progression-free survival was significantly longer in patients who had an IPI ≤2 compared to those who had an IPI >2 (Kaplan-Meier, log-rank test, $P=0.003$) (Figure 3). The mean time PFS in patients who had DS ≤3 was 17.8, while the mean survival time in patients with DS >3 was 13.6 months. PFS was significantly longer in patients with DS ≤3 (Kaplan-Meier, log-rank test, $P<0.001$) (Figure 4).

Discussion

In this study, various clinical, demographic parameters, and ^{18}F-FDG PET/CT parameters, were analyzed to assess their influence on the therapy response and prediction on PFS in patients with DLBCL. The only significant factor among the clinical-demographic parameters was the IPI score, categorized by group. Of the ^{18}F-FDG PET/CT parameters, DS demonstrated strong statistical significance in both univariate and multivariate analyses while SUVmax and SUVpeak were found to be statistically significant only in univariate analysis. Progression-free survival was longer in patients with IPI≤2

Table 4. *Univariate analysis of demographic and clinical parameters of 64 patients with DLBCL.*

Parameter	P	HR	95.0% CI for Exp(B)	
			Lower	Upper
Sex	0.267	1.514	0.728	3.147
Age (by groups)	0.265	1.526	0.729	3.196
Age	0.264	1.525	0.728	3.195
Ann Arbor	0.150	1.325	0.903	1.944
Ann Arbor (by groups)	0.339	1.433	0.680	3.061
IPI	0.082	1.321	0.965	1.808
IPI (by groups)	0.003*	2.477	1.094	5.608
Localization	0.769	0.964	0.751	1.236
Extranodal involvement	0.767	0.884	0.392	1.996
LDH	0.155	1.808	0.799	4.090

DLBCL: Diffuse large B-cell lymphoma, IPI: International Prognostic Index, LDH: lactate dehydrogenase

Table 5. *Multivariate analysis of demographic and clinical parameters of 64 patients with DLBCL.*

Parameter	P	HR	95.0% CI for Exp(B)	
			Lower	Upper
Sex	0.488	1.310	0.610	2.813
Age	0.541	0.991	0.962	1.021
Ann Arbor	0.412	1.227	0.753	1.998
IPI	0.308	1.276	0.799	2.038
Extranodal involvement	0.637	1.264	0.477	3.350
LDH	0.178	1.778	0.770	4.105

DLBCL: Diffuse large B-cell lymphoma, IPI: International Prognostic Index, LDH: lactate dehydrogenase

Table 6. *Univariate analysis of ^{18}F-FDG PET/CT parameters of 64 patients with DLBCL.*

Parameter	P	HR	95.0% CI for Exp(B)	
			Lower	Upper
SUVmax	0.035*	1.029	1.002	1.056
SUVpeak	0.043*	1.033	1.001	1.066
MTV	0.647	1.000	0.998	1.001
TLG	0.271	0.999	0.997	1.001
DS	<0.001*	3.982	2.385	6.648

DLBCL: Diffuse large B-cell lymphoma, ^{18}F-FDG: fluorine-18-fluorodeoxyglucose, PET: Positron Emission Tomography, SUV: Standardized Uptake Value, MTV: Metabolic Tumor Volume, TLG: Total Lesion Glycolysis, DS: Deauville score

Table 7. *Multivariate analysis of ^{18}F-FDG PET/CT parameters of 64 patients with DLBCL.*

Parameter	P	HR	95.0% CI for Exp(B)	
			Lower	Upper
SUVmax	0.525	0.925	0.727	1.177
SUVpeak	0.351	1.151	0.856	1.547
MTV	0.918	0.998	0.997	1.000
TLG	0.119	0.996	0.991	1.001
DS	<0.001*	4.027	2.306	7.030

DLBCL: Diffuse large B-cell lymphoma, ^{18}F-FDG: fluorine-18-fluorodeoxyglucose, PET: Positron Emission Tomography, SUV: Standardized Uptake Value; MTV: Metabolic Tumor Volume, TLG: Total Lesion Glycolysis, DS: Deauville score

and DS ≤ 3 compared to those with higher IPI and DS.

The IPI score is an internationally recognized and widely used prognostic index in patients with DLBCL, typically assessed before the initiation of therapy [11, 12]. However, contradictory data exist in the literature, as some clinical studies suggest that while the IPI score can predict the prognosis in many DLBCL patients, patients with similar IPI scores often have differing long-term survival rates [13, 14]. Kwon et al. (2016) found that a higher IPI score was associated with significantly worse survival compared to IPI values of 1 and 2, which is consistent with the results of our study [15]. Additionally, in the univariate analysis, Ann Arbor stage, LDH, extranodal involvement and SUVmax values were predictive parameters for the disease in DLBCL patients, which is not in accordance with the results of our study. On the other hand, in the multivariate analysis, only the IPI showed prognostic statistical significance. The IPI is considered to retain its predictive significance when the score is 0 or 4-5, while it shows inconsistency in stratifying patients with intermediate scores, whose prognosis is often unclear and/or difficult to estimate, ranging from intermediate to poor prognostic predictions [16]. These findings suggest that other clinical parameters, the presence of comorbidities, and individual characteristics must also be considered when assessing response to chemotherapy and prognosis in DLBCL patients.

The results of our study indicate that patients with lower DS had a better prognosis and PFS. Several other studies have investigated the significance of DS, or the metabolic response to therapy, through interim ^{18}F-FDG PET/CT scans in patients with DLBCL. The Lugano criteria are used to assess

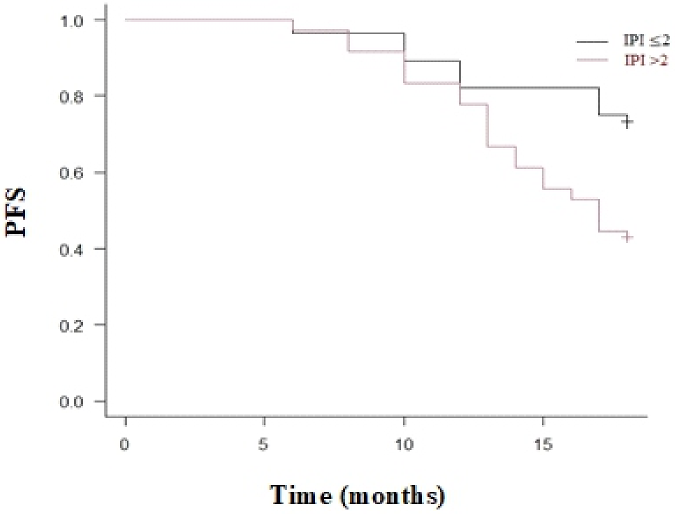

Figure 3. Kaplan-Meier survival analysis of PFS according to IPI (by groups). PFS: Progression-free survival; IPI: International prognostic ındex

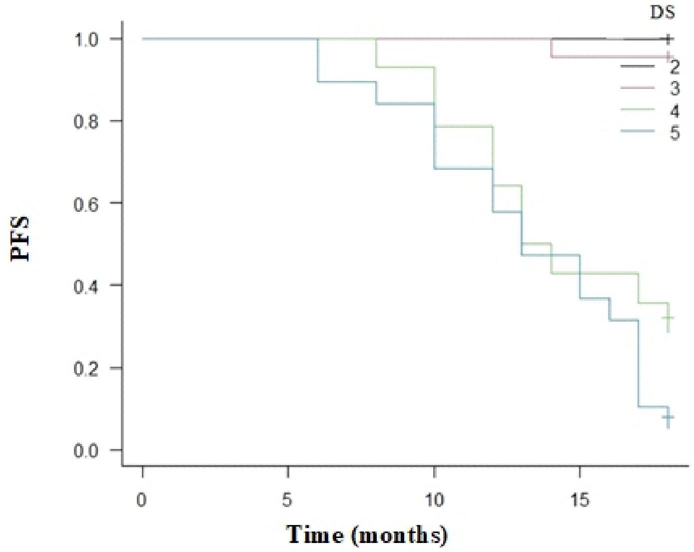

Figure 4. Kaplan-Meier survival analysis of PFS according to DS. PFS: Progression-free survival, DS: Deauville score

response to therapy based on DS, with a score ≤3 indicating a good metabolic response, while a DS of 4 or 5 is considered a poor metabolic response or metabolic progression [17]. Jin et al. (2021) demonstrated in their study that patients with DS ≤3 had a significantly longer PFS compared to those with DS >3 [18]. In line with these results, Allioux et al. (2021) reported significantly longer survival in patients who showed a good metabolic response to therapy (≤3), compared to those who had a poor metabolic response to therapy (DS 4 or 5) over a two-year period (P<0.0001). However, they also noted that no significant survival difference was observed between those with DS 4 and DS 5 [19]. One study found that the risk of disease progression, recurrence, and death within 2 years was significantly higher in patients who did not achieve a complete response (DS 4 or 5) compared to those who achieved a complete response (DS 1, 2, or 3) [20]. Poor interim treatment response is an indication for early clinical intervention, intensive treatment, or autologous stem cell transplantation [17]. Patients with a poor metabolic response to initial therapy have a higher risk of disease progression, relapse, and death due to the underlying disease. Therefore, with interim ^{18}F-FDG PET/CT examinations, determination DS and assessing metabolic response, it is possible to identify patients who have a greater chance of a worse prognosis of the disease, but also to find an adequate treatment strategy for them.

Other semi-quantitative and quantitative ^{18}F-FDG PET/CT parameters analyzed in our study did not demonstrate significant predictive value. Maximum SUV and SUVpeak showed statistical significance only in the univariate analysis, but their significance was lost after the inclusion of other semi-quantitative and quantitative ^{18}F-FDG PET/CT parameters. Data from literature are contradictory. Gallicchio et al. (2014) reported that higher SUVmax values were associated with a better prognosis of the disease [21]. On the other hand, some studies show that higher SUVmax values are associated with worse prognosis [15, 16]. These conflicting results can be explained by several factors reported in the literature. High SUVmax values are generally associated with more aggressive types of lymphoma linked to faster progression and shorter survival [10]. However, some studies suggest that higher SUVmax values, indicating greater glycolytic activity, are associated with a better response to chemotherapy and longer survival [21].

In our study, MTV and TLG did not prove to be significant factors in the prediction of response to therapy, which is consistent with the results of other studies [12, 16, 21]. Possible explanation could be that the MTV and TLG parameters could underestimate the actual tumor burden due to necroses often present in large tumor masses, with absent accumulation of ^{18}F-FDG [12].

The main limitations of this study are related to the relatively small sample size and the fact that all patients from this study belonged to one center, so it is necessary to analyze, monitor and compare the results from more different institutions. A longer follow-up period is necessary to assess the predictive significance of all investigated parameters for the long-term prognosis of the disease. This study lays the foundation for further research to determine whether patients with DS $\leq$3, after 18 months, have successfully avoided disease progression, and for how long.

In conclusion, the results of this study indicate that the early metabolic response to therapy, assessed on the basis of interim ^{18}F-FDG PET/CT is a significant independent predictive factor of disease outcome in patients with DLBCL. The use of ^{18}F-FDG PET/CT during therapy helps in the early identification of patients at increased risk for disease progression, allowing for timely adjustments to the therapeutic approach.

The authors declare that they have no conflicts of interest.

Acknowledgement

The study was supported by Grant No 451-03-137/2025-03/ 200110 Ministry of Science, Technological Development and Innovation.

Bibliography

1. Jiang P, Yu F, Zhou X et al. Dissecting causal links between gut microbiota, inflammatory cytokines, and DLBCL: a Mendelian randomization study. *Blood Adv* 2024; 8(9): 2268-78.
2. Al Armashi AR, Al Zubaidi A, Mahmood O et al. Trends in Diffuse Large B-Cell Lymphoma Mortality in the United States: A Comprehensive Review from 2000 to 2020. *Blood* 2023; 142((Suppl. S1)): 1765.
3. Chua B.J.G, Low C.E, Yau C et al. Recent updates on central nervous system prophylaxis in patients with high-risk diffuse large B-cell lymphoma. *Exp Hematol Oncol* 2024; 13: 1.
4. Feng K, Zhao S, Shang Q et al. The prognostic value of IPI in patients with primary breast lymphoma, a multicenter retrospective study. *Cancer Cell Int* 2022; 22(1): 357.
5. Voltin CA, Mettler J, Grosse J et al. ^{18}F-FDG-PET Imaging for Hodgkin and Diffuse Large B-Cell Lymphoma-An Updated Overview. *Cancers (Basel)* 2020; 12(3): 601.
6. Gómez León N, Delgado-Bolton RC, Del Campo Del Val L et al. Multicenter Comparison of Contrast-Enhanced ^{18}F-FDG PET/CT and 64-Slice Multi-Detector-Row CT for Initial Staging and Response Evaluation at the End of Treatment in Patients With Lymphoma. *Clin Nucl Med* 2017; 42(8): 595-602.
7. Todorovic Tirnanic M, Artiko V, Methods of nuclear medicine in hematology. In: Šobić Šaranović D, Artiko V. Eds. *Nuclear medicine*. Belgrade: Faculty of Medicine, University of Belgrade; 2020. p203-237.
8. Zanoni L, Bezzi D, Nanni C et al. PET/CT in Non-Hodgkin Lymphoma: An Update. *Semin Nucl Med* 2023; 53(3): 320-51.
9. Meignan M, Gallamini A, Haioun C. Report on the First International Workshop on Interim-PET-Scan in Lymphoma. *Leuk Lymphoma* 2009; 50: 1257-60.
10. Cheson BD, Fisher RI, Barrington SF et al. Recommendations for initial evaluation, staging, and response assessment of Hodgkin and non-Hodgkin lymphoma: The Lugano classification. *J Clin Oncol* 2014; 32: 3059-68.
11. Eertink JJ, Zwezerijnen GJC, Heymans MW et al. Baseline PET radiomics outperforms the IPI risk score for prediction of outcome in diffuse large B-cell lymphoma. *Blood* 2023; 141(25): 3055-64.
12. Zhou Z, Sehn LH, Rademaker AW et al. An enhanced international prognostic index (NCCN-IPI) for patients with diffuse large B-cell lymphoma treated in the rituximab era. *Blood* 2014; 123: 837-42.
13. Vaidya R, Witzig TE. Prognostic factors for diffuse large B-cell lymphoma in the R(X)CHOP era. *Ann Oncol* 2014; 25: 2124-33.
14. Sehn LH, Berry B, Chhanabhai M et al. The revised international prognostic index (R-IPI) is a better predictor of outcome than the standard IPI for patients with diffuse large B-cell lymphoma treated with R-CHOP. *Blood* 2007; 109: 1857-61.
15. Kwon SH, Kang DR, Kim J et al. Prognostic value of negative interim 2-[^{18}F]-fluoro-2-deoxy-d-glucose PET/CT in diffuse large B-cell lymphoma. *Clin Radiol* 2016; 71(3): 280-6.
16. Park S, Moon SH, Park LC et al. The impact of baseline and interim PET/CT parameters on clinical outcome in patients with diffuse large B cell lymphoma. *Am J Hematol* 2012; 87: 937-40.
17. Burggraaff CN, de Jong A, Hoekstra OS, et al. Predictive value of interim positron emission tomography in diffuse large B-cell lymphoma: a systematic review and meta-analysis. *Eur J Nucl Med Mol Imaging* 2019; 46(1): 65-79.
18. Jin J, Liu Y, Zhang Q et al. Interim PET/CT result is the sole prognostic factor of survival in patients with advanced-stage diffuse large B-cell lymphoma: a subset analysis of a prospective trial. *J Radioanal Nucl Chem* 2021; 327: 353-8.
19. Allioux F, Gandhi D, Vilque JP et al. End-of-treatment ^{18}F-FDG PET/CT in diffuse large B cell lymphoma patients: ΔSUV outperforms Deauville score. *Leuk Lymphoma* 2021; 62(12): 2890-8.
20. Zhu L, Meng Y, Guo L et al. Predictive value of baseline ^{18}F-FDG PET/CT and interim treatment response for the prognosis of patients with diffuse large B-cell lymphoma receiving R-CHOP chemotherapy. *Oncol Lett* 2021; 21(2): 132.
21. Gallicchio R, Mansueto G, Simeon V et al. ^{18}F-FDG PET/CT quantization parameters as predictors of outcome in patients with diffuse large B-cell lymphoma. *Eur J Haematol* 2014; 92(5): 382-9.

^{68}Ga-pentixafor for PET imaging of chemokine receptor 4 expression in lymphoproliferative diseases and solid tumors

Tingwei Meng Msc,
Qingqing Pan MD,
Yaping Luo MD

Department of Nuclear Medicine, State Key Laboratory of Common Mechanism Research for Major Diseases, Chinese Academy of Medical Sciences and Peking Union Medical College Hospital, Beijing, China.

Keywords: CXCR4 - ^{68}Ga-pentixafor - Lymphoma - Multiple myeloma - Pancreatic cancer

Corresponding author:
Qingqing Pan MD,
Department of Nuclear Medicine,
State Key Laboratory of Common Mechanism Research for Major Diseases, Chinese Academy of Medical Sciences and Peking Union Medical College Hospital.
Address: No.1 Shuaifuyuan Wangfujing, Dongcheng District, Beijing, 100730, P. R. China
Tel: 86-10-69154720
pqqelvay@126.com

Yaping Luo MD,
Department of Nuclear Medicine,
State Key Laboratory of Common Mechanism Research for Major Diseases, Chinese Academy of Medical Sciences and Peking Union Medical College Hospital.
Address: No.1 Shuaifuyuan Wangfujing, Dongcheng District, Beijing, 100730, P. R. China
Tel: 86-10-69154716
luoyaping@live.com

Received:
13 March 2025
Accepted revised:
26 June 2025

Abstract

Objective: Gallium-68 (^{68}Ga)-pentixafor, a novel positron emission tomography (PET) tracer with high affinity for C-X-C motif chemokine receptor 4 (CXCR4), has recently been introduced in order to assess the CXCR4 expression status in vivo. This study is to investigate the role of ^{68}Ga-pentixafor in detecting various tumors with mice models and to provide references to clinical studies. **Materials and Methods:** Gallium-68-pentixafor and fluorine-18-fluorodeoxyglucose (^{18}F-FDG) PET was performed in opm-2 (lymphoma), daudi (myeloma) and panc1 (pancreatic cancer)-bearing mice. Tumor and background tissue uptake between ^{68}Ga-pentixafor and ^{18}F-FDG PET were compared. Gallium-68-pentixafor PET/computed tomography (CT) was performed in four patients with lymphoma and three patients with multiple myeloma, and ^{18}F-FDG PET/CT was performed as a reference. **Results:** The uptake of ^{68}Ga-pentixafor in background tissues including muscle, liver and kidneys were all lower than those of ^{18}F-FDG. The uptake of ^{68}Ga-pentixafor in the tumors of lymphoma and myeloma-bearing xenografts was comparable or higher than those of ^{18}F-FDG. However, the tumors of panc-1 xenografts had much lower uptake of ^{68}Ga-pentixafor than those in lymphoma and myeloma-bearing mice, and it was also significantly lower than those of ^{18}F-FDG. The high uptake of ^{68}Ga-pentixafor in vivo was confirmed by the high expression of CXCR4 in tumors with immunochemical analysis. Gallium-68-pentixafor PET/CT in patients with marginal zone lymphoma (MZL) and myeloma showed more intense uptake and more extensive involvement than ^{18}F-FDG PET/CT did. Gallium-68-pentixafor and ^{18}F-FDG PET/CT showed comparable uptake in the patient with follicular lymphoma. **Conclusions:** Gallium-68-pentixafor is a promising agent for the evaluation of lymphoproliferative diseases.

Hell J Nucl Med 2025; 28(2): 124-130 *Epub ahead of print: 4 August 2025* *Published online: 30 August 2025*

Introduction

Chemokine receptors form a large family of G-protein coupled receptors that mediate chemotaxis of cells towards a gradient of chemokines. C-X-C motif chemokine receptor 4 (CXCR4) is a transmembrane G-protein-coupled receptor physiologically expressed on T-lymphocytes, B-lymphocytes, monocytes, macrophages, neutrophils and eosinophils as well as hematopoietic stem and progenitor cells in the bone marrow [1]. In pathological conditions, CXCR4 overexpression has been reported in more than 30 different types of cancer crucially involving in tumor dissemination [2], and CXCR4 overexpression has been identified as an adverse prognostic factor of lymphoma, leukemia and solid tumors [3-6].

Gallium-68 (^{68}Ga)-pentixafor, a novel positron emission tomography (PET) tracer with high affinity for CXCR4, has recently been introduced in order to assess the CXCR4 expression status in vivo [7]. In preclinical studies, ^{68}Ga-pentixafor PET/computed tomography (CT) provided images with excellent specificity and contrast in lymphoma and myeloma xenografts [8, 9]. However, the comparison of ^{68}Ga-pentixafor and fluorine-18-fluorodeoxyglucose (^{18}F-FDG) in the distribution of this tracer need further illustrated. Additionally, whether ^{68}Ga-pentixafor could be used to map CXCR4 expression in solid tumors xenografts has not been fully investigated. Thus, we conducted this preclinical study in order to compare the role of ^{68}Ga-pentixafor with ^{18}F-FDG PET in detecting various tumors with mice models and to provide references to further clinical studies.

Materials and Methods

Preparation of ^{68}Ga-pentixafor

The synthesis of ^{68}Ga-pentixafor was performed as described in published articles [10]. In short, 92mL of sodium acetate (1.25M) was added to 1mL of gallium-68 trichloride ($^{68}GaCl_3$) eluent ($^{68}Ga^{3+}$ in 1.0M HCl) obtained from a germanium-68 (^{68}Ge)/^{68}Ga generator (ITG) to adjust the pH to 3.5-4.0. After the addition of a 20μL aliquot (1mg/mL) of DOTA-CPCR4-2 (purchased from CSBio Co.), the mixture was heated to 105°C for 15min. The reaction solution was diluted to 5mL and passed through a preconditioned Sep-Pak C18 Plus Light cartridge (Waters), and the cartridge was eluted with 0.5mL of 75% ethanol to obtain the final product. The radio-chemical purity of the product was analyzed by thin-layer chromatography. The radiochemical purity was always >99%, and the molar activities of the ^{68}Ga-labeled peptides were in the range of 41.3±17.1GBq/μmol. Fluorine-18-FDG was synthesized in-house with an 11MeV cyclotron (CTIRDS 111).

Cell culture and animal model

Opm-2 (lymphoma) and daudi (myeloma) cell lines were grown in Roswell Park Memorial Institute 1640 (RPMI-1640) with 10% fetal bovine serum (FBS), 2mM glutamine, and 100 units/mL penicillin/streptomycin. Panc1(pancreatic cancer) cell lines were incubated in Dulbecco's Modified Eagle Medium (DMEM) medium supplemented with 10% FBS, 2mM glutamine, and 100 units/mL penicillin/streptomycin. All cell lines were maintained in 5% CO_2 at 37°C.

Female nude mice (6-8 weeks, Beijing Vital River Laboratory Animal Technology Co., Ltd.) were subcutaneously injected in the right shoulder with $\sim 5\times10^6$ daudi cells (or opm-2 or panc1) suspended in 100μL of a 1/1 (v/v) mixture of serum free culture medium and Matrigel (BD Biosciences, Heidelberg, Germany). Once tumors became palpable {100 mm^3 [volume=0.5×long diameter×(short diameter)2]}, approximately 15-21 days post-injection, the animals were employed in the experiments.

In vivo PET study

All mice received ^{68}Ga-pentixafor and ^{18}F-FDG micro PET static scan in two consecutive days. Animals were fasted for 2 hours before scanning. An average of 4.4-15.2MBq ^{68}Ga-pentixafor was injected intravenously into the tail vein of isoflurane anesthetized female daudi (n=4), opm-2 (n=4), and panc1-bearing (n=4) Severe Combined Immunodeficiency mice (SCID mice). Static PET imaging was acquired at 30, 60, 90, 120min p.i. (Inveon micro-PET scanner, Siemens, Germany). Fluorine-18-FDG PET scan was performed at the same time interval after intravenously injection with 8.1-11.5MBq of ^{18}F-FDG. All images were analyzed with the Inveon Research Workspace software, and tumor-to-background ratios were measured.

To fully investigated the advantages of ^{68}Ga-pentixafor comparing to ^{18}F-FDG, PET/CT study in humans was further carried out. Seven patients with lymphoma and multiple myeloma (MM) were included. The study was approved by the institutional review board in Peking Union Medical College Hospital, and written informed consent was obtained from all the patients before PET/CT scan. All PET scans were performed on dedicated PET/CT scanners (Biograph 64 Truepoint TrueV, Siemens, Germany; Polestar m660, SinoUnion, China). For ^{18}F-FDG PET/CT, the patients fasted for at least 6h, and the blood glucose levels were monitored (5.3-7.5mmol/L) before an injection of ^{18}F-FDG (5.55MBq/kg). The PET/CT images (2min/bed) were acquired with an uptake time of 75.0±13.0min (range, 60-83min). For ^{68}Ga-pentixafor PET/CT, imaging was performed (2-3min/bed) with an uptake time of 51.8±13.5 (range, 30-70min) after an injection of 92.5±44.4MBq (range, 55.5-170.2MBq) of ^{68}Ga-pentixafor. The emission scan was obtained from the tip of the skull to the midthigh. All patients underwent unenhanced low-dose CT (120kV; 30-50mAs) for attenuation correction and anatomic reference. For image analysis, all PET/CT scans were read by 2 experienced nuclear medicine physicians (YL and QP). Lesions were visually determined as focally increased tracer retention as compared to surrounding normal tissue. Bone marrow involvement in PET/CT was interpreted as being positive if there was presence of focal lesions with positive PET results, or diffuse bone marrow patterns with uptake higher than liver. The involvement of lymphoma/myeloma, and their highest maximum standardized uptake value (SUVmax) were recorded.

Immunohistochemical staining

The mice were sacrificed after PET imaging and tumor tissues were obtained. For immunohistochemistry, anti-CXCR4 rabbit polyclonal antibody (Abcam) was used. After deparaffinization and rehydration, the slides were placed in a pressure cooker in 0.01M citrate buffer (pH 6.0) and were heated for 7 min. Incubation with the different antibodies was carried out overnight at 4°C. Detection was performed with DAKO envision system according to the manufacturer's protocol.

Statistical analysis

Statistical analyses were done with Medcalc (version 19.6.4) and SPSS Statistics software (version 22.0, IBM SPSS Inc.). Quantitative values were expressed as mean±standard deviation. Comparisons of related metric measurements were performed using Wilcoxon signed-rank test, or Student's t-test was used to compare quantitative data between two paired samples. A P-value <0.05 was considered statistically significant.

Results

Animal studies

Daudi xenografts

The uptake of ^{68}Ga-pentixafor in the tumor of daudi xenografts was increasing over time and clearly delineated 120 mins p.i., which was similar to that of ^{18}F-FDG (uptake of ^{68}Ga-pentixafor vs ^{18}F-FDG: 2.50±4.47% ID/g, vs 2.82±1.82% ID/g, P=0.7859). The uptake of ^{68}Ga-pentixafor in background tissues including muscle, liver and kidneys were all lower than that of ^{18}F-FDG, especially in muscle 120mins p.i. (^{68}Ga-pentixafor vs ^{18}F-FDG: 0.28±0.10% ID/g, vs 2.36±1.37% ID/g, P= 0.0501). The tumor/muscle, tumor/liver and tumor/ kidneys ratios of ^{68}Ga-pentixafor were all higher than those that of ^{18}F-FDG (Figure 1).

Opm-2 xenografts

The uptake of ^{68}Ga-pentixafor in the tumor of opm-2 xenografts was also increasing over time and clearly delineated 120mins p.i. The tumor uptake showed higher uptake than those of ^{18}F-FDG in the only survival xenograft (the uptake of ^{68}Ga-pentixafor vs ^{18}F-FDG: 5.33±3.09% ID/g vs 4.9% ID/g). The uptake of ^{68}Ga-pentixafor in background tissues including muscle, liver and kidneys were all lower than those of ^{18}F-FDG, leading to higher tumor/muscle, tumor/liver and tumor/kidneys ratios of ^{68}Ga-pentixafor than those of ^{18}F-FDG. The highest tumor/muscle ratio of ^{68}Ga-pentixafor was delineated at 90mins with the activity uptake of 11.80± 3.23% ID/g comparing to those of ^{18}F-FDG with the activity uptake of 0.69% ID/g. The highest tumor/liver and tumor/ kidneys ratios of ^{68}Ga-pentixafor were delineated at 120 mins with the activity uptake of 4.80±0.53% ID/g and 2.86± 1.22% ID/g, respectively (Figure 2).

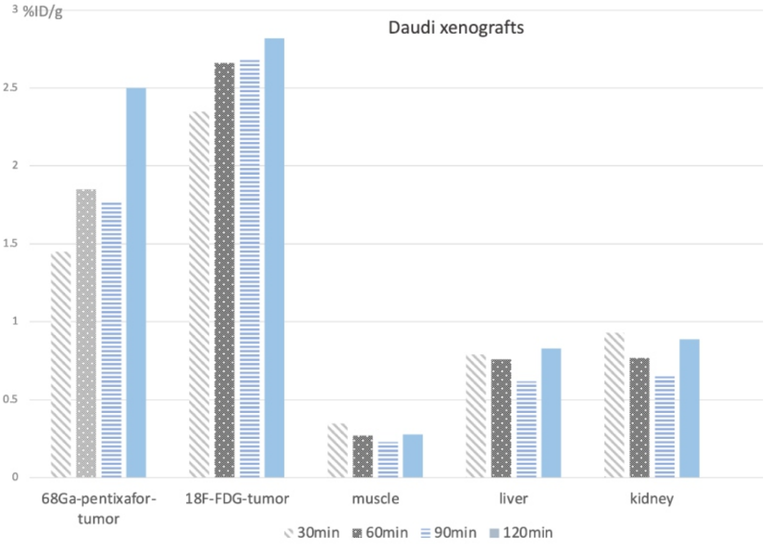

Figure 1. The biodistribution of ^{68}Ga-pentixafor and ^{18}F-FDG at different time points after injection in daudi-bearing mice. The uptake of ^{68}Ga-pentixafor in the tumor of daudi xenografts was increasing over time and clearly delineated 120mins p.i.

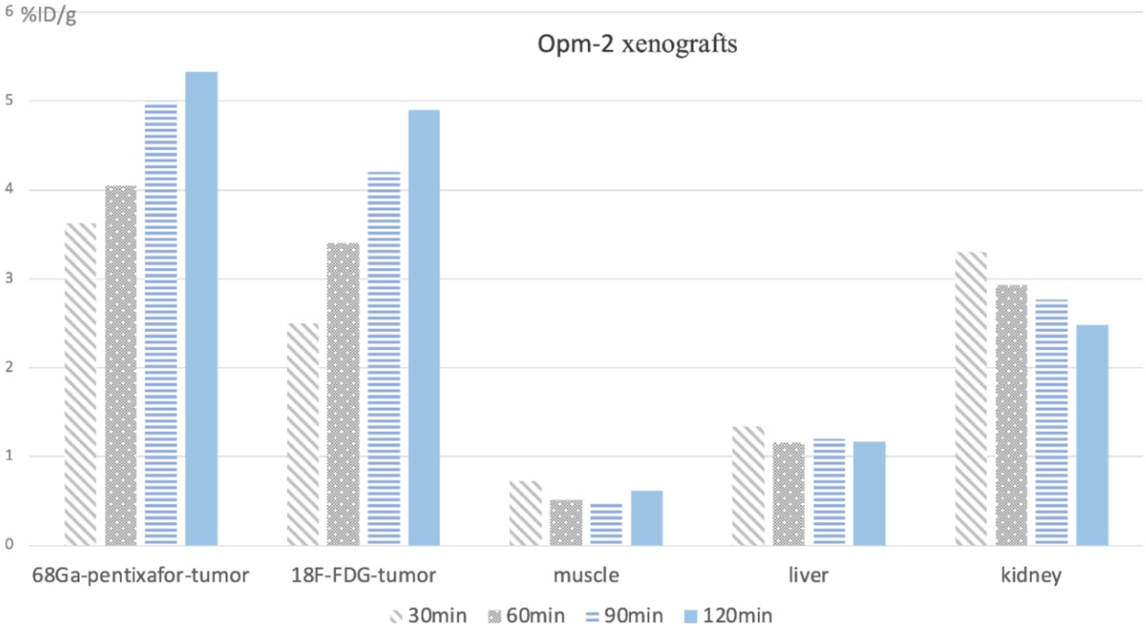

Figure 2. The biodistribution of ^{68}Ga-pentixafor and ^{18}F-FDG after injection at different time points in opm2-bearing mice. The uptake of ^{68}Ga-pentixafor in the tumor of opm-2 xenografts was increasing over time and clearly delineated 120mins p.i..

Panc-1 xenografts

The panc-1 xenografts had much lower uptake of ^{68}Ga-pentixafor than those in daudi and opm-2-bearing mice, and it was also significantly lower than the uptake of ^{18}F-FDG (^{68}Ga-pentixafor vs ^{18}F-FDG: 30mins p.i., 0.46±0.12% ID/g vs 1.18±0.15% ID/g, P=0.0032; 60mins p.i., 0.37±0.14% ID/g vs 1.30±0.18% ID/g, P=0.0008; 90mins p.i., 0.36±0.06% ID/g vs 1.28±0.13% ID/g, P=0.0009; 120mins p.i., 0.41±0.14% ID/g vs 1.35±0.10% ID/g, P=0.0039) (Figure 3).

Immunohistochemical analysis of representative daudi and opm-2 xenograft samples showed intense CXCR4 expression, however it was relatively low in the sample of panc-1-bearing mice. Representative images were shown in Figure 4.

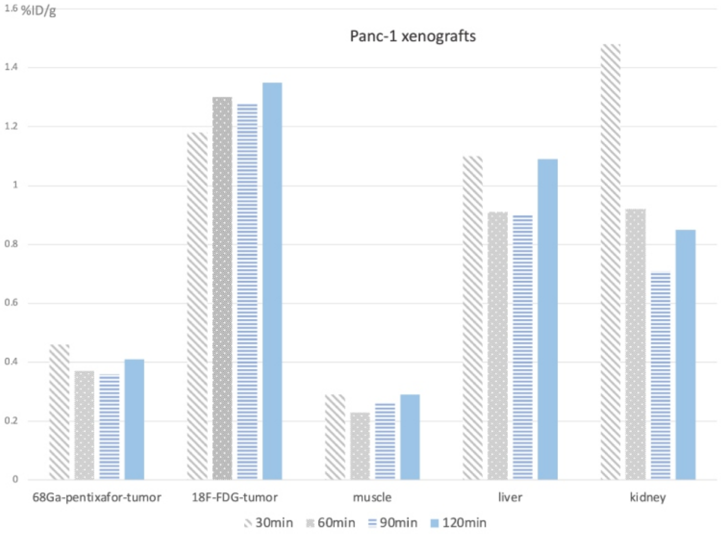

Figure 3. The biodistribution of ^{68}Ga-pentixafor and ^{18}F-FDG after injection at different time points in panc-1-bearing mice. The uptake of ^{68}Ga-pentixafor in panc-1 xenografts was significantly lower than that of ^{18}F-FDG.

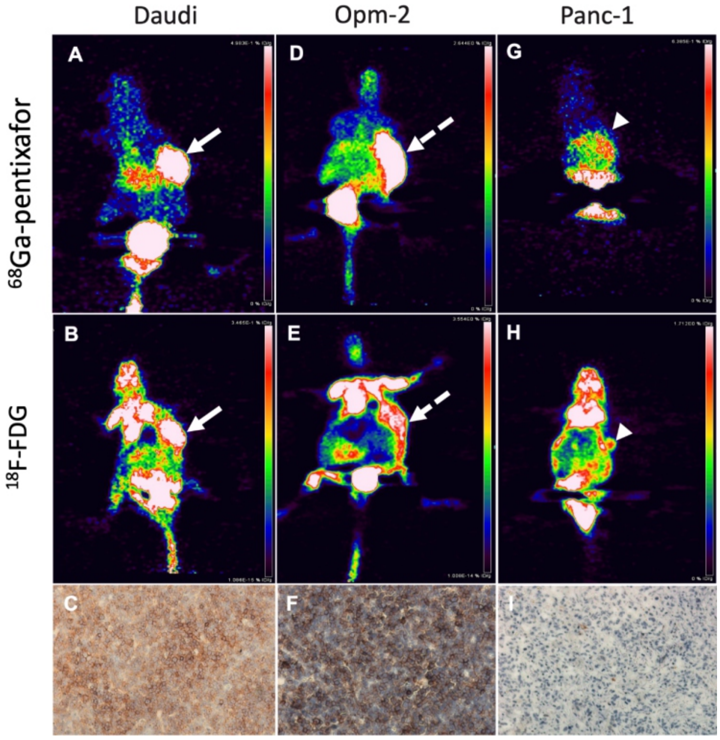

Figure 4. Representative images of three types of xenografts. (A-C) Daudi-bearing mice. Gallium-68-pentixafor (A) and ^{18}F-FDG (B) PET showed intense tracer uptake in tumor on the right shoulder 120min p.i. (white arrows), which was consistent with the high expression of CXCR4 on immunohistochemical analysis (scale bars: 100µm) (C). (D-F) Opm2-bearing mice. The tumor on the right shoulder showed intense uptake of ^{68}Ga-pentixafor PET 120min p.i. (D) and ^{18}F-FDG avidity (E) (white dotted arrows). The immunohistochemical analysis also demonstrated strong CXCR4 expression (scale bars: 100µm) (F). In panc-1-bearing mice, the tumor showed increased uptake of ^{18}F-FDG 120min p.i.(H) but nearly no uptake of ^{68}Ga-pentixafor (G) (white arrow heads). Consistently, CXCR4 expression was low in the tumor sample with immunohistochemical analysis (scale bars: 100 µm) (I)

PET/CT study in humans

Gallium-68-pentixafor PET/CT was further performed in seven patients with histologically proven lymphoma or multiple myeloma. Fluorine-18-FDG PET/CT was performed as comparison (Table 1).

In the three patients with marginal zone lymphoma, ^{68}Ga-pentixafor PET/CT showed superiority to ^{18}F-FDG with more intense uptake and more extensive involvement in bone marrow, lymph nodes, as well as retroperitoneum, kidney, psoas major and dura mater. The SUVmax of ^{68}Ga-pentixafor PET/CT was higher than those of ^{18}F-FDG PET/CT (13.4±4.7 vs. 5.3±5.0, P=0.011). In one patient with follicular lymphoma, ^{68}Ga-pentixafor and ^{18}F-FDG PET/CT both detected lymph nodes involving neck and left inguinal area with similar intensity of tracer uptake (the SUV max, 9.9 vs. 16.3).

In the three patients with multiple myeloma, ^{68}Ga-pentixafor PET/CT were all positive, while ^{18}F-FDG PET/CT were visually negative in two patients and positive in one patient. Gallium-68-pentixafor PET/CT showed more intense and extensive bone marrow involvement than ^{18}F-FDG did. In two patients, ^{68}Ga-pentixafor PET/CT additionally detected focal bone lesions and paramedullary diseases which were not seen in ^{18}F-FDG PET/CT. The SUVmax of ^{68}Ga-pentixafor PET/CT was significantly higher than those of ^{18}F-FDG PET/CT (17.8±2.4 vs. 3.4±1.6, P=0.001). Comparison of maximum intensity projections of PET images were shown in Figure 5.

Discussion

In our study, we evaluated ^{68}Ga-pentixafor as a probe for CXCR4 imaging in xenograft models of lymphoma, myeloma and pancreatic cancer cell lines. The results showed significantly high uptake of ^{68}Ga-pentixafor in lymphoma and myeloma. However, the uptake of ^{68}Ga-pentixafor in pancreatic cancer bearing mice was significantly low.

With its high CXCR4 affinity, ^{68}Ga-pentixafor first demonstrated excellent in vivo pharmacokinetics and highly specific accumulation in CXCR4-positive cell lines of small cell lung cancer [11]. In addition, Wester et al. (2015) found that CXCR4 expression correlated with lymphoma cellular uptake, and ^{68}Ga-pentixafor PET/CT studies showed excellent imaging properties in lymphoma-bearing mice [4]. In patient studies, ^{68}Ga-pentixafor PET/CT showed excellent tumor uptake in diffuse large B-cell lymphoma and aggressive T-cell lymphoma [4]. Our study showed consistent results with previous studies of high uptake of ^{68}Ga-pentixafor in lymphoma tumors [12-16]. Furthermore, ^{68}Ga-pentixafor PET/CT showed superior imaging characteristics to ^{18}F-FDG in three patients with MZL, with more intense and extensive lesions detected. Staging of marginal zone lymphoma is challenging with ^{18}F-FDG PET/CT because marginal zone lymphoma does not usually present with increased glycolysis and may have heterogeneous metabolic behavior [17, 18]. Therefore, it's suggested that ^{68}Ga-pentixafor PET/CT may have the potential to be used in the evaluation of lymphomas, particularly in those types of lymphoma with low ^{18}F-FDG avidity.

Fluorine-18-FDG PET/CT has an impact on the work up of MM. However, the false-negative ^{18}F-FDG uptake [19-22] due

Table 1. *Patients' clinical characteristics and PET/CT results.*

Age/sex	Tumor type	Involvement	SUVmax of PET/CT	
			^{68}Ga-pentixafor	^{18}F-FDG
59/M	MZL (Ann Arbor IV)	Bone marrow, lymph node	6.7	2.7
51/M	MZL (Ann Arbor IV)	Bone marrow, lymph node	11.0	2.6
65/ F	MZL (Ann Arbor IV)	Retroperitoneum, kidney, psoas major, dura mater	12.5	5.2
59/M	FL (Grade 1-2)	Lymph node	9.9	16.3
74/M	MM (LC-λ, ISS III)	Bone marrow	15.5	2.3
49/ F	MM (IgA-κ, ISS III)	Bone marrow	20.3	5.2
61/M	MM (LC-κ, ISS III)	Bone marrow	17.7	2.7

MZL=marginal zone lymphoma, FL=follicular lymphoma, MM=multiple myeloma, LC=light chain, ISS=International Staging System.

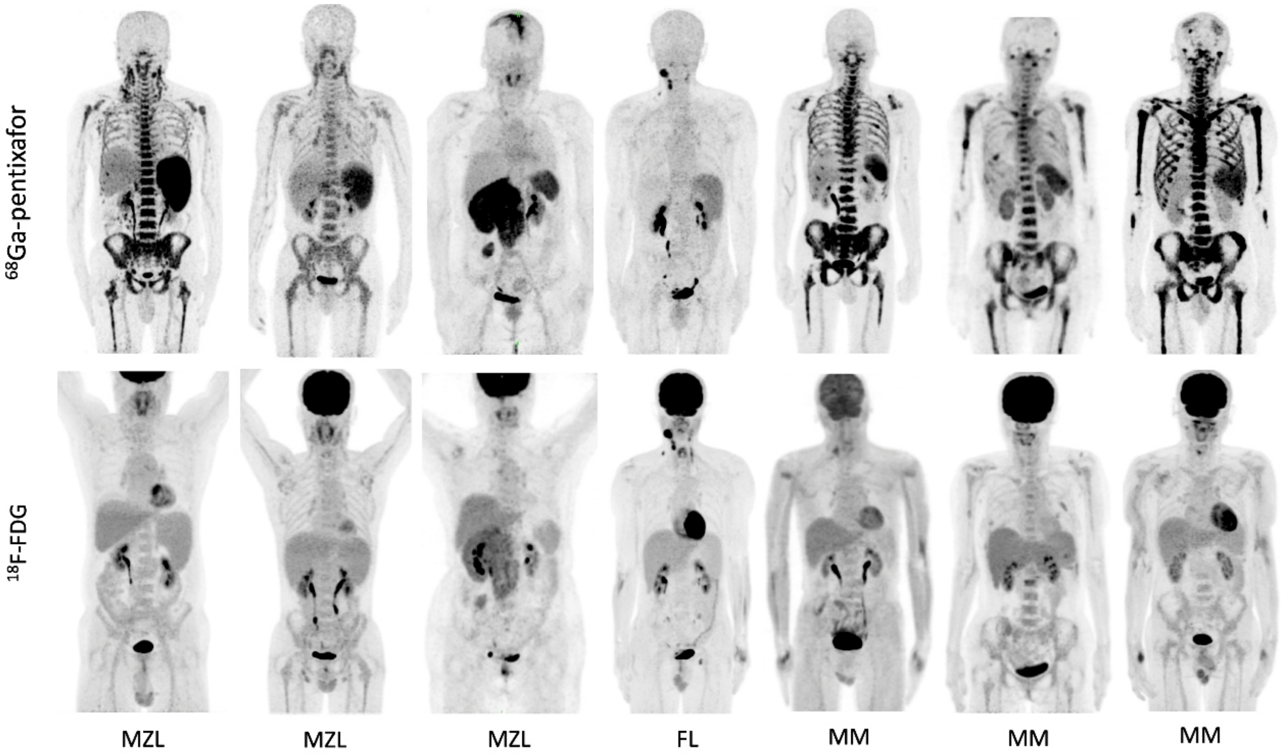

Figure 5. Individual comparison of lymphoproliferative diseases shown on ^{68}Ga-pentixafor and ^{18}F-FDG PET/CT. Gallium-68-pentixafor PET showed obviously higher intensity than ^{18}F-FDG uptake in marginal zone lymphoma (MZL) and multiple myeloma (MM) with more intense uptake in involved bone marrow, lymph nodes, as well as extranodal lesions. In follicular lymphoma (FL), ^{68}Ga-pentixafor and ^{18}F-FDG PET detected involvement of cervical and inguinal lymph nodes with comparable uptake of both tracer.

to the loss of hexokinase-2 expression in MM [23] hampers the assessment of the extent of disease and staging of MM with ^{18}F-FDG PET/CT. According to our study, ^{68}Ga-pentixafor demonstrated high accumulation and tumor to background ratio in MM tumors in vivo, which was consistent with the previous study [24-27]. The high expression of CXCR4 on tumor cell surface revealed by immunohistochemical analysis was considered to be correlated with the high uptake of ^{68}Ga-pentixafor in our small animal PET. This correlation was also confirmed by the previous study using flow cytometric quantification of cell surface CXCR4 expression on MM tumors [21]. We further applied ^{68}Ga-pentixafor PET/CT in patients with MM. In three patients with advanced MM, ^{68}Ga-pentixafor PET/CT scans revealed extensive MM involvement, whereas all ^{18}F-FDG PET/CT scans were rated visually negative. These encouraging results suggested ^{68}Ga-pentixafor PET/CT may overcome the shortcomings of ^{18}F-FDG in the evaluation of MM patients.

In contrast to the high tracer avidity in lymphoma and MM, ^{68}Ga-pentixafor showed very low uptake in panc1-bearing mice, and it also showed significantly lower uptake than ^{18}F-FDG in our study. The immunohistochemical analysis confirmed the low expression of CXCR4 on panc1 cells. As to solid tumors, previous literatures showed very high tracer uptake (SUVmax >12) was found in adrenocortical carcinoma, adrenocortical adenoma, and small cell lung cancer [28], however 37.5% of the patients with pancreatic cancer were negative with ^{68}Ga-pentixafor [29]. This heterogeneous uptake of ^{68}Ga-pentixafor in different types of solid tumors should be further investigated especially when using ^{68}Ga-pentixafor PET/CT as an approach for patient selection for CXCR4-targeted therapies.

In conclusion, ^{68}Ga-pentixafor PET showed high uptake in lymphoma and MM, and may be a promising method for assessing lymphoproliferative diseases. However, pancreatic cancer may not be indicated for ^{68}Ga-pentixafor PET.

The authors declare that they have no conflicts of interest.

Ethics approval and consent to participate

We performed this study in compliance with the 1964 Helsinki Declaration and its later amendments and federal laws in China. The study was approved by the institutional review board of PUMCH (IRB protocol # ZS-1810) and registered at Clinicaltrial.gov (NCT 04514614). All patients signed written informed consent for participation in this study.

Funding

This study has received funding by National High Level Hospital Clinical Research Funding (2022-PUMCH-A-127, 2022-PUMCH-B-070, 2022-PUMCH-B-071) and Peking Union Medical College Hospital Talent Cultivation Program (Categoty C, UBJ10707).

Bibliography

1. Teicher BA, Fricker SP. CXCL12 (SDF-1)/CXCR4 pathway in cancer. *Clin Cancer Res* 2010; 16: 2927-31.
2. Domanska UM, Kruizinga RC, Nagengast WB et al. A review on CXCR4/CXCL12 axis in oncology: no place to hide. *Eur J Cancer* 2013; 49: 219-30.
3. Scotton CJ, Wilson JL, Scott K et al. Multiple actions of the chemokine CXCL12 on epithelial tumor cells in human ovarian cancer. *Cancer Res* 2002; 62: 5930-8.
4. Lapa C, Lückerath K, Kleinlein I et al. ^{68}Ga-Pentixafor-PET/CT for Imaging of Chemokine Receptor 4 Expression in Glioblastoma. *Theranostics* 2016; 6: 428-34.
5. Müller A, Homey B, Soto H et al. Involvement of chemokine receptors in breast cancer metastasis. *Nature* 2001; 410: 50-6.
6. Burger JA, Peled A. CXCR4 antagonists: targeting the microenvironment in leukemia and other cancers. *Leukemia* 2009; 23: 43-52.
7. Herrmann K, Lapa C, Wester HJ et al. Biodistribution and radiation dosimetry for the chemokine receptor CXCR4-targeting probe ^{68}Ga-pentixafor. *J Nucl Med* 2015; 56: 410-6.
8. Philipp-Abbrederis K, Herrmann K, Knop S et al. In vivo molecular imaging of chemokine receptor CXCR4 expression in patients with advanced multiple myeloma. *EMBO Mol Med* 2015; 7: 477-87.
9. Wester HJ, Keller U, Schottelius M et al. Disclosing the CXCR4 expression in lymphoproliferative diseases by targeted molecular imaging. *Theranostics* 2015; 5: 618-30.
10. Pan Q, Luo Y, Zhang Y et al. Preliminary evidence of imaging of chemokine receptor-4 targeted PET/CT with ^{68}Ga pentixafor in non-Hodgkin lymphoma: comparison to ^{18}F-FDG. *EJNMMI Res* 2020; 10: 89.
11. Gourni E, Demmer O, Schottelius M et al. PET of CXCR4 expression by a ^{68}Ga-labeled highly specific targeted contrast agent. *J Nucl Med* 2011; 52: 1803-10.
12. Pan Q, Luo Y, Cao X et al. Posttreated POEMS Syndrome With Concurrent Follicular Lymphoma Revealed by ^{18}F-FDG and ^{68}Ga-Pentixafor PET/CT. *Clin Nucl Med* 2020; 45: 220-2.
13. Luo Y, Cao X, Pan Q et al. ^{68}Ga-Pentixafor PET/CT for Imaging of Chemokine Receptor 4 Expression in Waldenström Macroglobulinemia/Lymphoplasmacytic Lymphoma: Comparison to ^{18}F-FDG PET/CT. *J Nucl Med* 2019; 60: 1724-9.
14. Pan Q, Cao X, Luo Y et al. Chemokine Receptor 4-Targeted ^{68}Ga-Pentixafor PET/CT in Response Assessment of Waldenström Macroglobulinemia/Lymphoplasmacytic Lymphoma: Comparison to ^{18}F-FDG PET/CT. *Clin Nucl Med* 2021; 46: 732-7.
15. Pan Q, Cao X, Luo Y et al. Semi-quantitative measurements of chemokine receptor 4-targeted ^{68}Ga-pentixafor PET/CT in response assessment of Waldenström macroglobulinemia/lymphoplasmacytic lymphoma. *EJNMMI Res* 2021; 11: 110.
16. Pan Q, Luo Y, Zhang Y et al. Preliminary evidence of imaging of chemokine receptor-4-targeted PET/CT with ^{68}Ga-pentixafor in non-Hodgkin lymphoma: comparison to ^{18}F-FDG. *EJNMMI Res* 2020; 10: 89.
17. Albano D, Bosio G, Giubbini R, Bertagna F. ^{18}F-FDG PET/CT and extragastric MALT lymphoma: role of Ki-67 score and plasmacytic differentiation. *Leuk Lymphoma* 2017; 58: 2328-34.
18. Albano D, Durmo R, Treglia G et al. ^{18}F-FDG PET/CT or PET Role in MALT Lymphoma: An Open Issue not Yet Solved-A Critical Review. *Clin Lymphoma Myeloma Leuk* 2020; 20: 137-46.
19. Zamagni E, Nanni C, Patriarca F et al. A prospective comparison of ^{18}F-fluorodeoxyglucose positron emission tomography-computed tomography, magnetic resonance imaging and whole-body planar radiographs in the assessment of bone disease in newly diagnosed multiple myeloma. *Haematologica* 2007; 92: 50-5.
20. Spinnato P, Bazzocchi A, Brioli A et al. Contrast enhanced MRI and ^{18}F-FDG PET-CT in the assessment of multiple myeloma: a comparison of results in different phases of the disease. *Eur J Radiol* 2012; 81: 4013-8.
21. Philipp-Abbrederis K, Herrmann K, Knop S et al. In vivo molecular imaging of chemokine receptor CXCR4 expression in patients with advanced multiple myeloma. *EMBO Mol Med* 2015; 7: 477-87.
22. Nanni C, Zamagni E, Farsad M et al. Role of ^{18}F-FDG PET/CT in the assessment of bone involvement in newly diagnosed multiple myeloma: preliminary results. *Eur J Nucl Med Mol Imaging* 2006; 33: 525-31.
23. Rasche L, Angtuaco E, McDonald JE et al. Low expression of hexokinase-2 is associated with false-negative ^{18}F-FDG-positron emission tomography in multiple myeloma. *Blood* 2017; 130: 30-4.
24. Lapa C, Schreder M, Schirbel A et al. ^{68}Ga-Pentixafor-PET/CT for imaging of chemokine receptor CXCR4 expression in multiple myeloma - Comparison to ^{18}F-FDG and laboratory values. *Theranostics* 2017; 7: 205-12.
25. Pan Q, Luo Y, Cao X et al. Multiple Myeloma Presenting as a Superscan on ^{68}Ga-Pentixafor PET/CT. *Clin Nucl Med* 2018; 43: 462-3.
26. Pan Q, Cao X, Luo Y et al. Chemokine receptor-4 targeted PET/CT with ^{68}Ga-Pentixafor in assessment of newly diagnosed multiple myeloma: comparison to ^{18}F-FDG PET/CT. *Eur J Nucl Med Mol Imaging* 2020; 47: 537-46.
27. Pan Q, Luo Y, Cao X, Li J. ^{68}Ga-Pentixafor PET/CT Improves the Detection of Recurrent Myeloma in the Temporal Bone Masked by the Physiological ^{18}F-FDG Uptake of the Brain and Extraocular Muscles. *Clin Nucl Med* 2022; 47: e348-e50.
28. Buck AK, Haug A, Dreher N et al. Imaging of C-X-C Motif Chemokine Receptor 4 Expression in 690 Patients with Solid or Hematologic Neoplasms Using ^{68}Ga-Pentixafor PET. *J Nucl Med* 2022; 63: 1687-92.
29. Dreher N, Hahner S, Fuß CT et al. CXCR4-directed PET/CT with ^{68}Ga-pentixafor in solid tumors-a comprehensive analysis of imaging findings and comparison with histopathology. *Eur J Nucl Med Mol Imaging* 2024; 51: 1383-94.

Comparative study on the diagnostic value of ^{18}F-FDG PET/CT imaging and integrated PET/MR imaging in pediatric tumors

Xuemei Sun[1] **MD,**
Jiahe Gu[2] **MD**

1. Pediatric Department, Taizhou People's Hospital, Taizhou, China
2. Radiologic Department, Taizhou People's Hospital, Taizhou, China

Keywords: Pediatric tumors
- ^{18}F-FDG PET/CT imaging
- Integrated PET/MR imaging
- Diagnostic value

Corresponding author:
Jiahe Gu MD,
Radiologic department, Taizhou People's Hospital, Taizhou, China
Sanwang1985@163.com

Received:
12 October 2024
Accepted revised:
1 August 2025

Abstract

Objective: To analyze and compare the diagnostic value of fluorine-18-fluorodeoxyglucose (^{18}F-FDG) positron emission tomography/computed tomography (PET/CT) imaging and integrated PET/magnetic resonance imaging (MR) in pediatric tumors. **Subjects and Methods:** A retrospective analysis was conducted on the clinical data of 61 pediatric patients with malignant tumors admitted to our hospital from September 2022 to December 2023. All patients underwent pathological examinations as well as ^{18}F-FDG PET/CT and integrated PET/MR imaging. The pathological diagnosis results were used as the gold standard. Pearson correlation analysis, Bland-Altman analysis, and t-tests were used to compare the maximum standardized uptake value (SUVmax), signal-to-noise ratio (SNR), and target-to-background ratio (T/B) between the two methods. Chi-square tests were employed to compare the diagnostic efficacy differences of each index. **Results:** Among the 61 pediatric malignant tumor patients, a total of 417 lesions were detected, of which 363 lesions showed high uptake on both PET/MR and PET/CT. Among the remaining 54 PET-negative lesions, 9 were CT-positive but MR-negative, including 6 in the lungs and 3 in the vertebrae, while 12 lesions were MR-positive but CT-negative, including 5 in the liver, 4 in the brain, and 3 in the breasts. No statistically significant difference was found in the PET positivity rate or diagnostic results between the two devices ($P<0.05$). Bland-Altman analysis showed that the background uptake of PET/MR images was lower than that of PET/CT, and the SNR was higher ($P<0.05$); the SUVmax of the lesions on PET/MR was higher than that on PET/CT ($P<0.05$); the T/B value of PET/MR images was higher than that of PET/CT ($P<0.05$). In terms of correlation, the SUVmax, SNR, and T/B values between PET/MR and PET/CT were positively correlated ($r=0.919$, 0.507, 0.698, $P<0.05$). **Conclusions:** In the diagnosis of pediatric malignant tumors, PET/MR and PET/CT have relatively consistent lesion detection rates. PET/MR images have a higher SNR and better resolution, making them more advantageous than PET/CT for evaluating lesions in the liver, brain, and other soft tissue organs, thus warranting clinical application.

Hell J Nucl Med 2025; 28(2):131-136 *Epub ahead of print: 4 August 2025*

Introduction

In recent years, the incidence of pediatric tumors has been gradually rising, making it one of the leading diseases threatening children's health worldwide [1]. Early and accurate diagnosis is crucial for improving the survival rate and quality of life for pediatric tumor patients. Imaging examinations play a key role in the early detection, staging, and treatment evaluation of tumors [2]. Selecting an efficient and accurate imaging tool has become an important topic in clinical medicine. Currently, positron emission tomography/computed tomography (PET/CT) is widely used as a conventional imaging tool for tumor detection and staging [3]. Positron emission tomography/CT captures the metabolic activity of tumor cells in the body using the tracer fluorine-18-fluorodeoxyglucose (^{18}F-FDG) combined with anatomical information from CT, thus providing functional and anatomical images of tumor lesions [4]. However, PET/CT has certain limitations in soft tissue resolution, especially when detecting lesions in complex organs such as the liver and brain, where magnetic resonance imaging (MRI) often provides clearer images [5].

Integrated PET/MR, a rapidly developing imaging technology in recent years, combines PET's functional imaging with MRI's high-resolution anatomical imaging of soft tissues [6], offering the potential to provide more detailed and accurate information for the diagnosis of pediatric tumors. Compared to PET/CT, PET/MR can further improve tumor imaging quality, particularly in displaying lesions in the liver, brain, and other soft tissue organs. It also reduces radiation exposure, which is especially important for growing pediatric patients [7]. Therefore, PET/MR technology is considered an important development direction in future tumor diagnosis. Although PET/MR has advantages in imaging quality, its application is still in the early stages, and the costs are high, limiting its widespread adoption. Thus, comparing the diagnostic value of PET/MR and PET/CT in pediatric tumors has become a highly relevant research topic. For these reasons, this study aims to retrospectively analyze the imaging data of 61 pediatric patients with malignant tumors treated at our hospital, to explore the differences and advantages of ^{18}F-FDG PET/CT imaging and integrated PET/MR imaging in the diagnosis of pediatric tumors, and provide valuable references for clinical decision-making.

Subjects and Methods

Basic information

A retrospective analysis was conducted on the clinical data of 61 pediatric patients with malignant tumors who were admitted to our hospital between September 2022 and December 2023. These patients had clinical indications for staging or re-staging using PET/CT. Among the 61 patients, 24 were male and 37 were female; their ages ranged from 0 to 12 years, with an average age of (4.79±3.26) years. All patients underwent pathological examinations, as well as ^{18}F-FDG PET/CT imaging and integrated PET/MR imaging. The pathological results of the primary lesions were confirmed through postoperative pathology or biopsy pathology, while the diagnosis of metastatic lesions was based on a comprehensive clinical assessment.

Examination methods

^{18}F-FDG PET/CT imaging

Before undergoing ^{18}F-FDG PET/CT imaging, all patients were required to fast for at least 6 hours. At the time of ^{18}F-FDG injection, the blood glucose level of the patients had to be controlled below 7.8mmol/L. Each patient received an injection of ^{18}F-FDG at a dose of 3.7MBq/kg based on their weight, and whole-body scanning commenced 40 minutes after injection. During the scan, patients were positioned supine for static imaging. For younger patients or those unable to cooperate, sedation or hypnosis was induced 30 minutes prior to the examination using a 10% chloral hydrate solution administered orally or by enema. Additionally, all patients and their legal guardians signed informed consent forms before the examination.

The ^{18}F-FDG PET/CT imaging was performed using the Discovery 710 PET/CT system manufactured by GE, USA. For the CT portion, the tube voltage was set at 120kV, and the tube current was 120mA. The slice thickness and interval were both 3.75mm, with a pitch of 0.984mm, and the reconstructed slice thickness was 1.25mm. Positron emission tomography scanning was performed in 3D mode, with each bed position scanned for 3 minutes. Image reconstruction of the PET images employed the ordered subset expectation maximization (OSEM) algorithm, using time-of-flight (TOF) and point spread function (PSF) correction to improve image quality and accuracy.

Integrated PET/MR imaging

Immediately following the PET/CT scan, integrated PET/MR imaging was conducted using a SIGNA PET/MR (3.0 T) system manufactured by GE, USA, for whole-body imaging, with the patient remaining in a supine position. The MR sequences used in PET/MR scanning included axial LA-VA-Flex T1-weighted imaging, fat suppression (FS) PROPELLER T2-weighted imaging, and diffusion-weighted imaging (DWI) with a b-value of 800s/mm^2. The slice thickness was set at 6.0 mm, and the interslice gap was 1.0mm, with a field of view (FOV) of 34.0mm; for coronal scanning, the slice thickness was 5.5mm, with an interslice gap of 1.0mm, and the field of view was 42.0mm. The total examination time was approximately 40 minutes. Respiratory gating technology was employed during data acquisition to reduce respiratory motion artifacts. Positron emission tomography images were acquired in 3D mode, with both respiratory-gated data (about 3 minutes) and non-gated data (6 minutes) collected. The image reconstruction method used was also OSEM, with TOF and PSF correction to ensure consistency in image quality with PET/CT.

Image processing

Image processing was completed using GE's AW Server 2.0 workstation. High FDG uptake lesions detected in PET/MR and PET/CT imaging were marked, and their morphological information from MRI and CT scans was compared and analyzed. Additionally, lesions that did not show significant ^{18}F-FDG uptake on PET imaging but were highly suspected of being malignant based on MRI or CT were recorded and analyzed. All PET/MR lesions were compared with the corresponding PET/CT clinical reports to assess differences and complementarity between the two modalities. The size, location, and extent of the tumors were determined by combining the morphological characteristics of the tumors with the ^{18}F-FDG metabolic data. In both PET/MR and PET/CT images, regions of interest (ROI) were delineated, and the maximum standardized uptake value (SUVmax) for each ROI was measured. Additionally, the average liver background SUV and standard deviation were measured in the same planes and positions to ensure comparability of liver SUV values. Using these measurements, the target-to-background ratio (T/B) and the signal-to-noise ratio (SNR) of the PET images were calculated.

Result evaluation

Two experienced clinicians independently assessed the image quality using a double-blind method. The image quality grading standard was divided into four levels: Grade 1 indicated the image was not diagnostic; Grade 2 indicated poor image quality; Grade 3 indicated moderate quality; and Grade 4 indicated excellent quality. The characteristics of malignant tumors mainly included large tumor volume, lobulated or spiculated margins, punctate or "sand-like" calcifications, as well as signs of tumor invasion into surrounding tissues or distant metastasis, all of which were accompanied by significantly increased ^{18}F-FDG metabolism. Based on the above imaging features, PET/CT and PET/MR images were analyzed for diagnosis.

Statistical analysis

GraphPad Prism 8 software was used for plotting, and SPSS 22.0 software was used for data processing. Pearson correlation analysis was applied to compare the consistency of the SUV values between the two imaging modalities. Bland-Altman analysis and t-tests were conducted to compare SUV and T/B values between the two. The chi-square test was used to compare the differences in imaging results between the two modalities. A P-value of <0.05 was considered statistically significant.

Results

Pathology and follow-up results

The main tumor types in the 61 pediatric patients in this study included: 35 cases of neuroblastoma, accounting for the largest proportion; followed by 7 cases of nephroblastoma, 6 cases of rhabdomyosarcoma, 5 cases of pancreatoblastoma, 2 cases of adrenocortical carcinoma, and 6 cases of lymphoma. Among all diagnosed patients, a total of 417 lesions were detected, of which 351 were malignant (including primary lesions, tumor recurrence, and metastases), and 66 lesions were benign.

Comparison of imaging findings

Comparing the PET images from both methods, it was evident that PET images from PET/MR showed clearer lesions, with more pronounced uptake and better contrast. Bland-Altman analysis showed that PET/MR images had lower background uptake and higher SNR compared to PET/CT (P< 0.05); the SUVmax of lesions shown by PET/MR was higher than that of PET/CT (P<0.05); the T/B value of PET/MR images was higher than that of PET/CT (P<0.05), as shown in Table 1 and Figure 1. Regarding Pearson correlation, SUVmax, SNR, and T/B values between PET/MR and PET/CT were positively correlated (r=0.919, 0.507, 0.698, P<0.05), as shown in Figure 2.

During the study, 8 patients were unable to complete the PET/MR examination, with 6 of them becoming emotionally unstable due to prolonged fasting and scanning time, and the remaining 2 cases ending prematurely due to tumor-induced pain. Nevertheless, these patients successfully completed the PET/CT examination, and the aforementioned issues did not affect the final diagnostic results. In terms of subjective image quality scoring, approximately 98.4% of CT images met diagnostic standards, with artifacts mainly arising from respiratory motion, physiological artifacts from the intestines and bladder, etc.; about 95.1% of PET/MR images met diagnostic standards, with artifacts in MR images mainly caused by respiratory motion, vascular pulsation, and metal implants.

Comparison of PET/CT and PET/MR diagnostic results

In this study, a total of 417 lesions were detected among the 61 pediatric patients with malignant tumors. Positron emission tomography/MR and PET/CT both detected 363 lesions with high ^{18}F-FDG uptake. There were 54 lesions that did not show significant ^{18}F-FDG uptake on PET imaging (i.e., PET-negative). Among these PET-negative lesions, 9 were positive on CT imaging but did not show abnormalities on MR imaging; these included 6 lung lesions and 3 vertebral lesions. Conversely, 12 lesions were positive on MR imaging but undetected by CT imaging, including 5 liver lesions, 4 brain lesions, and 3 breast lesions.

In addition, new metastatic lesions were detected in 5 patients due to the advantages of PET/MR imaging and its high soft tissue resolution, resulting in changes in tumor staging. In 3 post-operative pancreatoblastoma patients, lesions originally suspected to be liver metastases were reclassified as benign lesions during PET/MR examination, avoiding incorrect treatment plans. The tumor T staging of 2 pelvic rhab-

***Table 1.** Comparison of Lesion SUVmax, SNR, and T/B Values ($\bar{x}\pm s$).*

Parameter	Value	Bland-Altman		t	P
		Mean Difference	95% CI		
CT-Lesion SUVmax	4.53±2.29	1.59	-0.83~4.02	3.283	0.001
MR-Lesion SUVmax	6.12±3.01				
CT-SNR	6.74±1.70	1.95	-2.79~6.64	4.686	<0.001
MR-SNR	8.69±2.77				
CT-T/B	4.25±2.53	3.07	-6.71~12.89	3.479	<0.001
MR-T/B	7.32±6.41				

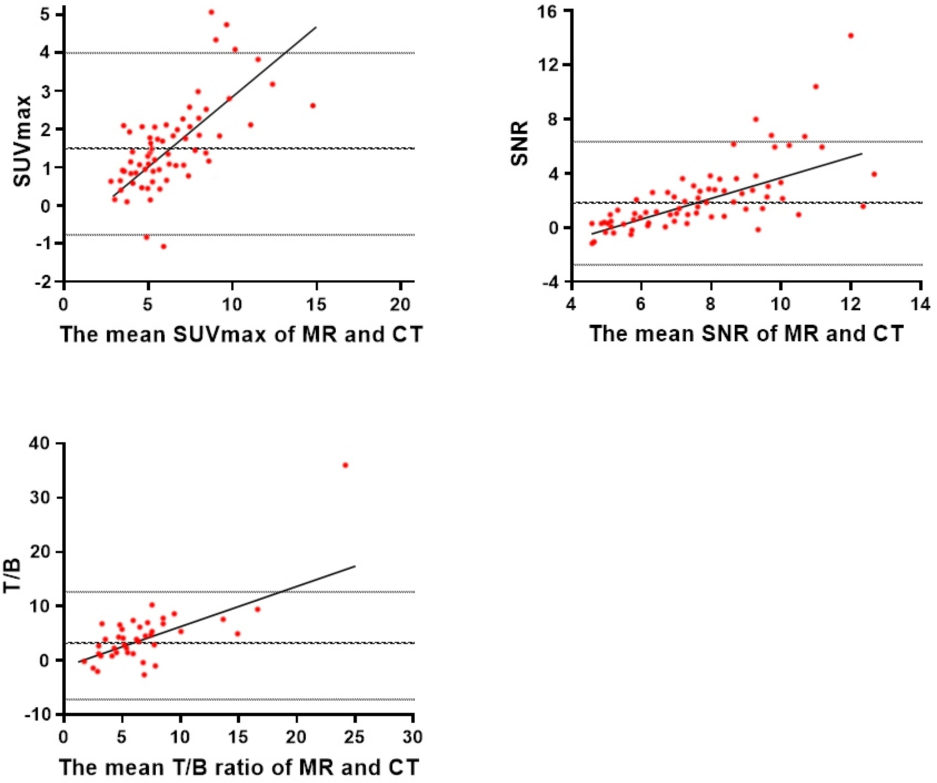

Figure 1. Bland-Altman plots comparing lesion SUVmax, SNR, and T/B values.

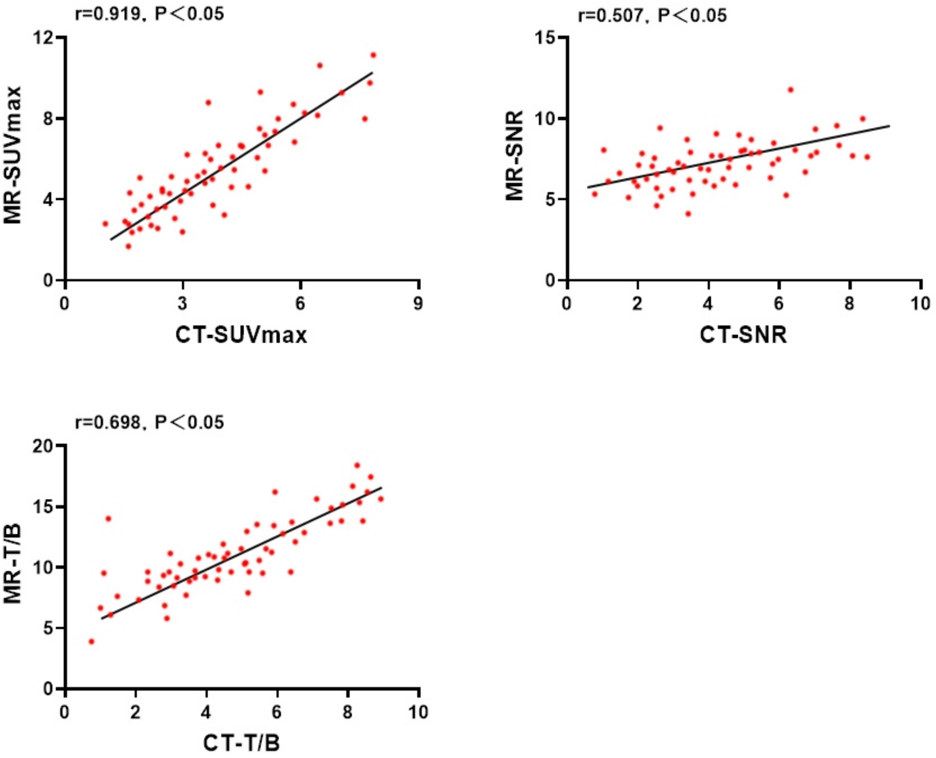

Figure 2. Correlation between lesion SUVmax, SNR, and T/B values in PET/MR and PET/CT.

domyosarcoma patients was adjusted after PET/MR imaging, demonstrating the advantages of PET/MR in pelvic soft tissue tumors. Moreover, in one case of lymphoma with pulmonary and systemic lymph node infiltration, PET/CT was found to be superior to PET/MR in T and N staging. It is worth noting that 8 patients who were initially scheduled for PET/MRI examinations were excluded from the analysis because they were unable to complete the procedure. Among these, 6 patients became emotionally unstable due to the prolonged scanning time, while 2 patients discontinued the exam prematurely due to tumor-related pain. The extended duration of the scan was particularly challenging, as prolonged immobilization is difficult for children, and sedation is not always a viable solution. In addition, claustrophobia, which can be exacerbated by the enclosed MRI environment, may further complicate the procedure in pediatric patients. These patients' results were not included in the final diagnostic comparison.

No significant difference was observed in the diagnostic results between the two devices across the 61 patients ($P > 0.05$).

Discussion

The diagnosis of pediatric malignant tumors often requires multiple imaging examinations, including X-ray, ultrasound, MRI, CT, and PET, which have been proven to have high sensitivity and specificity over the past few decades. These examinations play a crucial role in the detection, localization, and staging of tumors [8, 9]. However, for pediatric patients with malignant tumors, undergoing multiple imaging examinations can be time-consuming and may easily lead to issues like repeated sedation, causing unnecessary stress and risks to the child [10]. Therefore, optimizing the imaging examination process, reducing unnecessary examinations, and improving diagnostic accuracy and efficiency have become urgent issues for clinicians to address.

Among the existing imaging techniques, ^{18}F-FDG PET/CT is widely used in the staging, restaging, and therapeutic monitoring of pediatric malignant tumors due to its high sensitivity and specificity [11]. This technology allows for the detection of tumor lesions throughout the body via whole-body scanning, with a notable advantage in localizing recurrent and metastatic lesions [12]. However, conventional CT and MRI have their respective advantages and limitations in detecting tumor lesions in different regions [13]. For example, CT performs well in imaging bony structures, while MRI has a distinct advantage in soft tissue contrast. The results of this study demonstrate that the clinical application of whole-body integrated PET/MR is feasible, and it shows high consistency with PET/CT in lesion detection, with 96.1% of lesions accurately localized by either of these imaging modalities. In certain specific cases, lesions that were unclear on CT could be definitively diagnosed by MRI, and vice versa, suggesting that PET/MR and PET/CT have a degree of complementarity in imaging specific anatomical regions. Particularly in the imaging of soft tissue tumors, MRI's contrast advantage makes it superior to CT in detecting lesions in areas such as the liver, brain, and breast. In this study, of the 54 PET-negative lesions, 12 were confirmed as positive by MRI but were negative on CT, including 5 in the liver, 4 in the brain, and 3 in the breast. In this context, other studies have also supported the clinical value of PET/MR. Drzezga et al. (2012) [14] analyzed 32 patients with various tumors, confirming the feasibility of whole-body imaging with PET/MR and noting that the quality of PET images was similar to that of PET/CT. Furthermore, Saade-Lemus et al. (2020) [15] further revealed the advantages of PET/MR in anatomical localization, particularly in soft tissue-rich regions such as the head and neck, upper abdomen, and pelvis, where its contrast is significantly superior to that of PET/CT, increasing the accuracy of anatomical localization. Although PET/MR shows clear advantages in certain anatomical regions, PET/CT remains irreplaceable in the detection of lesions in areas such as the skeleton and lungs. In this study, of the 54 PET-negative lesions, 9 were confirmed as positive by CT but were negative on MRI, including 6 in the lungs and 3 in the vertebral bodies. Therefore, PET/MR and PET/CT can complement each other in tumor lesion imaging. The combination of both imaging techniques can provide more comprehensive diagnostic information, effectively improving diagnostic accuracy and avoiding misdiagnosis or missed diagnoses due to reliance on a single imaging modality.

Radiation dose management is crucial for pediatric patients. Compared with adults, children are more sensitive to ionizing radiation [16], so reducing radiation doses as much as possible while ensuring image quality is an important consideration in imaging examinations. Although ^{18}F-FDG PET/CT can provide precise diagnostic information for the staging and restaging of pediatric malignant tumors, the ionizing radiation risk it presents cannot be ignored [17]. In recent years, low-dose ^{18}F-FDG PET/CT technology has gained widespread attention, effectively reducing radiation exposure by lowering the activity of radiotracers and using low-dose CT scanning [18, 19]. However, PET/MR technology itself does not involve ionizing radiation, making it significantly advantageous compared to CT [20, 21], especially since its longer acquisition time allows for further reduction in the injected dose. Eldib et al. (2015) [22] demonstrated that by increasing the PET/MR acquisition time (which is required for MR imaging) from 8 minutes to 24 minutes, the ^{18}F-FDG dose could be reduced by up to 75%. Unlike the low-dose strategy of PET/CT, PET/MR relies on its longer MR scanning time. Thus, by matching the PET acquisition time with the MR imaging time, it is possible to maintain high-quality images while reducing the dose of radiotracers.

Conclusion and limitations

This study compared the application effects of ^{18}F-FDG PET/CT and PET/MR in the diagnosis of pediatric malignant tumors. The results indicate that PET/MR and PET/CT exhibit high consistency in the detection of most lesions, with both technologies showing certain complementarity in specific anatomical regions. Therefore, combining the two techniques allows for more comprehensive lesion localization, which helps improve diagnostic accuracy in complex cases while reducing the harm caused by ionizing radiation to children. It should be noted that, despite many valuable conclusions drawn from this study, there are still some limitations that need to be addressed and explored in future research: 1) Limited sample size: The sample size of this study is relatively small, covering only a limited number of pediatric patients with malignant tumors, which may limit the generalizability of the study results; 2) Insufficient lesion classification: This study did not conduct detailed classification and subgroup analysis of different types of tumor lesions, while different types of tumors may exhibit significant differences in imaging characteristics and lesion growth patterns; 3) Technical Challenges and Feasibility for Pediatric Populations: While PET/MR offers clear advantages, particularly in soft tissue resolution, its widespread clinical use, especially in pediatric populations, is hindered by certain challenges. The extended scan duration required for PET/MR makes it difficult for younger patients to remain still, often necessitating sedation. However, sedation is not always a viable solution due to medical risks and individual patient factors. Additionally, the enclosed nature of the PET/MR scanner increases the likelihood of claustrophobia, further complicating its use in children. These factors highlight the need for further technical advancements, as well as patient-centered strategies, to improve the feasibility and accessibility of PET/MR imaging in clinical practice; 4) Lack of long-term prognosis data: This study primarily focused on the accuracy of diagnosis and the optimization of examination processes but lacked an analysis of the impact of imaging examinations on patients' long-term prognosis. In summary, this study made some progress in the selection and optimization of imaging technologies for the diagnosis of pediatric malignant tumors. However, limitations remain in terms of sample size, lesion classification, cost-benefit analysis, and the lack of long-term prognosis data, which need to be further improved and refined in future research.

Bibliography

1. Kattner P, Strobel H, Khoshnevis N et al. Compare and contrast: pediatric cancer versus adult malignancies. *Cancer Metastasis Rev* 2019; 38(4): 673-82.
2. Llanos D, de la Pedraja Í, Campos L et al. Imaging palpable tumors in pediatrics. *Radiologia (Engl Ed)* 2022; 64(6): 552-65.
3. Kroeze E, Padilla LA, Burkhardt B et al. ^{18}F-FDG-PET/CT imaging in diagnostic workup of pediatric precursor B-cell lymphoblastic lymphoma. *Pediatr Blood Cancer* 2023; 70(11): e30642.
4. Agrawal A, Shah S, Gnanasegaran G et al. PET/CT Normal Variants and Pitfalls in Pediatric Disorders. *Semin Nucl Med* 2021; 51(6): 572-83.
5. States LJ, Reid JR. Whole-Body PET/MRI Applications in Pediatric Oncology. *Am J Roentgenol* 2020; 215(3): 713-25.
6. Pedersen C, Aboian M, McConathy JE et al. PET/MRI in Pediatric Neuroimaging: Primer for Clinical Practice. *Am J Neuroradiol* 2022; 43(7): 938-43.
7. Giraudo C, Carraro S, Zucchetta P, Cecchin D. Pediatric Imaging Using PET/MR Imaging. *Magn Reson Imaging Clin N Am* 2023; 31(4): 625-36.
8. Handa A, Nozaki T, Makidono A et al. Pediatric oncologic emergencies: Clinical and imaging review for pediatricians. *Pediatr Int* 2019; 61(2): 122-39.
9. Boterberg T, Dunlea C, Harrabi S et al. Contemporary paediatric radiation oncology. *Arch Dis Child* 2023; 108(5): 332-7.
10. Tydings C, Kim A. Technology and precision therapy delivery in childhood cancer. *Curr Opin Pediatr* 2020; 32(1): 1-6.
11. Chen W, Liu L, Li Y et al. Evaluation of pediatric malignancies using total-body PET/CT with half-dose ^{18}F-FDG. *Eur J Nucl Med Mol Imaging* 2022; 49(12): 4145-55.
12. Geitenbeek RTJ, Martin E, Graven LH et al. Diagnostic value of ^{18}F-FDG PET-CT in detecting malignant peripheral nerve sheath tumors among adult and pediatric neurofibromatosis type 1 patients. *J Neurooncol* 2022; 156(3): 559-67.
13. Voss SD. Staging and following common pediatric malignancies: MRI versus CT versus functional imaging. *Pediatr Radiol* 2018; 48(9): 1324-36.
14. Drzezga A, Souvatzoglou M, Eiber M et al. First clinical experience with integrated whole-body PET/MR: comparison to PET/CT in patients with oncologic diagnoses. *J Nucl Med* 2012; 53(6): 845-55.
15. Saade-Lemus S, Teixeira SR, Vossough A et al. Emerging Roles of PET/MR in the Pediatric Hospital. *PET Clin* 2020; 15(3): 253-69.
16. Kutanzi KR, Lumen A, Koturbash I, Miousse IR. Pediatric Exposures to Ionizing Radiation: Carcinogenic Considerations. *Int J Environ Res Public Health* 2016; 13(11): 1057.
17. Voss SD. Functional and anatomical imaging in pediatric oncology: which is best for which tumors. *Pediatr Radiol* 2019; 49(11): 1534-44.
18. Zhao YM, Li YH, Chen T et al. Image quality and lesion detectability in low-dose pediatric ^{18}F-FDG scans using total-body PET/CT. *Eur J Nucl Med Mol Imaging* 2021; 48(11): 3378-85.
19. Yu S, Qian Z, Liu H et al. Optimized low-dose positron emission tomography/computed tomography schemes in pediatric tumor patients: a randomized clinical trial. *Transl Pediatr* 2022; 11(9): 1510-20.
20. Saade-Lemus S, Nevo E, Soliman I et al. Clinical pediatric positron emission tomography/magnetic resonance program: a guide to successful implementation. *Pediatr Radiol* 2020; 50(5): 607-17.
21. Connor K, Aldridge MD, Gallegos C. Understanding the Experience of Mothers of Medically Complex Children through Photojournaling. *J Mod Nurs Pract Res* 2022; 2(2): 5.
22. Eldib M, Bini J, Lairez O et al. Feasibility of ^{18}F-Fluorodeoxyglucose radiotracer dose reduction in simultaneous carotid PET/MR imaging. *Am J Nucl Med Mol Imaging* 2015; 5(4): 401-7.

Characteristics of PET/CT uptake in the salivary glands in T1N0M0-T2N0M0 glottic cancer

Yukinori Okada[1] MD,
Tatsuhiko Zama[1] MD,
Tomohiro Itonaga[1] MD,
Ryuji Mikami[1] MD,
Mtsuru Okubo[1] MD,
Shinji Sugahara[1] MD,
Shiho Wada[1] MD,
Masumi Kawaguchi[1] MD,
Tsubasa Kawamoto[1] MD,
Masanori Ishida[1] MD,
Motoki Nakai[1] MD,
Koichiro Abe[1] MD,
Mana Yoshimura[1] MD,
Takashi Kodama[2] MSC,
Masahiko Kurooka[2] MSC,
Kazuhiro Saito[1] MD

1. Tokyo Medical University Department of Radiology, Tokyo, Japan
2. Tokyo Medical University Hospital Department of Radiation Therapy, Tokyo, Japan

Keywords: Positron emission tomography - Hypertension - Salivary glands - Glottic neoplasms - ^{18}F-FDG

Corresponding author:
Yukinori Okada MD
Tokyo Medical University
Department of Radiology, Tokyo, Japan
igaueno512@yahoo.co.jp

Received:
27 May 2025
Accepted revised:
10 August 2025

Abstract

Objective: This study aimed to identify factors influencing salivary gland uptake in fluorine-18-fluorodeoxyglucose (^{18}F-FDG) positron emission tomography/computed tomography (PET/CT). **Subjects and Methods:** We retrospectively reviewed patients aged 20-95 years diagnosed with T1N0M0 or T2N0M0 glottic carcinoma between July 2019 and March 2025, who underwent PET/CT for initial staging and radiotherapy planning. Maximum standardized uptake value (SUVmax) and total lesion glycolysis (TLG) were measured and compared based on gender, smoking history, hypertension, diabetes mellitus, dyslipidemia, stage, and primary tumor site. **Results:** A total of 61 patients were included (mean age, 68.3±12.4 years; 57 male, 4 female). The cohort included 41 patients with T1N0M0 and 20 with T2N0M0 disease. Hypertension status was negative in 32, positive in 28, and unknown in 1; diabetes status was negative in 54, positive in 6, and unknown in 1; dyslipidemia status was negative in 51, positive in 9, and unknown in 1. Smoking history was negative in 7, positive in 53, and unknown in 1. Primary tumor accumulation was observed in 44 patients, while 17 showed no uptake at the primary site. The mean SUVmax of the right submandibular gland was 3.16±0.70 on the left, it was 3.05±0.76. In the right gland, median SUVmax was significantly higher in patients without hypertension 3.350 than in those with hypertension 2.725; $P<0.01$. In the left gland, median SUVmax was significantly higher in patients without hypertension 3.18 than in those with hypertension 2.56; $P<0.01$). **Conclusions:** In T1N0M0-T2N0M0 glottic carcinoma, ^{18}F-FDG uptake in the submandibular glands is reduced in patients with hypertension.

Hell J Nucl Med 2025; 28(2): 137-144

Introduction

The salivary glands are secretion organs in the body, present as paired structures on the left and right sides. They are classified into major and minor salivary glands. The parotid, submandibular, and sublingual glands comprise the major salivary glands. Minor salivary glands are located in the oral and pharyngeal mucosa. Technetium-99m-pertechnetate ($^{99m}TcO_4^-$) salivary gland scintigraphy is used to evaluate salivary gland function. Both scintigraphy and single photon emission computed tomography (SPECT) detect gamma rays. Positron emission tomography (PET) detects annihilation radiation emitted in two opposing directions. In PET practice, glucose analog radiopharmaceuticals, such as fluorine-18-fluorodeoxyglucose (^{18}F-FDG), are used to diagnose tumors, cardiac disease, and large vessel vasculitis. Fluorine-18-FDG accumulation occurs in normal organs as well as tumors and inflammation. In 78 head and neck cancer-free patients, visual and quantitative evaluations at 11 sites showed accumulation in the sublingual gland in 72%, the submandibular gland in 53%, and the parotid gland in 51% of cases [1]. The mean standardized uptake value (SUV) was reported as 2.93 for the sublingual gland, 2.11 for the submandibular gland, and 1.90 for the parotid gland [1]. In a review of 98 cases, the mean SUV of the sublingual gland was reported as 3.3±1.5 [2].

The accumulation dose of ^{18}F-FDG in the salivary glands is associated with salivary gland function and has been reported as useful in evaluating adverse events following radiotherapy [3]. In 47 patients with head and neck cancer, the parotid gland volume decreased by 3.9%±1.9% for every 10Gy increase in mean dose post-radiotherapy and by 16.9%±1.9% within 3 months after treatment. Additionally, in these 47 individuals, the parotid gland volume decreased by 3.9%±1.9% with each 10Gy dose increment and by 16.5%±7.3% within 3 months following radiotherapy. The mean SUV of ^{18}F-FDG in the parotid gland SUVmean was 1.63±0.48 before treatment initiation. The mean salivary gland dose decreases by 5.2%± 2.5% with more than a 10Gy increase, and salivary gland function declines when the mean dose exceeds 32Gy [4].

Conversely, other studies suggest that salivary gland function may also be reduced due to systemic conditions. In basic medical research, salivary gland function was shown to be impaired in the presence of hypertension [5, 6]. Furthermore, individuals with diabetes exhibit reduced salivary gland function under both stimulated and unstimulated conditions [7]. In a cohort of 4544 patients with head and neck cancer, comorbidities were reported in over 90% of cases, with hypertension and diabetes present in approximately 60% and 17%-18% of patients, respectively [8]. In 131 individuals over 70 years old with T1N0M0 Stage I glottic carcinoma, hypertension, ischemic heart disease, emphysema, diabetes mellitus, and Chen's disease were observed in about 60% of cases [8]. Poor survival outcomes were reported in individuals with three or more of the following five conditions: hypertension, ischemic heart disease, emphysema, diabetes mellitus, and a history of myocardial infarction [9]. These findings suggest a potential for salivary gland dysfunction in patients with head and neck cancer even before initiating radiotherapy due to comorbidities such as hypertension and diabetes; however, detailed investigations are lacking. This study aimed to evaluate factors influencing ^{18}F-FDG accumulation in the salivary glands on PET/CT among patients with early-stage glottic carcinoma, a group in which radiotherapy is the primary treatment and which commonly presents with lifestyle factors such as alcohol consumption and smoking, as well as hypertension and diabetes.

Subjects and Methods

Study design

This was a single-center, retrospective, and case-control study.

Patient selection

We selected patients with T1N0M0 and T2N0M0 glottic carcinoma (squamous cell carcinoma) who underwent PET/CT for initial staging and radiotherapy planning at Tokyo Medical University Hospital from July 2019 to March 2025. The age range at selection was 20 to 95 years. We excluded the following patients: those with untreated overlapping cancers identified through clinical judgment, histopathology, endoscopy, CT, PET/CT, or magnetic resonance imaging (MRI) at the time of glottic carcinoma diagnosis; those with a history of other cancers (excluding glottic carcinoma) who had undergone drug therapy, radiotherapy, or surgery for metastatic or recurrent disease during radiotherapy for glottic carcinoma; those whose PET/CT was not performed at our hospital; those who declined data use; those whose families declined data use due to difficulty in decision-making caused by significant cognitive decline; and those enrolled in other clinical trials or studies. However, we included the following: patients with a history of cancer who were untreated or under observation at the time of radiotherapy for glottic carcinoma, patients not initially enrolled in clinical trials at the time of radiotherapy but later included for other purposes in other departments. Patients with synchronous bilateral glottic carcinomas (double cancer) and those with partial tumor removal by microlaryngeal surgery were also included.

PET/CT analysis

We used PET/CT performed prior to radiotherapy planning for initial staging. Fluorine-18-FDG (Nihon Medi-Physics Co., Ltd., Tokyo, Japan) was administered intravenously at a dose of 3.7MBq/kg based on body weight. The patient then rested for 1h. Positron emission tomography/CT imaging was performed using a Discovery MI (SiPM, Q clear, GE Healthcare, Hino, Japan). Positron emission tomography/CT analysis was conducted by Y.O, a board-certified radiation oncologist, nuclear medicine specialist, and certified PET nuclear medicine specialist. Positron emission tomography/CT images were imported into MIM Maestro (Euro Meditech Co., Ltd., Tokyo, Japan/MIM Software Co., Ltd., Cleveland, OH, USA) for analysis. Maximum SUV and, when applicable, total lesion glycolysis (TLG) were measured in the bilateral submandibular and parotid glands. The SUVmax and TLG values were automatically calculated from regions of interest configured by Y.O.

Contrast with clinical background

Fluorine-18-FDG accumulation was compared across age, gender, medical history, and the presence or treatment of hypertension, diabetes, dyslipidemia, other comorbidities, smoking history, blood glucose level at PET/CT and ^{18}F-FDG dose. The presence of hypertension, diabetes mellitus, dyslipidemia, other comorbidities, and smoking history was defined based on corresponding entries in the medical records; the absence of these conditions was defined as the lack of corresponding documentation.

Statistical analysis

Easy R (EZR), developed by the Jichi Medical University Saitama Medical Center, was used as the statistical software [10]. The Mann-Whitney U test was employed to compare the two groups. A logistic model was applied for univariate and multivariate analysis. Receiver operating characteristic (ROC) analysis was used to calculate the cut-off vale, area under the curve, sensitivity and specificity. Statistical significance was defined as $P<0.05$.

Ethical considerations

This study was approved by the Tokyo Medical University Hospital Ethics Committee (Approval No. T2025-0015). This study was conducted in accordance with the principles of the 1964 Declaration of Helsinki. An opt-out form was published on the hospital website. Only patients who provided consent for data use through the patient questionnaire at the Radiation Therapy Department consultation were included.

Previous study

This study includes patients from a previous study by Okada et al. (2022) [11]. That study focused on primary tumor accumulation and radiotherapy dose distribution. In contrast, the design of the current study targeted salivary gland accumulation, differentiating it from the prior work. Accordingly, this was conducted as a new and independent study.

Table 1. *Patient background.*

Factor	Result
Patients	61
Age	68.3±12.4
Sex	Male: 57 Female: 4
Stage	T1N0M0: 41 T2N0M0: 20
Tumor site	Unilateral: 57 Bilateral: 4
Hypertension	No: 32 Yes: 28 Unknown: 1
Diabetes	No: 54 Yes: 6 Unknown: 1
Dyslipidemia	No: 51 Yes: 9 Unknown: 1
Smoking history	No: 7 Yes: 53 Unknown: 1
Other comorbidities	Hyperthyroidism: 1 Hypothyroidism: 1 Collagen disease: 3 Dialysis: 1 Sarcoidosis: 1 Heart failure: 2 Myocardial infarction: 1 Cardiac surgery: 1
^{18}F-FDG dose	243.3±45.0MBq
Blood glucose level at PET/CT	106.7±13.5mg/dL
Primary site at PET/CT uptake	Yes: 44 No: 17

Mbq, mega becquerel; mg/dL, milligrams per deciliter; PET/CT, posit-ron emission tomography-computed tomography; ^{18}F-FDG, fluorine-18 fluorodeoxyglucose

Results

Patient selection

From 62 patients who met the inclusion criteria, one 82-year-old male patient (T2N0M0, squamous cell carcinoma) was excluded due to intense ^{18}F-FDG accumulation in the cervical muscles, which interfered with salivary gland evaluation. A total of 61 patients were included in this study.

The mean age was 68.3±12.4 years (range 40 year to 94 year); 57 were male, and 4 were female. In total, 41 had T1N0M0 Stage I, and 20 had T2N0M0 Stage II disease.

Unilateral primary glottic cancer was present in 57 patients. Bilateral primary glottic cancer was observed in one T1N0M0 case and three T2N0M0 cases. All patients had squamous cell carcinoma.

Hypertension status was positive in 32 patients, negative in 28, and unknown in 1. Antihypertensive medication names were recorded in 26 cases.

Furthermore, diabetes status was positive in 6, negative in 54, and unknown in 1.

Dyslipidemia status was positive in 9, negative in 51, and unknown in 1. Seven patients had no smoking history, 53 had a history of smoking, and 1 patient's smoking status was unknown. Data are summarized in Table 1.

Other comorbidities were noted in 11 patients: hyperthyroidism (n=1), hypothyroidism (n=1), collagen disease (n= 3), dialysis (n=1), sarcoidosis (n=1), heart failure (n=2), myocardial infarction (n=1), and cardiac surgery (n=1)). These results are shown in Table 1.

PET/CT

The dose of ^{18}F-FDG was 243.3±45.0MBq. The blood glucose level at the time of PET/CT examination was 106.7±13.5 mg/dL. Positron emission tomography/CT showed accumulation at the primary lesion in 44 patients and no accumulation in 17 patients. The results are shown in Table 1.

Evaluation of PET/CT in submandibular gland

The mean value of SUVmax in the right submandibular gland was 3.16±0.70, and the mean value of TLG was 14.6± 8.57mL ×SUV. The mean value of SUVmax in the left submandibular gland was 3.05±0.76, and the mean value of TLG was 13.7±6.81mL ×SUV. The mean value of sum SUVmax in the right plus left submandibular gland (both side) was 6.21±1.43 and The mean value of sum TLG in right and left submandibular gland (both side) 28.3±12.8mL×SUV.

In the right submandibular gland, the median SUVmax was 3.350 in the group without hypertension and 2.725 in the group with hypertension; this difference was statistically significant (P<0.01) (Figure 1). In the left submandibular gland the median SUVmax was 3.18 in the group without hypertension and 2.56 in the group with hypertension; this difference was statistically significant (P<0.01) (Figure 2). In the right plus left (both) submandibular gland, the median sum of SUVmax (in the right plus left submandibular gland) was 6.61 in the group without hypertension and 5.38 in the group with hypertension; this difference was statistically significant (P<0.01) (Figure 3). By univariate and multivariate analysis for for the sum (right plus left submandibular gland) of the SUVmax (median value <5.97 and ≥5.97) using age, sex (male/female), smoking history (yes/no), diabetes (yes/no), dyslipidemia (yes/no), other comorbidities (yes/no), ^{18}F-FDG dose, blood glucose level at PET/CT, a statistically significant value was found for hypertension in univariate analysis [odds ratio (OR), 0.18; 95% confidence interval (CI), 0.06-0.55; P< 0.01) and blood glucose level at PET/CT [odds ratio (OR), 0.95; 95% confidence interval (CI), 0.91-0.993; P =0.022) A a statistically significant values were found for hypertension (OR, 0.17; 95% CI, 0.04-0.62; P<0.01). and blood glucose level at PET/CT [odds ratio (OR), 0.94; 95% confidence interval (CI) 0.88-1.00; P=0.04] in multivariate analysis.There results are shown in Table 2.

In the right submandibular gland, the median TLG was 14.0mL ×SUV in the group without hypertension and 12.6mL ×SUV in the group with hypertension; this difference was no statistically significant (P =0.84). In the left submandibular gland, the median TLG was 14.8mL ×SUV in the group without hypertension and 12.5mL ×SUV in the group with hypertension; this difference was no statistically significant (P =0.39) In the right plus left (both) submandibular gland, the median sum TLG (in the right plus left submandibular gland) was 28.8mL ×SUV in the group without hypertension and 24.0mL ×SUV in the group with hypertension; this difference was no statistically significant (P=0.65).

About the median sum of SUVmax (in the right plus left submandibular gland), ROC analysis show the area under the curve 0.758, 95% confifence interval 0,633- 0.883, sensitivity 0,714, specificity 0,750 with cut-off vale 5.730 (Figure 4). By univariate analysis for the sum (right plus left submandibular gland) of the SUVmax (cut-off vale value <5.73 and ≥5.73, a statistically significant value was found for hypertension in univariate analysis [odds ratio (OR), 0.19; 95% confidence interval (CI), 0.06–0.56; P <0.01.

About the blood glucose level at PET/CT, ROC analysis show the area under the curve 0.585, 95% confifence interval 0,436-0.735, sensitivity 0,429, specificity 0,781 with cut-off vale 114mg/dL. By univariate analysis for the blood glucose level at PET/CT, a statistically significant value was found for hypertension in univariate analysis [odds ratio (OR), 3.25; 95% confidence interval (CI), 1.02-10.40; P =0.047).

Evaluation of PET/CT in the parotid gland

The SUVmax of the right parotid gland was 2.44±0.40 and the mean value of TLG was 33.6±13.1mL ×SUV. The SUVmax of the left parotid gland was 2.49±0.63 and the mean value of TLG was 35.0±17.5mL ×SUV.

The mean value of sum SUVmax in the right plus left parotidar gland (both side) was 4.4±0.93 and the mean value of sum TLG in right and left parotid gland (both side) 69.6± 29.1mL ×SUV.

By univariate and multivariate analysis for for the sum

Table 2. *Correlation between the sum of f SUVmax (in the right plus left submandibular gland) and other factors.*

Factors for sum of SUVmax at right plus left (both) submandibular gland (median value <5.97 and ≥5.97)	**Single variate analysis**			**Multivariate analysis**		
	Odds ratio	95%CI	P value	Odds ratio	95%CI	P value
Age	0.98	0.94-1.01	0.27	1.02	0.95-1.09	0.57
Sex (male/female)	1.04	0.14-7.87	0.97	18.8	0.181900	0.21
Smoking history (yes/no)	0.36	0.06-2.01	0.24	0.04	0.00-2.13	0.11
Hypertension (yes/no)	0.18	0.06-0.55	<0.01	0.17	0.04-0.62	<0.01
Diabetes (yes/no)	0.17	0.02-1.58	0.12	0.12	0.00-1.70	0.12
Dyslipidemia (yes/no)	1.30	0.31-5.40	0.72	1.81	0.30-11.1	0.52
Other comorbidities (yes/no)	0.49	0.13-1.87	0.30	0.35	0.05-2.21	0.26
Blood glucose level	0.95	0.91-0.99	0.02	0.94	0.88-1.00	0.04
^{18}F-FDG dose	1.00	0.99-1.01	0.61	1.00	0.98-1.01	0.65

SUVmax, maximum standardized uptake value; CI, confidence interval; P, P-value; OR, odds ratio.

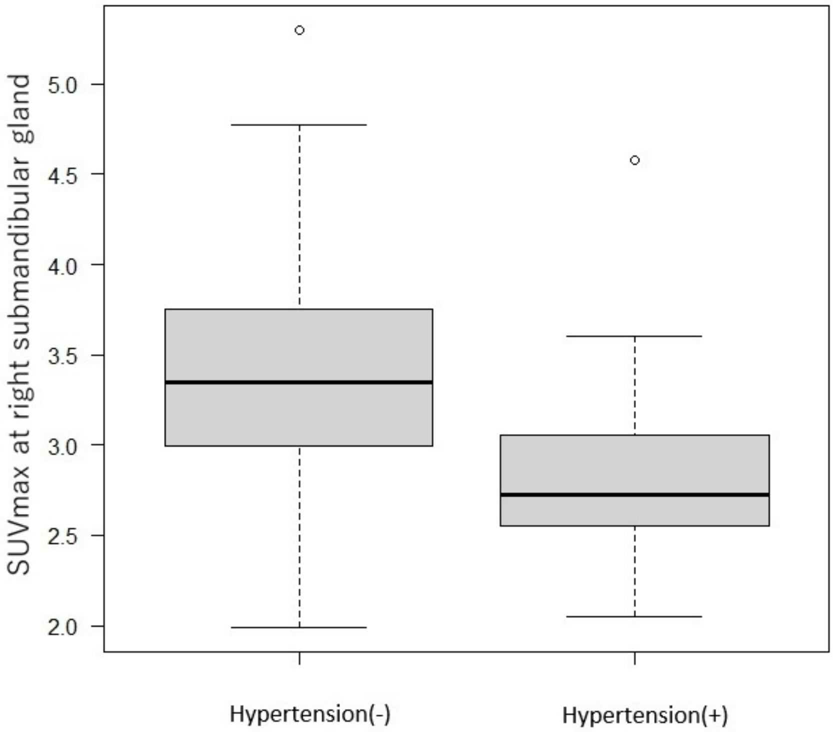

Figure 1. Relationship between SUVmax in the right submandibular gland and hypertension.

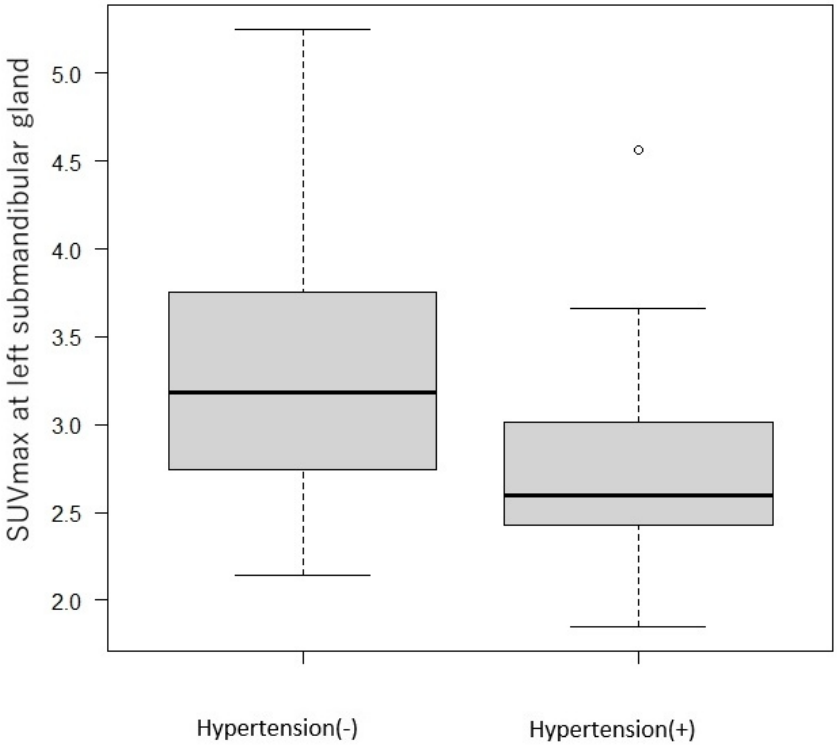

Figure 2. Relationship between SUVmax in the left submandibular gland and hypertension.

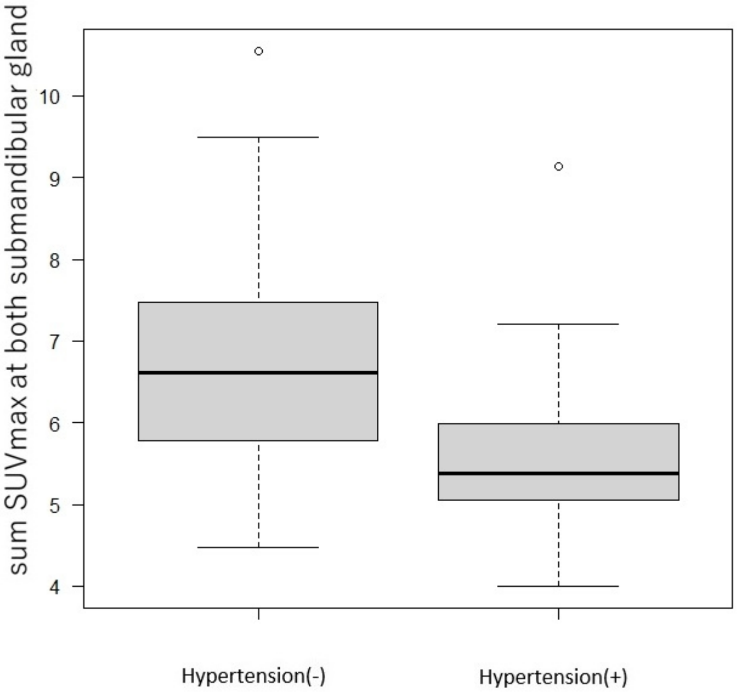

Figure 3. Relationship between the sum of SUVmax in the right plus left (both) submandibular gland and hypertension.

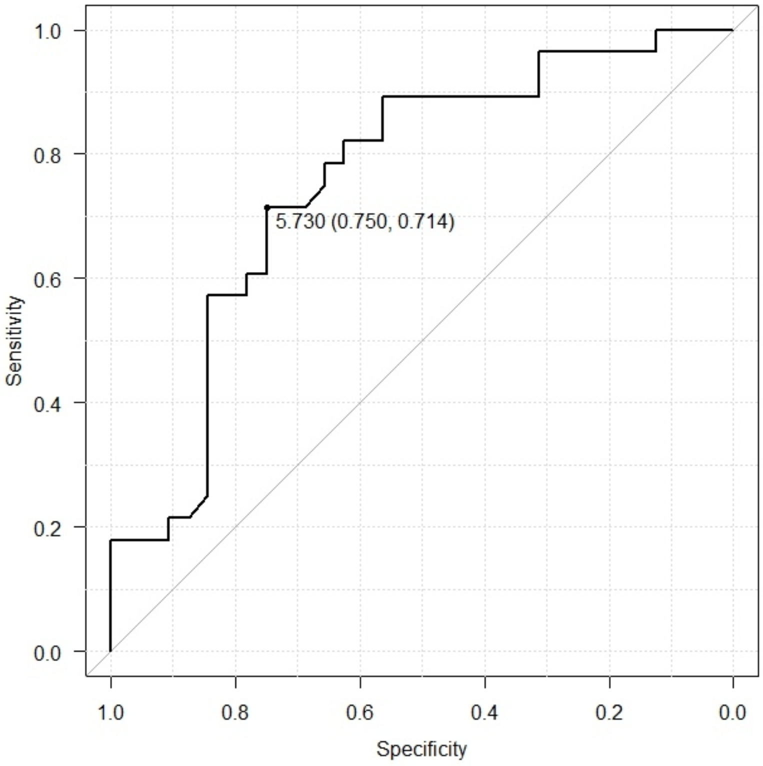

Figure 4. ROC analysis about the sum of SUVmax in the right plus left (both) submandibular gland and hypertension.

(right plus left parotidr gland) of the SUVmax (median value <4.85 and ≥4.85) using age, sex (male/female), smoking history (yes/no), diabetes (yes/no), dyslipidemia (yes/no), other comorbidities (yes/no), ^{18}F-FDG dose, blood glucose level at PET/CT, a there are no statistically significant factor. There results are shown in Table 3.

Discussion

In this study the blood glucose level at the time of PET/CT is associated the sum of SUVmax at right and left (both) submandibular gland. But, no statistically significant association was found between diabetes and the sum of SUVmat at right and left (both) submandibular gland in this study. Although the small number of diabetic patients may have influenced this result, it cannot be concluded that diabetes is associated with submandibular ^{18}F-FDG accumulation based on our findings. In head and neck cancer, salivary gland hypofunction is a significant side effect following radiotherapy. In 137 patients treated for head and neck cancer, 40% developed moderate-to-severe xerostomia 12 months after treatment. A predictive model using the 90th percentile ^{18}F-FDG uptake in the parotid gland and the average uptake level was reported to outperform models based on baseline xerostomia or salivary gland dose. In 161 head and neck cancer patients, 90th percentile uptake and texture analysis of ^{18}F-FDG in the parotid gland were also reported to be associated with oral dryness 12 months after radiotherapy [14]. In 56 patients with head and neck cancer, 29 (51.8%) developed Grade 2 or higher xerostomia, and the overall and relative changes in median SUV in the parotid gland (SUVmedian) 3 weeks after the start of radiotherapy correlated with moderate-to-severe xerostomia at 6 months [15]. Median SUV increased in both the ipsilateral and contralateral parotid glands at 3 weeks compared to baseline, and increases in ipsilateral SUVmedian and contralateral mean parotid dose were correlated with xerostomia [16]. Fluorine-18-FDG may be useful in predicting salivary gland hypofunction and xerostomia during radiotherapy, and in 2024, a model was developed to predict these outcomes based on ^{18}F-FDG accumulation in 540 patients with head and neck cancer [17]. In contrast, Itonaga et al. (2022) reported the utility of salivary gland scintigraphy using $^{99m}TcO_4^-$ [18]. In that study of 31 patients with head and neck cancer treated with radiotherapy, 46Gy was identified as the threshold for salivary gland recovery [18]. The 90th percentile signal intensity on T1-weighted MRI performed before radiotherapy in 68 patients was reported as a predictor of intraoral dryness 12 months post-treatment [19]. A 2024 meta-analysis indicated that decreased ^{18}F-FDG PET/CT uptake and increased ADC on MRI during radiotherapy for head and neck cancer were associated with reduced patient numbers [20]. Magnetic resonance imaging during

Table 3. *Factors affecting the accumulation of ^{18}F-FDG in the parotid gland.*

Factors for sum of SUVmax at right plus left (both) parotid gland (median value <4.85 and ≥4.85)	**Single variate analysis**			**Multivariate analysis**		
	Odds ratio	95%CI	P value	Odds ratio	95%CI	P value
Age	0.98	0.18-55.5	0.44	0.95	0.90-1.02	0.20
Sex (male/female)	3.33	0.33-34.0	0.31	1.10	0.06-18.0	0.95
Smoking history (yes/no)	1.49	0.30-7.33	0.82	3.51	0.43-26.8	0.24
Hypertension (yes/no)	0.39	0.14-1.10	0.08	0.45	0.14-1.41	0.17
Diabetes (yes/no)	0.43	0.07-2.56	0.35	0.30	0.04-2.39	0.26
Dyslipidemia (yes/no)	1.20	0.29-5.00	0.80	2.06	0.41-10.4	0.38
Other comorbidities (yes/no)	0.30	0.07-1.24	1.00	0.34	0.06-1.78	0.20
Blood glucose level	0.99	0.95-1.02	0.45	1.01	0.96-1.05	0.80
^{18}F-FDG dose	1.00	0.99-1.01	0.78	0.99	0.9-1.00	0. 15

SUVmax, maximum stand; SUVmax, maximum standardized uptake value; ^{18}F-FDG, fluorine-18-fluorodeoxyglucose; P, P-value.

treatment was also reported as predictive of post-radiotherapy oral dryness and decreased salivary gland function [20]. Although this study did not assess periodontal disease, a large prospective cohort of 2,588 individuals in Suita, Osaka, reported an association between hypertension and periodontal disease [21]. Taken together, hypertension may contribute to oral deterioration, including submandibular gland hypofunction, oral dryness, and periodontal disease. We believe that reducing the radiation dose to the submandibular gland is just as important as dose reduction to the parotid gland during radiotherapy planning, particularly in patients with hypertension. Attention should also be given to oral environment deterioration linked to submandibular gland dysfunction.

Recently, Intensity-Modulated Radiation Therap (IMRT) is performed for cancer radiotherapy. IMRT can reduce the radiation dose at normal organ. By using IMRT for head and neck cancer patietns and reduce the mean parotid radiation dose under 30.0Gy, the oral health-related quality of life (HR-QOL) after radiotherapy was well preserved [22]. From the results of this research, we think that reduce the radiation dose at submandibular gland using IMRT is useful in protecting salivary duct function in head and neck cancer patients with hypertension.

There are some limitations in this study. It was restricted to early-stage glottic cancer; the number of cases was limited; it was a retrospective analysis; and there was no comparison with salivary secretory function or periodontal disease. Further research through prospective clinical trials with larger sample sizes is needed.

In conclusion, in T1N0M0–T2N0M0 glottic carcinoma, PET/CT findings indicate that ^{18}F-FDG accumulation in the submandibular gland is reduced in patients with hypertension.

The authors declare that they have no conflicts of interest.

Acknowledgments

The idea for this study was derived from the content on the website of the Fujiyoshi Orthodontic Clinic (Saliva and Disease | Fujiyoshi Orthodontic Clinic).

Bibliography

1. Nakamoto Y, Tatsumi M, Hammoud D et al. Normal ^{18}F-FDG distribution patterns in the head and neck: PET/CT evaluation. *Radiology* 2005; 234(3): 879-85.
2. Wan Y, Chiu E, Rosenberg J et al. Standardized uptake value atlas: characterization of physiological 2-deoxy-2-[^{18}F]fluoro-D-glucose uptake in normal tissues. *Mol Imaging Biol* 2007; 9(2): 83-90.
3. Cannon B, Schwartz DL, Dong L. Metabolic imaging biomarkers of postradiotherapy xerostomia. *Int J Radiat Oncol Biol Phys* 2012; 83(5): 1609-16.
4. Roach MC, Turkington TG, Higgins KA et al. ^{18}F-FDG-PET assessment of the effect of head and neck radiotherapy on parotid gland glucose metabolism. *Int J Radiat Oncol Biol Phys* 2012; 82(1): 321-6.
5. Zhang J, Zhong L, Wang Y et al. Proteomic analysis reveals an impaired Ca2+/AQP5 pathway in the submandibular gland in hypertension. *Sci Rep* 2017 Nov 6;7(1): 14524.
6. Shen ZJ, Han YC, Wag YN et al. LncRNA and mRNA expression profiles and functional networks of hyposalivation of the submandibular gland in hypertension. *Sci Rep* 2020; 10(1): 13972.
7. Mata AD, Margues D, Rocha S et al. Effects of diabetes mellitus on salivary secretion and its composition in the human. *Mol Cell Biochem* 2004; 261(1-2): 137-42.
8. Rubn SJ, Wu KY, Kirke DN et al. Head and neck cancer comorbidities in the geriatric population based on hospital case volume. *Ear Nose Throat J* 2021; 100(2): NP62-NP68.
9. Malecka AM, Malecki R, Amrogowiez N, Biesaga B. Prognostic factors in elderly patients with T1 glottic cancer treated with radiotherapy. *Sci Rep* 2021; 11(1): 17717.
10. Kanda Y. Investigation of the freely available easy-to-use software 'EZR' for medical statistics. *Bone Marrow Transplant* 2013; 48(3): 452-8.
11. Okada Y, Zama T, Itonaga T et al. PET/CT findings and dose distribution during radiotherapy in T1N0M0–T2N0M0 glottic cancer. *Hell J Nucl Med* 2024; 27(1): 27-34.
12. Kawamoto M, Yamada S, Gibo T et al. Relationship between dry mouth and hypertension. *Clin Oral Investig* 2021; 25(9): 5217-25.
13. Nakamura S, Nakatani K, Yoshino K et al. Effects of glucose intolerance on physiological accumulation in salivary glands and palatine tonsils during ^{18}F-fluorodeoxyglucose positron emission tomography. *Cureus* 2024; 16(8): e67387.
14. Li Y, Sijtsema NM, Vette SPMd et al. Validation of the ^{18}F-FDG PET image biomarker model predicting late xerostomia after head and neck cancer radiotherapy. *Radiother Oncol* 2023; 180: 109458.
15. Dijk LV, Noordzij W, Brouwer CL et al. ^{18}F-FDG PET image biomarkers improve prediction of late radiation-induced xerostomia. *Radiother Oncol* 2018; 126(1): 89-95.
16. Trada Y, Lee MT, Jameson MG et al. Mid-treatment ^{18}F-FDG PET imaging changes in parotid gland correlates to radiation-induced xerostomia. *Radiother Oncol* 2023; 186: 109745.
17. Li Y, Dekker MIcR, Vette SPM et al. Late-xerostomia prediction model based on ^{18}F-FDG PET image biomarkers of the main salivary glands. *Radiother Oncol* 2024; 196: 110319.
18. Itonaga T, Rkuuye K, Mikami R et al. Scintigraphy and recovery thresholds for salivary glands. *Br J Radiol* 2022; 95(1130): 20210718.
19. Dijk ZV, Thor M, Steenbakkers RJHM et al. Parotid gland fat related magnetic resonance image biomarkers improve prediction of late radiation-induced xerostomia. *Radiother Oncol* 2018; 128(3): 459-66.
20. Guevelou Le, Novello XP, Kammerer E et al. Assessment and prediction of salivary gland function after head and neck radiotherapy: A systematic review. *Cancer* 2024; 13(24): e70494.
21. Kawabata Y, Ekumi D, Miwa H et al. Relationship between prehypertension/hypertension and periodontal disease: A prospective cohort Study. *Am J Hypertens* 2016; 29(3): 388-96.
22. Parliament MB, Scringer RA, Anderson SG et al. Preservation of oral health-related quality of life and salivary flow rates after inverse-planned intensity- modulated radiotherapy (IMRT) for head-and-neck cancer. *Int J Radiat Oncol Biol Phys* 2004;58(3): 663-73.

The effect of radiation on living beings

Andreas Otte MD

Peter Osypka Institute of Medical Engineering, Department of Electrical Engineering, Medical Engineering and Computer Science, Offenburg University, Germany

Keywords: Radiation risk
- Direct/indirect radiation effects
- Henri Becquerel - Atomic bomb
- Nuclear reactor accident

Corresponding author:
Prof. Andreas Otte,
Peter Osypka Institute of Medical Engineering, Department of Electrical Engineering, Medical Engineering and Computer Science, Offenburg University,
Badstr. 24, D-77652 Offenburg,
Germany,
andreas.otte@hs-offenburg.de

Received:
9 Jul 2025
Accepted revised:
14 Jul 2025

Abstract

This overview covers the effects of radiation on living organisms, including risks and legal requirements. It defines basic radiation terms, such as ionization, activity, energy dose, or equivalent dose, and explains direct and indirect radiation effects. It also lists foods that should be avoided after a reactor accident, including the topic of iodine prophylaxis.

Hell J Nucl Med 2025; 28(2): 145-148 *Epub ahead of print: 4 August 2025* *Published online: 30 August 2025*

Introduction

Inspired by Wilhelm Conrad Rontgen's (1845-1923) discovery of "X-rays," Antoine Henri Becquerel (1852-1908) [1, 2] investigated uranium compounds for their phosphorescence in 1896 and demonstrated a hitherto unknown type of radiation that blackens photographic plates independently of external influences, in particular excitation by solar radiation: uranium rays. In the same year, he published seven papers on this subject [3-9]. In 1901, Becquerel wrote retrospectively in Nature [10]:

"At the commencement of the year 1896, in carrying out some experiments with the salts of uranium, the exceptional optical properties of which I had been studying for some time, I observed that these salts emitted an invisible radiation, which traversed metals and bodies opaque to light as well as glass and other transparent substances. This radiation impressed a photographic plate ... The phenomenon does not appear to be influenced by any known external cause, such as a variation of temperature or a luminous excitation; it is entirely different from phosphorescence; is not weakened in an appreciable manner by time, even at the end of several years; and is emitted spontaneously without any apparent exciting cause."

Becquerel certainly could not have imagined the benefits his discovery would bring to radiology. Today, radioactive substances have become indispensable in modern diagnostics and are of great benefit to many patients: in single-photon emission computed tomography (SPECT), positron emission tomography (PET) or their hybrid technologies combining nuclear medicine with radiology. The use of radioactive substances has also become useful in drug research: For example, some active pharmaceutical ingredients can be directly radioactively labelled with (diagnostic) gamma or positron emitters in order to visualize the mechanism of action of the new drug in the body and to determine pharmacokinetic and pharmacodynamic data from it [11], e.g., in eletriptan, a migraine drug, the intracranial distribution could be studied with PET by directly labelling eletriptan with the positron marker ^{11}C [11, 12].

But radioactive substances are also used for treatment. For example, monoclonal antibodies or peptides are being developed for the treatment of various types of cancer (e.g., non-Hodgkin's lymphomas, neuroendocrine carcinomas), which can be labelled with a beta emitter and used for internal, receptor-mediated radiation therapy [13, 14]. Already early, external radiation with radioactive isotopes was performed: Famous composer Giacomo Puccini, e.g., was treated with radium in 1924 for his laryngeal cancer [15].

Not even 50 years after Becquerel´s discovery, on August 6, 1945, the world's first atomic bomb fell on Hiroshima, and three days later the second on Nagasaki. The extent of the destruction and the effects of the exposed radiation, which continue to this day, exceed anything previously imaginable in an unbearable way. Numerous nuclear weapons tests followed, e.g., at the Bikini Atoll between 1946 and 1958 or in the Nevada Desert between 1951 and 1992, and the peaceful use of nuclear energy also showed its dangers in the reactor meltdown at Chernobyl in 1986 and in 2011 in Fukushima.

Legal requirements

The disasters of Hiroshima and Nagasaki have triggered the formation of various organizations that regulate the legal basis for the use of ionizing radiation at the international, European and national levels. Particularly noteworthy here are the recommendations of the *International Commission of Radiological Protection (ICRP)*, which are the basis for the *European Atomic Energy Act* (EUROATOM) at the international level and, e.g., the Atomic Energy Act in Germany. EURATOM was founded on 25 March 1957 by France, Italy, Benelux countries and Germany within the framework of the *Treaties of Rome* and deals with the handling of radioactive substances.

In addition to EURATOM, there are a number of other organisations; however, their influence on national legislation can be assessed as small:

- UNSCEAR: United Nations Scientific Committee on the Effects of Atomic Radiation (Wien),
- ILO: International Labour Organization of the UN (Geneva),
- IAEA: International Atomic Energy Agency (Vienna),
- WHO: World Health Organization

Radiation risk

When it comes to the effect of radiation on living beings, a distinction must be made between stochastic and deterministic risk:

- **Stochastic risk** is a random event without a threshold dose. If the dose increases, the probability of the risk also increases. Examples of a stochastic radiation risk are genetic DNA damage or tumor induction. The dose size is the effective dose in the mSv range.
- In the **case of deterministic risk**, on the other hand, there is a threshold dose above which the extent of the damage increases with increasing dose. Examples of deterministic radiation damage are radiation erythema or so-called radiation sickness. The dose size is the organ dose in the Sv range.

Stochastic risk

The ICRP 60 (1990) publication bases its recommendations and findings primarily on studies of survivors of the atomic bomb explosions of Hiroshima and Nagasaki [16]. In doing so, it reassessed its earlier data from publication 26 (from 1977) due to a longer observation period, a new dosimetry system and new relative/multiplicative risk models for the extrapolation of stochastic risk. ICRP 60 (1990) determined deaths from radiation-induced cancer per 10,000 people and per sievert at 500 (5%/Sv). The formula 5%/Sv is the stochastic radiation risk for the occurrence of a fatal radiation-induced cancer.

Deterministic risk

In humans, the threshold dose for deterministic radiation damage is 2Sv; transient signs of fatigue and concentration disorders already occur here. At 3 to 4Sv, the median lethal dose $LD_{50/30d}$ is reached. This means that 50% of people die after 30 days at this dose. At 7Sv you have reached the absolute lethal dose, and at >100Sv you are dead immediately.

Poisoning with radioactive material is a case of its own. Pollonium-210 (^{210}Po), e.g., a powerful alpha emitter which decays to lead (^{206}Pb) and has a physical half-life of 138 days, is a radioactive element to which every human being is constantly exposed, but if ingested in high amounts it can lead to vomiting, pain in the abdomen, diarrhea and severe dehydration at the beginning and, in the following days, to hair loss, mucositis and a decrease in platelets and leukocytes until finally multi-organ failure occurs [17].

The $LD_{50/30d}$ for living organisms, bacteria and viruses differs because they have different sensitivity to ionizing radiation.

Radiation terms

Ionizing radiation

Radioactive substances generate ionizing radiation. Ionizing radiation is any particle or electromagnetic radiation that can remove electrons from atoms or molecules so that positively charged ions or molecular residues remain (ionization). These can be the following types of radiation: gamma radiation, X-rays, shorter-wave UV radiation, alpha radiation, beta radiation or free neutrons.

In addition to the direct radiation effect of these ionizing radiation, it is the indirect radiation effect in particular that can cause decisive damage to the cell. This results in reactive products of the radiolysis of the water, which are not provided for in the cell environment and produce an indirect radiation effect through chemical reactions with biomolecules [18].

Activity

The activity of a radioactive substance is the average number of atomic nuclei that decay radioactively per second. The SI unit is the becquerel (Bq), where 1Bq=1 decay/s.

Energy dose

The energy dose D is the mass-specific amount of energy absorbed by an irradiated object over a period of exposure. It depends on the intensity of the irradiation, the absorption capacity of the irradiated material for the given type and energy of radiation, and geometric factors. The SI unit is the gray (Gy), where 1Gy=1J/kg.

Equivalent dose

The equivalent dose H is a measure of the strength of the biological effect of a given radiation dose. This means that equivalent doses of the same size are comparable in their effect on a living being, regardless of the type and energy of radiation.

The following applies: $H=w_R \times D$ where w_R is the radiation weighting factor (formerly quality factor); for gamma radiation and beta radiation it is 1 each, for other types of radiation it can be up to 20 (e.g., w_R of alpha radiation: 20). The dose conversion factor can be used to estimate the equivalent dose from the activity. The SI unit of the equivalent dose is sievert (Sv), where 1Sv =1J/kg.

Direct/indirect radiation effects

Direct radiation effects

Direct radiation effects occur when energy is transferred directly to a biomolecule (DNA, RNA, protein, etc.) by ionizing radiation. A single event may be sufficient to trigger a biological effect (single-hit process); however, multiple hits are sometimes necessary (multi-hit process).

Indirect radiation effect

An organic cell consists mainly of water. Ionizing radiation is therefore very likely (up to 80%) to be absorbed by water molecules. This produces the following reactive products of water radiolysis:

- hydrogen peroxide,
- molecular hydrogen,
- hydrated electrons,
- H and OH radicals,
- in the presence of O_2, also superoxide radicals O_2^- and HO_2.

These products are not intended to be present in the cellular environment and cause indirect radiation effects through chemical reactions with biomolecules.

Mainly the OH radicals produced during water radiolysis (and the subsequent radicals formed by them) react with proteins and cause damage there [18]. They cause the following reactions in proteins (biomolecules):

- Protein (P) + $^{\cdot}$OH→ P-OH→ radical migration
- P$^{\cdot}$OH+P$^{\cdot}$OH→HO-P-P-OH→ recombination reaction, which leads to conformational and possibly structural changes in the protein molecule

Both reactions (radical migration and recombination) are dose-dependent. The probability of recombination increases when the dose rate reaches high values and decreases at low dose rates.

Factors influencing the effect of radiation

The effect of radiation on biomaterial must be regarded as a complex biophysical process that depends on a variety of factors:

- the radiation dose,
- the type of radiation,
- the spatial dose distribution,
- the temporal dose distribution (in fractionated irradiation, radiation damage to healthy cells in the low dose range can be repaired during the irradiation-free intervals; in tumor tissue, the repair capacity is lower; in prolonged irradiation, cell damage can accumulate to a greater extent),
- the tissue environment (a high oxygen content increases the sensitivity of cells to ionizing radiation),
- the radiation sensitivity of the tissue (tissue with a high cell division rate is more sensitive to radiation than tissue with a low cell division rate).

Accumulation in the food chain

After a reactor accident, certain foods should be avoided. At the site of the accident, radioactive substances are deposited in the soil and can then be found in the food chain, sometimes for decades. Important radionuclides in this context are ^{131}I and ^{137}Cs:

- ^{131}I has a physical half-life of 8.02 days. The limit for this radionuclide in Japan at the time of the Fukushima accident was 2000Bq/kg in food and 300Bq/l in tap water.
- ^{137}Cs, on the other hand, has a physical half-life of 30.17 years. The limit for this long-lived radionuclide in Japan was 500Bq/kg in food.

Since the half-life of a radioactive substance is subject to the law:

$$N(t) = N_0\left(\frac{1}{2}\right)^{\frac{t}{t_{1/2}}}$$

with: $N(t)$: activity by time t, N_0: initial activity (at time t=0), $t_{1/2}$: physical half-life,
1/8 of the initial activity is measured after 3 half-lives and 1/1024 after 10 half-lives. In ^{137}Cs, the activity is still present at 1/8 after 90 years.

The problem in the food chain is the animals, as they cannot recognize contaminated food. In particular, food contaminated with ^{131}I and ^{137}Cs is fish from the region of a reactor accident. If one looks at the reactor accident in Fukushima, these were mainly fish from the North Pacific such as Alaska pollock, plaice, wild salmon or monkfish. The neighbouring countries and regions were also affected. In the disaster area itself, people had to do without fresh food from the field (especially spinach leaves), meat, fresh milk, sausage and dairy products, mushrooms and berries, and resort to canned food.

Potassium iodide tablets with stable ^{127}I are intended to prevent released radioactive ^{131}I from entering the thyroid gland, in whose follicles iodine is produced for the production of the thyroid hormones triiodothyronine and tetraiodothyronine, also known as thyroxine. This is done by saturating the thyroid gland with non-radioactive ^{127}I from the potassium iodide tablet. This saturation prevents further uptake of radioactive ^{131}I, as the thyroid gland does not distinguish between radioactive and non-radioactive iodine.

However, iodine tablets should never be taken on your own initiative, but only on the recommendation of authorities. From about 45 years of age, there is also a risk of induction of thyroid disease when taking iodine tablets indiscriminately. You should also ask about a possible iodine allergy.

The intake of iodine tablets after the reactor accident in Fukushima was not necessary in Europe.

Radiation in medical diagnostics

In medical imaging diagnostics, radioactive substances and X-rays are used in a targeted manner. However, the radiation doses used are very low and are within the range of radiation exposure that we are already exposed to in Europe through natural annual terrestrial radiation. In our opinion, this does not justify any fear of radiation used in medical diagnostics, and overall, as with all other medical procedures, especially ionizing imaging techniques, it is necessary to carefully weigh the benefits and risks.

Conclusion

In 1908, Becquerel became president of the *Académie des Sciences*. In the same year, on August 25, he died at the age of only 55 from radiation disease in *Le Croisic (Loire-Atlantique)* in Brittany. Becquerel was able to experience the *Belle Époque*; fortunately, he was spared from World War I. His discovery is invaluable to medicine and has also catalyzed many other discoveries in modern atomic physics. Becquerel certainly could not have foreseen the danger that his discovery might bring at the time.

A new type of weapon had been found.

Bibliography

1. Otte A. Wenn der Name zur Einheit wird: Antoine Henri Becquerel [When a name becomes a unit: Antoine Henri Becquerel]. *Radiologe* 2017; 57(2): 111-2.
2. Otte A. Röntgen, Becquerel and radiation. *Nature* 2020; 580(7801): 29.
3. Becquerel H. Sur les radiations émises par phosphorescence. In: *Comptes Rendus de l'Académie des sciences* 1896; 122: 420-1.
4. Becquerel H. Sur les radiations invisibles émises par les corp s phosphorescents. In: *Comptes Rendus de l'Académie des sciences* 1896; 122: 501-3.
5. Becquerel H. Sur quelquer propriétés nouvelles des radiations invisibles émises par divers corps phosphorescents. In: *Comptes Rendus de l'Académie des sciences* 1896; 122: 559-64.
6. Becquerel H. Sur les radiations invisibles émises par les sels d'uranium. In: *Comptes Rendus de l'Académie des sciences* 1896; 122: 689-94.
7. Becquerel H. Sur les propriétés différentes des radiations invisibles émises par les sels d'uranium, et du rayonnement de la paroi anticathodique d'un tube de Crookes. In: *Comptes Rendus de l'Académie des sciences* 1896; 122: 762-67.
8. Becquerel H. Émission de radiation nouvelles par l'uranium métallique. In: *Comptes Rendus de l'Académie des sciences* 1896; 122: 1086-88.
9. Becquerel H. Sur diverses propriétés des rayons uraniques. In: *Comptes Rendus de l'Académie des sciences* 1896; 123: 1086-88.
10. Becquerel H (1901) The radio-activity of matter. *Nature* 1901; 63(1634): 396-8.
11. Otte A, Rosé C, Zähringer A, Maier-Lenz H. New clinical technologies in drug development (article in German). *Internist* 2008; 49: 232-7.
12. Otte A, Hilliard B, Taylor K, Rubens R. The intracranial distribution of eletriptan: a combined [^{11}C]-eletriptan/[^{15}O]CO/[^{15}O]H_2O positron emission tomography (PET) study. *Eur J Nucl Med Mol Imaging* 2003; 30 (Suppl. 2): S292.
13. Otte A, Mueller-Brand J, Dellas S et al. Yttrium-90-labelled somatostatin-analogue for cancer treatment. *Lancet* 1998: 351: 417-8.
14. Otte A, Van de Wiele C, Dierckx RA. Radiolabelled immunotherapy in non-Hodgkin's lymphoma - the next step. *Nucl Med Commun* 2009; 30: 5-15.
15. Otte A. Giacomo Puccini (1858-1924) and his terminal disease (article in German). *Arch Kriminol* 2024; 253: 123-6.
16. ICRP Publication 60: 1990 Recommendations of the International Commission on Radiological Protection. *Annals of the ICRP* 1990; 21: 1-3.
17. Nathwani AC, Down JF, Goldstone J, et al. Polonium-210 poisoning: a first-hand account. *Lancet* 2016; 388: 1075-80.
18. Stark G. The effect of ionizing radiation on lipid membranes. *Biochim Biophys Acta* 1991; 1071: 103-22.

The efficacy and safety of ^{225}Ac-PSMA RLT targeted therapy for metastatic castration-resistant prostate cancer: A systematic review and meta-analysis

Huajun Liu[1,2,3,4] **Bsc,**
Ma Jiao[1,2,3,4] **MSc,**
Junzheng Wang[1,2,3,4] **BSc,**
Chunyin Zhang[1,2,3,4] **MD**

1. Department of Nuclear Medicine, Affiliated Hospital of Southwest Medical University, Luzhou, Sichuan, China,
2. Nuclear Medicine and Molecular Imaging Key Laboratory of Sichuan Province, Luzhou, Sichuan, PR China,
3. Laboratory for Targeted Radiopharmaceuticals Creation, Luzhou, Sichuan, China,
4. Institute of Nuclear Medicine, Southwest Medical University, No. 25, Taiping St, Luzhou 646000, Sichuan, China

Abstract

Objective: Using radiolabeled prostate-specific membrane antigen (PSMA) ligands for the treatment of metastatic prostate cancer is a promising therapeutic approach. This systematic review and meta-analysis aims to assess the efficacy and safety of actinium-225 (^{225}Ac)-PSMA radioligand therapy (RLT) for prostate cancer. **Materials and Methods:** The systematic review and meta-analysis adheres to the preferred reporting items for systematic reviews and meta-analyses (PRISMA). Searches were conducted in databases including PubMed, Web of Science, Medline, CNKI, and VIP, for studies related to ^{225}Ac-PSMA RLT for prostate cancer from inception until April 2024. The primary endpoint was the therapeutic effect as measured by post-treatment biochemical response evaluation criteria, while secondary endpoints included evaluating overall survival (OS), progression-free survival (PFS), molecular responses, etc. **Results:** A total of 17 studies involving 1042 patients were included. The pooled proportion of patients with PSA reduction was 85% (95% confidence interval [CI]: 80%-91%), and the pooled rate of PSA reduction >50% was 66% (95% CI: 58%-75%). The combined values for OS and PFS were 13.79 months (95% CI: 11.11-16.48 months) and 9.67 months (95% CI: 6.99-12.35 months), respectively. The molecular response rate was 71% (95% CI: 56-87%). The most common side effect of ^{225}Ac-PSMA RLT was xerostomia, accounting for 63.5%. Anemia, leukopenia, thrombocytopenia, and renal toxicity were observed in 54.3%, 30.4%, 31.8%, 32.0%, respectively. **Conclusions:** Actinium-225 -PSMA RLT is an effective and safe treatment for metastatic castration-resistant prostate cancer (mCRPC) patients, with a low incidence of treatment-related adverse reactions. Additionally, a history of lutetium-177 (^{177}Lu) treatment may have an impact on PSA reduction in mCRPC patients.

Hell J Nucl Med 2025; 28(2): 149-167 *Epub ahead of print: 4 August 2025* *Published online: 30 August 2025*

Keywords: ^{225}Ac, - PSMA-targeted radioligand therapy
- Metastatic castration resistant prostate cancer
- Meta-analysis

Corresponding author:
Chunyin Zhang MD,
Department of Nuclear Medicine,
The Afliated Hospital of
Southwest Medical University,
Luzhou, Sichuan, PR China
zhangchunyin345@sina.com

Received:
24 September 2024
Accepted revised:
15 July 2025

Introduction

Prostate cancer (PCa) is the most common malignancy in men globally. According to the 2023 Annual Cancer Report, prostate cancer has the highest incidence among male cancer cases in the United States, accounting for approximately 29%, making it the second leading cause of cancer-related deaths in men, representing around 11% [1]. The incidence of prostate cancer varies significantly by region, traditionally with lower rates in Asia. However, due to increasing economic levels, aging populations, Westernized lifestyles, and improved prostate cancer detection, the incidence of prostate cancer in Asia is rapidly rising [2-4]. Current treatment methods for prostate cancer primarily include radical surgical removal, chemotherapy, radiotherapy, and androgen deprivation therapy (ADT). However, these treatment approaches are not always curative, and patients may eventually develop metastatic castration-resistant prostate cancer (mCRPC), which is a major cause of patient mortality [4-6]. Although certain treatments such as taxane chemotherapy (docetaxel and cabazitaxel), immunotherapy, next-generation hormone therapies (abiraterone, enzalutamide), and targeted therapies have been approved for mCRPC, resistance mechanisms and adverse reactions may limit the improvement in prognosis and quality of life for some patients [7-10]. Prostate-specific membrane antigen (PSMA) is a type II transmembrane glycoprotein located on the cell membrane, with increased specific expression in prostate cancer [11-12]. Radioligand therapy (RLT) involves injecting a therapeutic dose of a radiolabeled ligand into the body. When the ligand reaches the target cells, the radiolabel releases alpha particles and/or beta particles, causing DNA single-strand or double-strand breaks, leading to cell death. With a half-life of 9.9 days, actinium-225 (^{225}Ac) produces 4 alpha particles, 2 beta particles, and gamma photons during its decay. The short range of alpha rays enables the destruction of tumor cells with minimal damage to surrounding normal tissues, making it a favorable choice for patients with bone marrow infiltration. The high energy of alpha rays also makes it suitable for treating beta-resistant prostate cancer cells [13-15]. Clinical trials have evaluated efficacy and safety of ^{225}Ac-PSMA-RLT for the treatment of metastatic prostate cancer. However, only a limited number of systematic reviews or meta-analyses are available on the efficacy and safety of ^{225}Ac-PSMA RLT for metastatic prostate cancer, and the literature included mostly consists of small sample, retrospective studies. The present study aimed to analyze various clinical trials published on ^{225}Ac-PSMA RLT for metastatic prostate cancer, in order to provide further evidence for this treatment.

Materials and Methods

This systematic review adhered to the preferred reporting items for systematic reviews and meta-analyses (PRISMA) guidelines [16].

Search strategy

A systematic search was conducted from inception till April 2024 in PubMed, Web of Science, Medline, CNKI, and VIP for studies on ^{225}Ac-PSMA therapy for prostate cancer. The search terms included ("Prostate Cancer" OR "Prostate Tumor") AND "PSMA" AND ("^{225}Ac" OR "^{225}-Actinium"). In case of duplicate records (from the same trial or institution), the most comprehensive one was chosen. However, if two studies included partially different patient populations (overlap rate <50%), they were considered separately.

Inclusion criteria

Study population: Studies including more than 10 patients diagnosed with mCRPC and positive for ^{68}Ga-PSMA-11 imaging; intervention: ^{225}Ac-PSMA RLT for at least one cycle; Outcome: The primary endpoints were any level of prostate-specific antigen (PSA) decline and PSA decline >50%.

Exclusion criteria

Studies with fewer than 10 included patients; duplicate publications, reviews, case reports, communications, abstracts, dosimetry studies, and letters to the editors.

Quality assessment

Two researchers (HJL, JM) independently conducted the systematic search and study selection. Disagreements were resolved through discussion with a third reviewer. Ultimately, 17 studies were selected, and the methodological quality of all included studies was assessed using the Newcastle-Ottawa Scale (NOS). (Studies with NOS scores ≥ 6 were considered to have better quality).

Statistical analysis

All data were analyzed using STATA version 17.0 for meta-analysis. Treatment efficacy was evaluated using PSA decline and PSA decline >50%. Additionally, overall survival (OS), progression-free survival (PFS), molecular responses, and treatment-related toxicities were assessed for all studies. Forest plots were generated for analysis. The I^2 statistic and chi-square test were used for heterogeneity testing. If there was no significant heterogeneity among studies ($I^2 \leq 50\%$, $P> 0.10$), a fixed-effects model was used to pool the data. If significant heterogeneity was present among studies ($I^2>50\%$, $P\leq 0.10$), subgroup analysis was conducted, and a random-effects model was used to pool the data.

Results

Literature search results

According to the predetermined search strategy, a total of 228 relevant articles were retrieved. After removing 126 duplicate articles, there were 102 remaining. Upon preliminary review of the titles and abstracts, 80 articles were excluded. Of the remaining articles, 30 were review articles and meta analyses, 14 were preclinical studies, 12 were related to radiopharmaceuticals or drugs, 12 studied dosimetry or imaging, 7 were case reports or brief communications, and 5 were unrelated to PSMA therapy. Further reading of the full texts led to the exclusion of 5 articles. Two articles by Sathekge et al. and Banda et al. focused on metastatic hormone-sensitive prostate cancer, while one by Kremser et al. investigated the prognostic value of neutrophil-to-lymphocyte ratio in prostate cancer patients undergoing radionuclide therapy. Langbein et al. and Feuerecker et al. each contributed 2 articles solely examining salivary gland toxicity of radionuclide therapy. Finally, a total of 17 articles were included [17-33], as shown in Figure 1.

Results

Literature quality assessment and information of studies included

Ultimately, 17 studies were included, comprising 1042 study subjects. All studies included had Newcastle-Ottawa Scale NOS scores greater than 6, indicating good methodological quality (Table 1). The information collected from the studies encompassed the first author and publication date of each article, the number and age of the patients, the presence or absence of prior ^{177}Lu treatment history, the disease stage of the patients, the baseline PSA levels, the Gleason score, and the Eastern Cooperative Oncology Group (ECOG) score (Table 2). Additionally, information pertaining to the radioligand therapy was recorded, such as the ^{225}Ac compound used, the dosage, the duration, and the time intervals between successive administrations (Table 3). Outcome measures for the studies included biochemical and molecular response rates, survival periods, treatment-related deaths, clinical responses, and toxicity reactions. Biochemical response was evaluated according to the criteria defined by the Prostate

Cancer Clinical Trials Working Group 3 (PCWG3) [34], where PSA response was defined as a decrease in PSA levels by more than 50% from baseline, while any level of PSA decrease was recorded. Patients underwent ^{68}Ga-PSMA PET/CT imaging, and molecular response was assessed according to PERCIST 1.0 criteria [35], combining complete response (CR) and partial response (PR) into molecular response rate. Survival periods included PFS and OS, with PFS defined as the time from the first dose of ^{225}Ac-PSMA-RLT to the first evidence of progression or death, or the end of the study period, and OS defined as the time from the first dose of ^{225}Ac-PSMA-RLT to death from any cause. Clinical responses were evaluated using clinical response criteria such as visual analogue score, pain score, Karnofsky Performance Status (KPS), and ECOG criteria. Adverse events and toxicities were recorded and graded according to the Common Terminology Criteria for Adverse Events version 5.0 (CTCAE5.0) [36] (Tables 3-5).

Meta-analysis results

Meta-analysis of any PSA decline rate

A total of 14 relevant studies on single-agent ^{225}Ac-PSMA RLT in mCRPC patients were included, comprising 1005 patients, with 973 patients being evaluated, among whom 781 patients experienced a decline in PSA levels. Significant heterogeneity (I^2=79.4%, P<0.001) was present, thus subgroup analysis (using two groups, 1: representing studies where less than 50% of patients had a history of ^{177}Lu treatment, 2: representing studies where more than 50% of patients had a history of ^{177}Lu treatment) and a random-effects model were used for meta-analysis of the rate of PSA decline. The forest plot suggested that the combined rate of any degree of PSA decline after treatment with ^{225}Ac-PSMA-617/I&T (Figure 2) was 0.85 (95% CI: 0.80-0.91). In studies where fewer than 50% of patients had received prior ^{177}Lu treatment, the pooled response rate was 0.87 (95% CI: 0.80-0.93); in those with more than 50% prior ^{177}Lu treatment, the rate was 0.83 (95% CI: 0.74-0.91).

Meta-analysis of PSA decline rate >50%

A total of 14 relevant studies on single-agent ^{225}Ac-PSMA RLT in mCRPC patients were included, comprising 1005 patients, with 973 patients being evaluated, and 619 (63.6%) achieved a >50% decline in PSA levels. Significant heterogeneity (I^2=85.3%, P<0.001) was present, thus subgroup analysis (using two groups, 1: representing studies where less than 50%

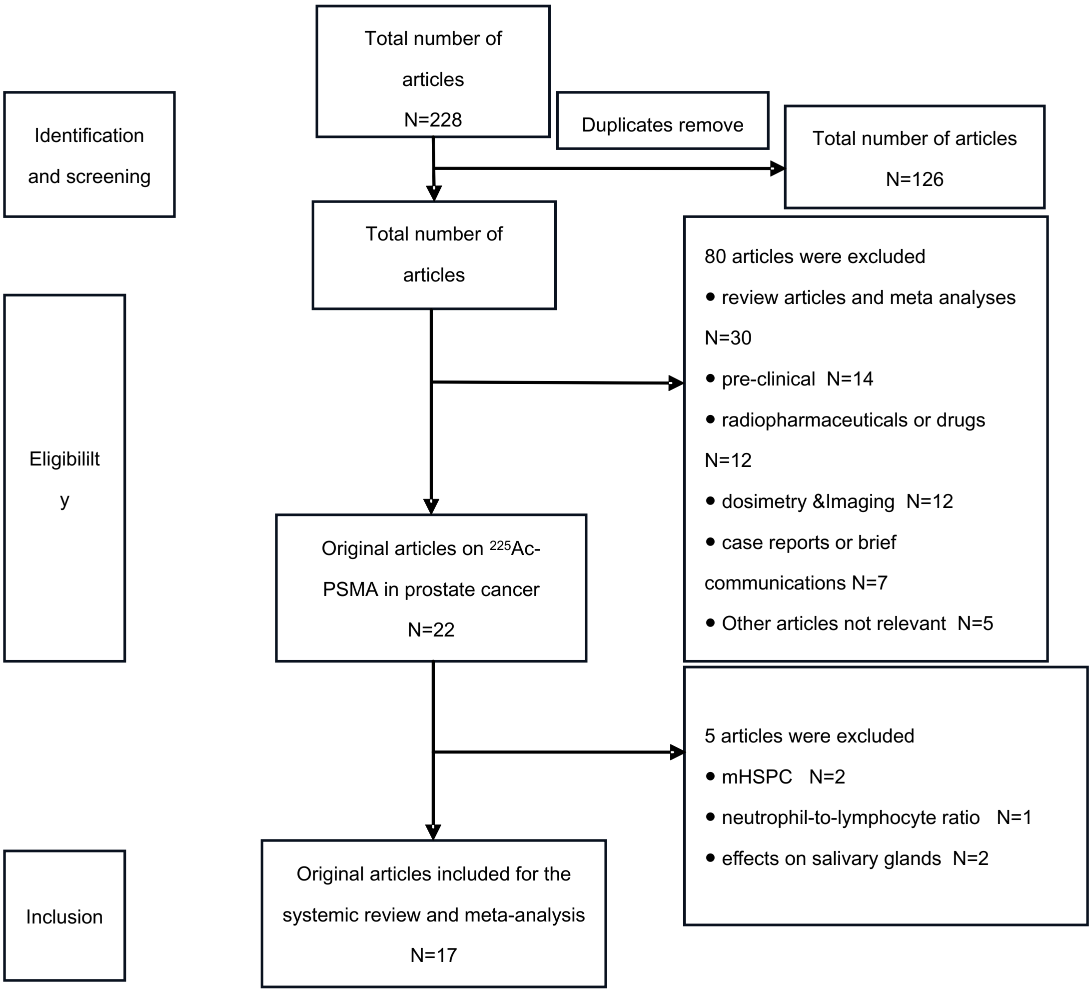

Figure 1. Flowchart of literature screening.

Table 1. *Quality assessment of the included studies based on the Newcastle-Ottawa.*

NO.	Author and year	Selection	Comparability	Outcome	Score
1	Kratochwil et al., 2018 (17)	3	1	3	7
2	Sathekge et al., 2019 (18)	3	1	3	7
3	Khreish et al., 2020 (19)	3	1	3	7
4	Sathekge et al., 2020 (20)	3	1	3	7
5	Satapathy et al., 2020 (21)	3	1	2	6
6	Yadav et al., 2020 (22)	3	1	3	7
7	van der Doelen et al., 2021 (23)	3	1	3	7
8	Zacherl et al., 2021 (24)	3	1	2	6
9	Feuerecker et al., 2021 (25)	2	1	3	6
10	Sen Ishita et al., 2021 (26)	3	1	3	7
11	Rosar et al., 2021 (27)	3	1	3	7
12	Sanli et al., 2021 (28)	2	1	3	6
13	Lawal et al., 2022 (29)	3	1	3	7
14	Sathekge et al., 2022 (30)	3	1	3	7
15	Ballal et al., 2023 (31)	3	1	3	7
16	Selcuk et al., 2023 (32)	2	1	3	6
17	Sathekge et al., 2024 (33)	3	1	3	7

of patients had a history of ^{177}Lu treatment, 2: representing studies where more than 50% of patients had a history of ^{177}Lu treatment) and a random-effects model were used for the meta-analysis of the rate of PSA decline >50%. The forest plot suggested that the combined rate of PSA decline >50% after treatment with ^{225}Ac-PSMA RLT (Figure 3) was 0.66 (95% CI: 0.58-0.75). In studies with <50% of patients previously treated with ^{177}Lu, the response rate was 0.71 (95% CI: 0.61-0.81), while in studies with >50% prior ^{177}Lu treatment, the rate was 0.51 (95% CI: 0.39–0.64).

Meta-analysis of overall survival (OS)

Overall survival was evaluated in a total of 806 patients in a total of 7 studies on the use of ^{225}Ac-PSMA RLT in the treatment of mCRPC. Since significant heterogeneity was present (I^2=81.3%, P<0.001), a random-effects model was employed for the combined analysis of OS. The forest plot (Figure 4) showed a pooled median OS of 13.79 months (95% CI: 11.11-16.48 months).

Meta-analysis of progression-free survival (PFS)

PFS was evaluated in 834 patients across 8 studies investigating ^{225}Ac-PSMA RLT for the treatment of mCRPC. Since significant heterogeneity was present (I^2=86.8%, P<0.001), a random-effects model was used for the combined analysis of PFS. The forest plot (Figure 5) showed a pooled median PFS of 9.67 months (95% CI: 6.99-12.35 months).

Molecular response

Molecular responses were evaluated by gallium-68 (^{68}Ga)-PSMA PET/CT in 111 of 123 patients across 5 studies evaluating ^{225}Ac-PSMA RLT in the treatment of mCRPC. Molecular responses were observed in 72 patients. Since significant heterogeneity was present (I^2=69.3%, P=0.011), a random-effects model was used to combine the molecular response rates. Meta-analysis showed a pooled molecular response rate of 0.71 (95% CI: 0.56 to 0.87), as shown in Figure 6.

Adverse reactions

Among the 17 studies analyzed, 15 studies examined the adverse events of single-agent ^{225}Ac-PSMA-RLT according to the Common Terminology Criteria for Adverse Events version 5.0 (CTCAE 5.0). The most common adverse event was xerostomia (dry mouth), occurring in 63.5% (638/1005) of

Table 2. *Basic characteristics of the studies included.*

Author and year	Patients (N)	Age (yr) (median and/or range)	Prior ^{177}Lu treatment (%)	Study population	Baseline PSA (ng/mL) (median and/or range)	GS	ECOG
Kratochwil et al., 2018 (17)	40	70	0%	mCRPC	169	NR	0-1 (80%) ≥2 (20%)
Sathekge et al., 2019 (18)	17	64.5 (45-82)	18%	mCRPC	33.84 (1.2-1300.69)	9 (6-10)	0-1 (88%) ≥2 (12%)
Khreish et al., 2020 (19)	20	72 (57-88)	20%	mCRPC	215 (6-5547)	NR	0-1 (60%) ≥2 (40%)
Sathekge et al., 2020 (20)	73	69 (45-85)	14%	mCRPC	57.2	8 (6-10)	0-1 (82%) 2-3 (18%)
Satapathy et al., 2020 (21)	11	68 (57–81)	46%	mCRPC	158 (35-840)	8 (7-9)	0-1 (64%) 2 (36%)
Yadav et al., 2020 (22)	28	69.7 (46-87)	54%	mCRPC	222.2 (47-443.2)	≤7 (21%) ≥8 (79%)	≤2 (28%) ≥3 (72%)
van der Doelen et al., 2021 (23)	13	71 (64-77)	15%	mCRPC	878 (203-1611)	≤7 (54%) ≥8 (46%)	0 (23%) 1-2 (77%)
Zacherl et al., 2021 (24)	14	75 (64-88)	79%	mCRPC	112 (20.5-818)	NR	0-1 (79%） 2 (21%)
Feuerecker et al., 2021 (25)	26	72.5 (63–75.8)	100%	mCRPC	331 (142–682)	8 (7-9)	≤2 (100%)
Sen Ishita et al., 2021 (26)	38	68 (53-84)	24%	mCRPC	NR	≤7 (10%) ≥8 (90%)	0-2 (100%)
Rosar et al., 2021 (27)	17	69.4(57-89)	100%	mCRPC	152(5.9-2570)	NR	0-1 (94%) ≥2 (6%)
Sanli et al., 2021 (28)	12	70 (45-89)	58%	mCRPC	129 (10.7-765)	9 (6-10)	0-1 (50%) ≥2 (50%)
Lawal et al., 2022 (29)	106	NR (44-86)	7%	mCRPC	250.2 (2.8-4494.0)	8 (6-10)	NR
Sathekge et al., 2022 (30)	53	63.4 (45-83)	0%	mCRPC	466 (102-4405)	NR	0-1 (79%) ≥2 (21%)
Ballal et al., 2023 (31)	63	67 (39-87)	43%	mCRPC	NR	≤7 (11%) ≥8 (89%)	3 (1-4)
Selcuk et al., 2023 (32)	23	70.3 (61.5-79.1)	100%	mCRPC	103.79 (0.349–727.8)	NR	NR
Sathekge et al., 2024 (33)	488	68·1 (59.3-76.9)	32%	mCRPC	169·5 (34·6–519·8)	NR	0-1 (65%) ≥2 (28%)

NR, not reported; mCRPC, metastatic castration-resistant prostate cancer; PSA,prostate-specific antigen; ECOG, Eastern Cooperative Oncology Group; GS, Gleason score.

Table 3. *Treatment characteristics of the studies included.*

Author and year	Patients analyzed for PSA decline (N)	RLT agent	Dose	Number of cycles (median and/or range)	Follow-up (wk)	Any PSA decline (n/N (%))	PSA decline >50% (n/N (%))
Kratochwil et al., 2018 (17)	38	^{225}Ac-PSMA-617	100KBq/kg BW	1-3	8	33/38 (87%)	24/38 (63%)
Sathekge et al., 2019 (18)	17	^{225}Ac-PSMA-617	7.4±1.5MBq/cycle	2-6	8	16/17 (94%)	15/17 (88%)
Khreish et al., 2020 (19)	20	^{225}Ac-PSMA-617/^{177}Lu-PSMA-617 tandem therapy	^{225}Ac-PSMA-617: 5.3 (1.5-7.9) MBq/cycle, 177Lu-PSMA-617: 6.9 (5.0-11.6) GBq/cycle	1 (0-5)	NR	18/20 (90%)	13/20 (65%)
Sathekge et al., 2020 (20)	73	^{225}Ac-PSMA-617	4-8MBq/cycle	3 (1-8)	8	60/73 (83%)	51/73 (70%)
Satapathy et al., 2020 (21)	11	^{225}Ac-PSMA-617	100KBq/kg BW	2 (1-4)	8-12	8/11 (73%)	5/11 (46%)
Yadav et al., 2020 (22)	28	^{225}Ac-PSMA-617	100KBq/kg BW	3 (1-7)	8	22/28 (79%)	11/28 (39%)
van der Doelen et al., 2021 (23)	13	^{225}Ac-PSMA-617	6-8MBq/cycle	3 (1-4)	8	11/13 (85%)	9/13 (69%)
Zacherl et al., 2021 (24)	14	^{225}Ac-PSMA-I&T	7.8 (6.0-8.5) MBq/cycle	1-5	8	11/14 (79%)	7/14 (50%)
Feuerecker et al., 2021 (25)	26	^{225}Ac-PSMA-617	9MBq/cycle	2 (1-6)	8	23/26 (88%)	17/26 (65%)

(continued)

Sen Ishita et al., 2021 (26)	38	^{225}Ac-PSMA-617	100KBq/kg BW	2 (2-5)	8	33/38 (87%)	25/38 (66%)
Rosar et al., 2021 (27)	17	^{225}Ac-PSMA-617/^{177}Lu-PSMA-617 tandem therapy	^{225}Ac-PSMA-617: 1.8-6.9 MBq/cycle, ^{177}Lu-PSMA-617: 3.8-8.2GBq/cycle	1	NR	10/17 (59%)	5/17 (29%)
Sanli et al., 2021 (28)	12	^{225}Ac-PSMA-617	7.4 (5.9-9.9) MBq/cycle	2 (1-3)	8	9/12 (75%)	6/12 (50%)
Lawal et al., 2022 (29)	106	^{225}Ac-PSMA-617	100KBq/kg BW	4 (1-9)	NR	95/106 (90%)	85/106 (80%)
Sathekge et al., 2022 (30)	53	^{225}Ac-PSMA-617	4-8MBq/cycle	3 (1-7)	8	51/53 (96%)	48/53 (91%)
Ballal et al., 2023 (31)	63	^{225}Ac-PSMA-617	100-150KBq/kg	3-9	8	51/56 (91%)	38/56 (68%)
Selcuk et al., 2023 (32)	23	^{225}Ac-PSMA-RLT	7.6 (6.2-10)/cycle	13 (8-28)	4.5 (2-9)	NR	NR
Sathekge et al., 2024 (33)	488	^{225}Ac-PSMA-RLT	8MBq/cycle	2 (2-4)	8	358/488 (73%)	278/488 (57%)

NR, not reported; BW, body weight; PSA, prostate specific antigen.

Table 4. Outcome measurements in the studies included.

Author and year	Patients (N)	Molecular response (n/N (%))	OS (months) (median and/or range)	PFS (months) (median and/or range)	Treatment related deaths, (n/N (%))	Post-therapy clinical response parameters
Kratochwil et al., 2018 (17)	40	NR	>12.0 (NR)	7.0 (NR)	NR	NR
Sathekge et al., 2019 (18)	17	15/17 (88%)	NR	NR	NR	NR
Khreish et al., 2020 (19)	20	10/20 (50%)	48 (4-92)	19 (12-26)	NR	NR
Sathekge et al., 2020 (20)	73	NR	18 (16.2-19.9)	15.2 (13.1-17.4)	NR	NR
Satapathy et al., 2020 (21)	11	NR	NR	NR	3/11 (27%)	NR
Yadav et al., 2020 (22)	28	12/22 (55%)	17 (16-NR)	12 (9-13)	NR	VAS max: 4.7 (0 - 9) Analgesic score: 2 (0-3) KPS: 75.5 (40-90) ECOG: 2 (0-4)
van der Doelen et al., 2021 (23)	13	6/7 (86%)	8.5 (NR)	5.5(NR)	NR	NR
Zacherl et al., 2021 (24)	14	NR	NR	NR	NR	NR
Feuerecker et al., 2021 (25)	26	NR	7 (4.5–12.1)	3.5 (1.8–11.2)	NR	VAS: 25 (0-90)

(continued)

Sen Ishita et al., 2021 (26)	38	17/38 (45%)	12 (9.1-14.9)	8 (5.3-10.6)	NR	NR
Rosar et al., 2021 (27)	17	5/17 (29%)	NR	3.7 (3.0-4.4)	NR	NR
Sanli et al., 2021 (28)	12	9/12 (75%)	10 (1-24)	4 (1-20)	NR	NR
Lawal et al., 2022 (29)	106	NR	15 (12.8-17.2)	14 (8.15-19.86)	NR	NR
Sathekge et al., 2022 (30)	53	30/53 (57%)	>55 (NR)	22 (NR)	NR	NR
Ballal et al., 2023 (31)	63	NR	15 (10-19)	9 (7-15)	NR	VAS: 5 (0-10) Analgesic score: 2 (0-3) KPS: 70 (40-90) ECOG: 2 (0-4)
Selcuk et al., 2023 (32)	23	NR	7.7 (NR)	3.1 (NR)	NR	NR
Sathekge et al., 2024 (33)	488	NR	15.5 (13.4-18.3)	7.9 (6.8-8.9)	0/488 (0%)	NR

NR, not reported; OS, overall survival; PFS, progression-free survival; VAS: Visual analgesic score; KPS: Karnofsky Performance Status.

Table 5. Treatment-related toxicity of the studies included.

Author and year	Patients (N)	Hematological toxicity (n/N)		Nephrotoxicity (n/N)		Xerostomia (n/N)		Other side effects (n/N)
		Any grade	Grade≥3	Any grade	Grade≥3	Any grade	Grade≥3	
Kratochwil et al., 2018 (17)	40	NR	NR	NR	NR	19/40	NR	NR
Sathekge et al., 2019 (18)	17	NR	NR	1/17	1/17	17/17	0/17	NR
Khreish et al., 2020 (19)	20	① NR ② NR ③ NR	3/20 2/20 2/20	NR	0/20	13/20	0/20	nausea 1/20, fatigue 5/20, anorexia 4/20
Sathekge et al., 2020 (20)	73	① 27/73 ② 9/73 ③ 7/73	5/73 2/73 1/73	23/73	5/73	62/73	0/73	nausea 15/73, anorexia 23/73, constipation 19/73 fatigue 37/73, weight loss 28/73, hypoalbuminemia 14/73, dysuria 13/73, xerophthalmia 4/73
Satapathy et al., 2020 (21)	11	① 8/11 ② 5/11 ③ 5/11	1/11 0/11 2/11	1/11	1/11	8/11	1/11	nausea 2/11, constipation 2/11, fatigue 3/11, weight loss 2/11, anorexia 3/11

(continued)

Yadav et al., 2020 (22)	28	① 28/28 ② 11/28 ③ 4/28	1/28 0/28 0/28	4/28	0/28	8/28	0/28	fatigue 15/28
van der Doelen et al., 2021 (23)	13	① 0/13 ② 0/13 ③ 0/13	0/13 0/13 0/13	0/13	0/13	13/13	0/13	NR
Zacherl et al., 2021 (24)	14	① 14/14 ② 5/14 ③ 6/14	3/14 1/14 0/14	2/14	0/14	5/14	0/14	dysgeusia 6/14, anorexia 9/14, nausea 5/14, fatigue 12/14, weightloss 4/14
Feuerecker et al., 2021 (25)	26	① 15/26 ② 13/26 ③ 14/26	9/26 7/26 5/26	5/26	0/26	26/26	0/26	fatigue 12/26, Weight loss 3/26, anorexia 8/26
Sen Ishita et al., 2021 (26)	38	① 11/38 ② 6/38 ③ 4/38	0/38 0/38 3/38	NR	NR	37/38	5/38	weight loss 21/38, hearing loss 2/38 nausea 9/38
Rosar et al., 2021 (27)	17	① 17/17 ② 5/17 ③ 3/17	0/17 0/17 1/17	7/17	0/17	5/17	0/17	NR
Sanli et al., 2021 (28)	12	① 11/12 ② 2/12 ③ 3/12	0/12 0/12 1/12	2/12	0/12	12/12	0/12	NR

(continued)

Lawal et al., 2022 (29)	106	① 43/106 ② 40/106 ③ 33/106	1/106 3/106 3/106	NR	NR	NR	NR	NR
Sathekge et al., 2022 (30)	53	① 8/53 ② 5/53 ③ 5/53	1/53 1/53 0/53	10/53	3/53	43/53	0/53	NR
Ballal et al., 2023 (31)	63	① 52/56 ② 12/56 ③ 9/56	2/56 3/56 0/56	2/56	1/56	18/56	0/56	fatigue 41/56, nausea 7/56, vomiting 7/56, gstritis 15/56, anorexia 24/56, myalgia 21/56, constipation 13/56, ascites with pleural effusion 1/56
Selcuk et al., 2023 (32)	23	NR	NR	NR	NR	23/23	NR	NR
Sathekge et al., 2024 (33)	488	① 329/488 ② 198/488 ③ 230/488	64/488 19/488 32/488	272/488	22/488	347/488	NR	NR

① anemia; ② leucopenia; ③ thrombocytopenia; NR, not reported.

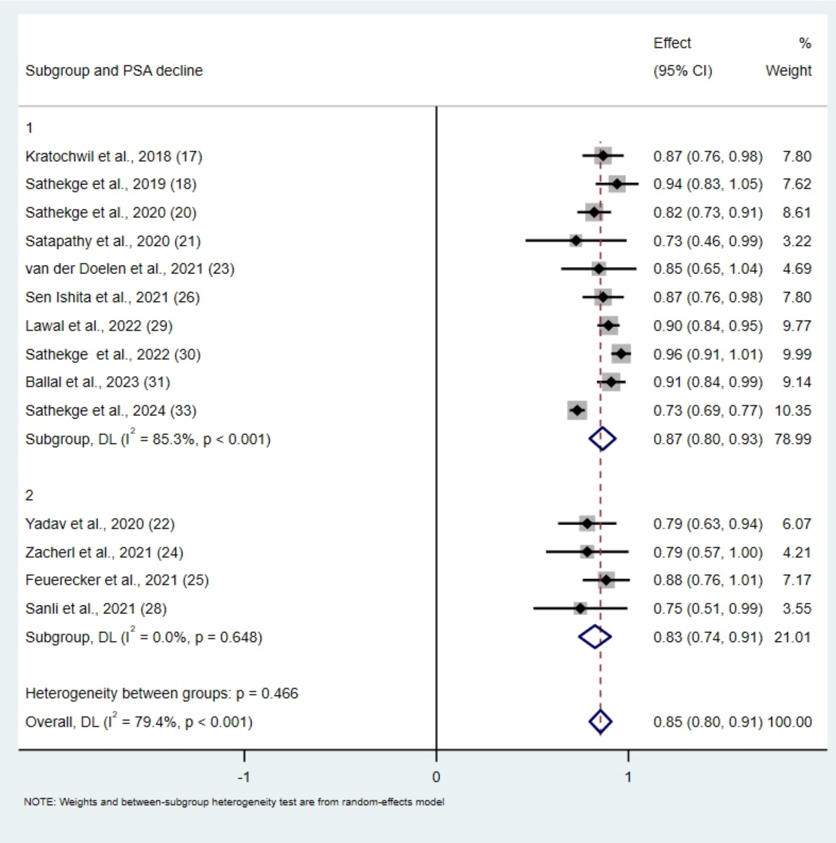

Figure 2. Forest plot for PSA decline after treatment.

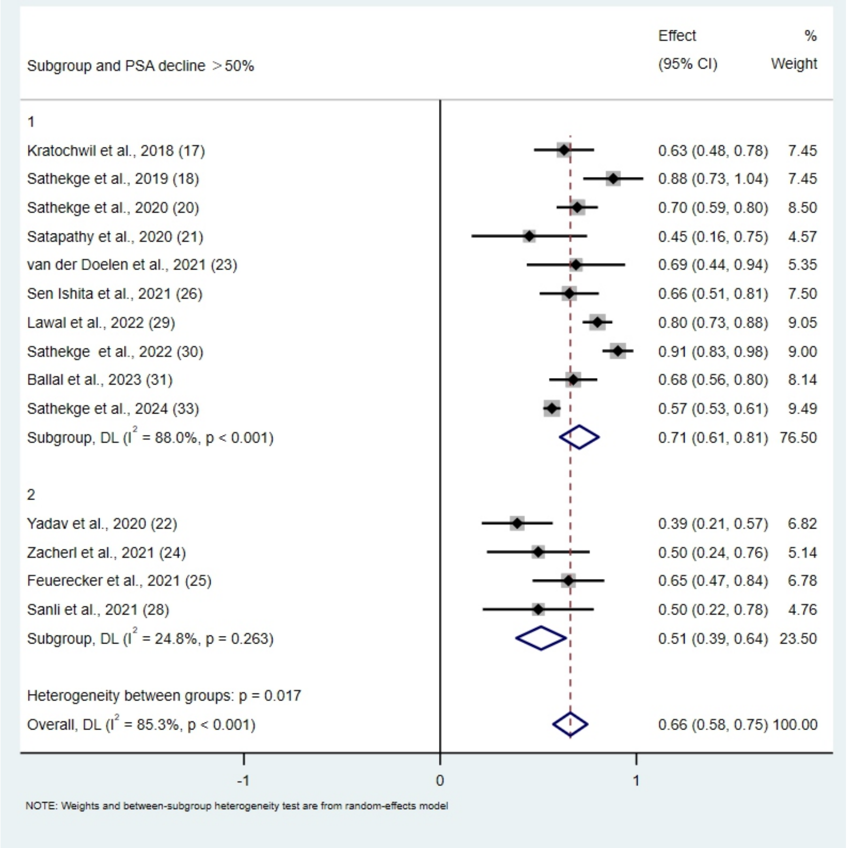

Figure 3. Forest plot for >50% PSA decline after treatment.

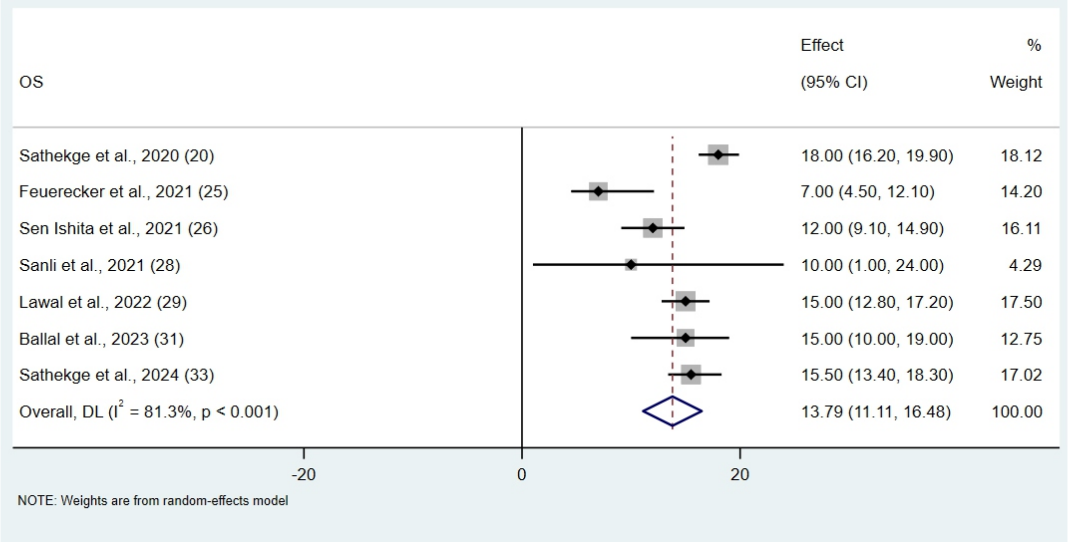

Figure 4. Forest plot for overall survival.

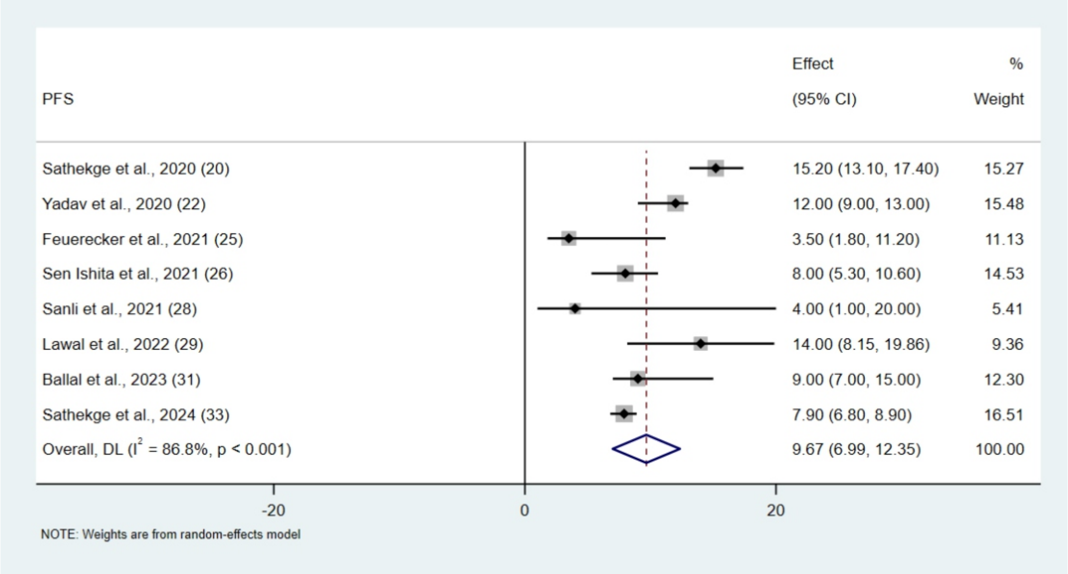

Figure 5. Forest plot for progression-free survival.

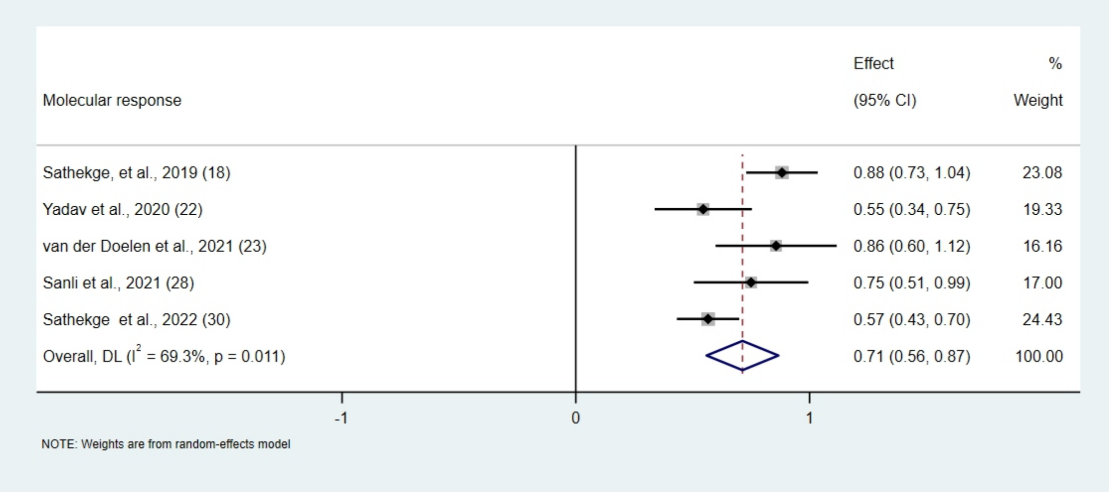

Figure 6. Forest plot for molecular response.

individuals at any grade, with only 0.6% (6/1005) experiencing grade III or higher xerostomia. The second most common event was anemia, affecting 54.3% (546/1005), with grade III or higher anemia observed in 8.7% (87/1005). Leukopenia occurred in 30.4% (306/1005), with grade III or higher leukopenia seen in 3.6% (36/1005), while thrombocytopenia affected 31.8% (320/1005), with grade III or higher thrombocytopenia observed in 4.7% (47/1005). Renal toxicity was reported in 32.0% (322/1005), with grade III or higher renal toxicity observed in 3.3% (33/1005). Other adverse events included fatigue (11.9% [120/1005]), anorexia (6.7% [67/1005]), weight loss (5.8% [58/1005]), constipation (3.4% [34/1005]), and nausea (3.8% [38/1005]). Furthermore, some studies have reported rare adverse reactions, such as urinary difficulty, dry eyes, vomiting, muscle pain, etc. Treatment-related deaths were reported in only one study, with three out of eleven patients experiencing treatment-related deaths.

A total of 9 studies reported anemia. After excluding data that could not be analyzed, we applied a random-effects model and subgroup analysis based on previous standards. The final forest plot indicated an incidence of anemia of 0.59 (95% CI: 0.41-0.76). A total of 11 studies reported leucopenia and thrombocytopenia, with the final forest plot showing incidences of 0.28 (95% CI: 0.18-0.38) for leukopenia and 0.26 (95% CI: 0.14-0.38) for thrombocytopenia. Furthermore, in studies where over 50% of patients received ^{177}Lu treatment, the incidences of leukopenia and thrombocytopenia were higher, at 0.36 (95% CI: 0.22-0.50) and 0.33 (95% CI: 0.13-0.54), respectively. A total of 10 studies reported renal toxicity, with an incidence of 0.19 (95% CI: 0.02-0.36). Finally, 9 studies reported xerostomia, with an incidence of 0.62 (95% CI: 0.48-0.77). The forest plots about adverse events are shown in Figures 7-11.

Discussion

This systematic review and meta-analysis of 17 studies comprehensively evaluated the efficacy and safety of ^{225}Ac-PSMA RLT in mCRPC. Our analysis indicates that ^{225}Ac-PSMA RLT is effective with limited adverse reactions in mCRPC patients. Approximately 85% of patients experienced a decrease in PSA levels following treatment, with around 66% of patients experiencing a decrease of over 50%. The average PFS and OS were 9.67 and 13.79 months, respectively. This conclusion is undoubtedly promising for patients with advanced prostate cancer who have failed other treatment modalities. Xerostomia was the most prominent side effect in ^{177}Lu/^{225}Ac-PSMA RLT for prostate cancer [37], with 63.5% of patients in our study experiencing xerostomia, mostly at grade II or below and

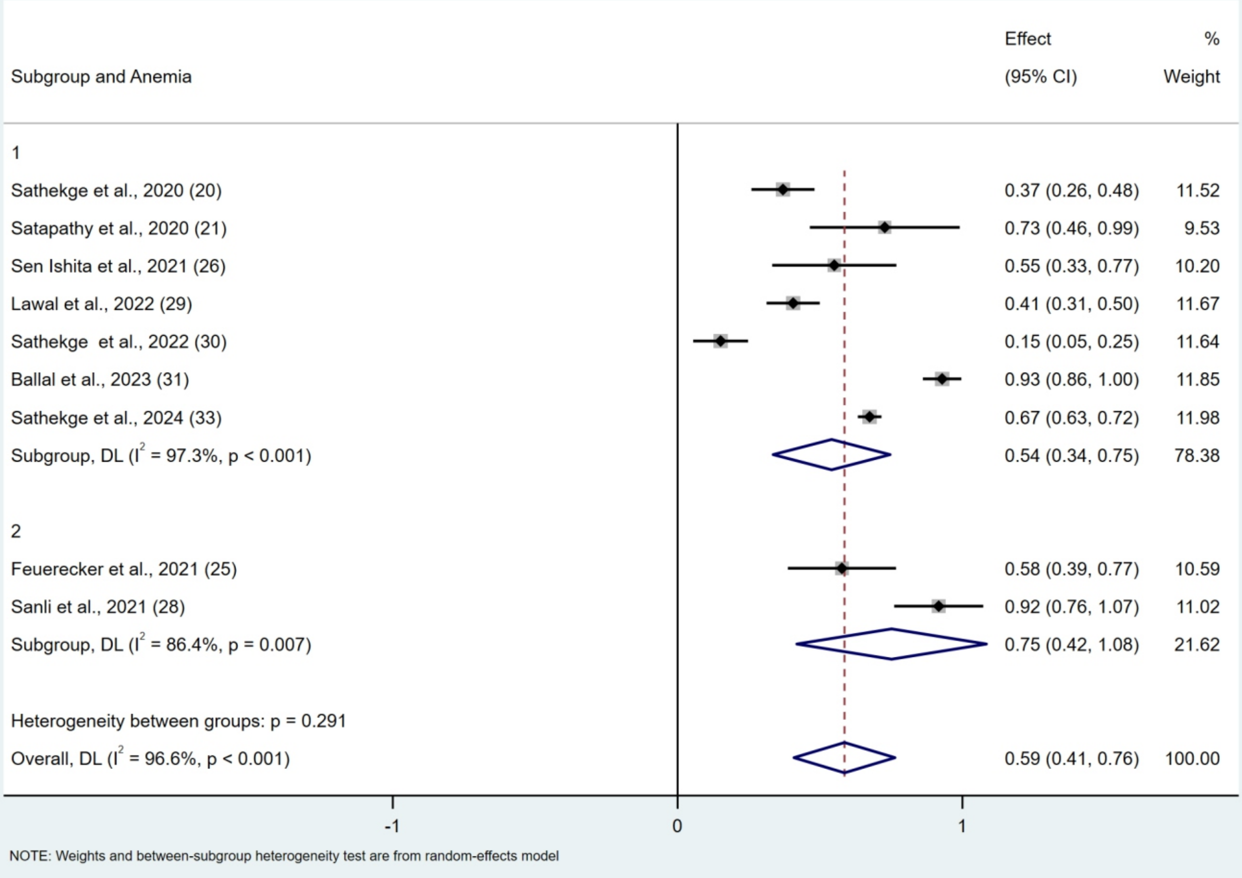

Figure 7. Forest plot for anemia.

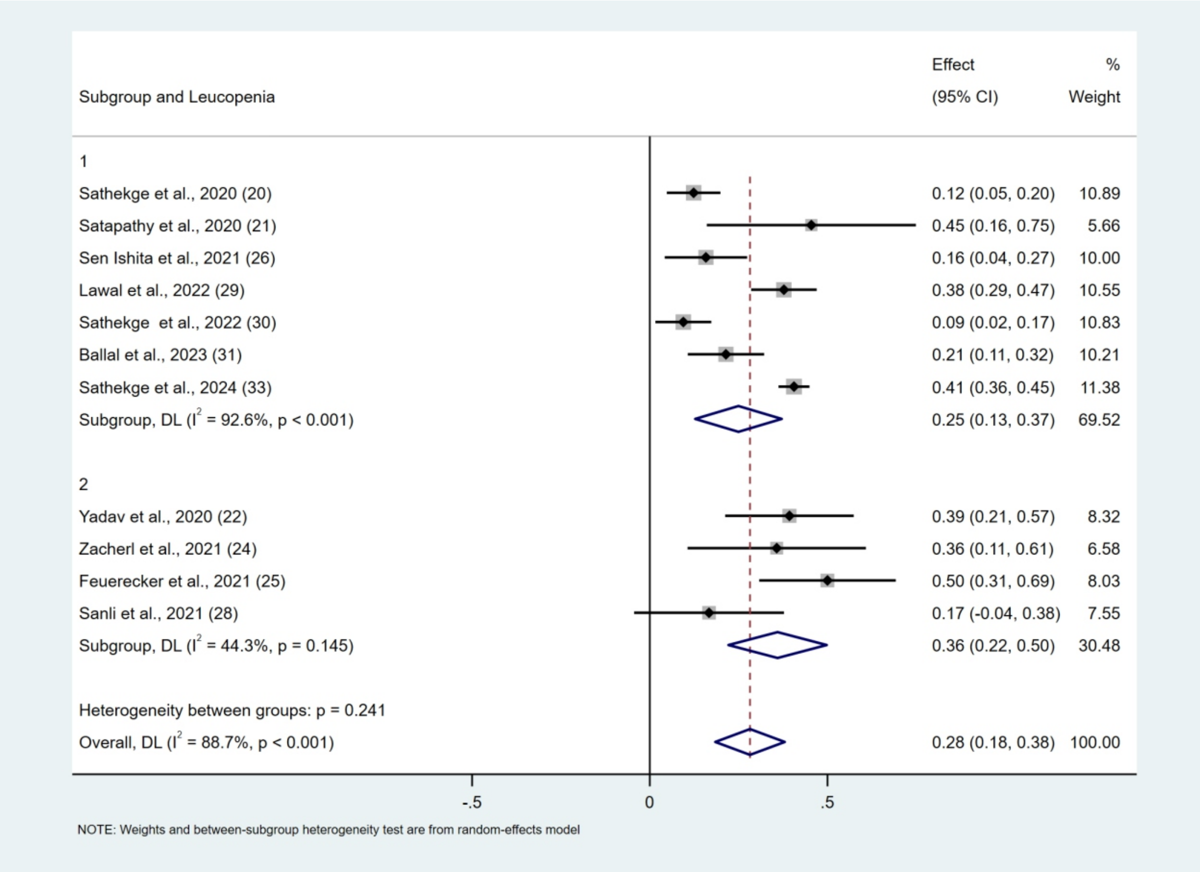

Figure 8. Forest plot for leucopenia.

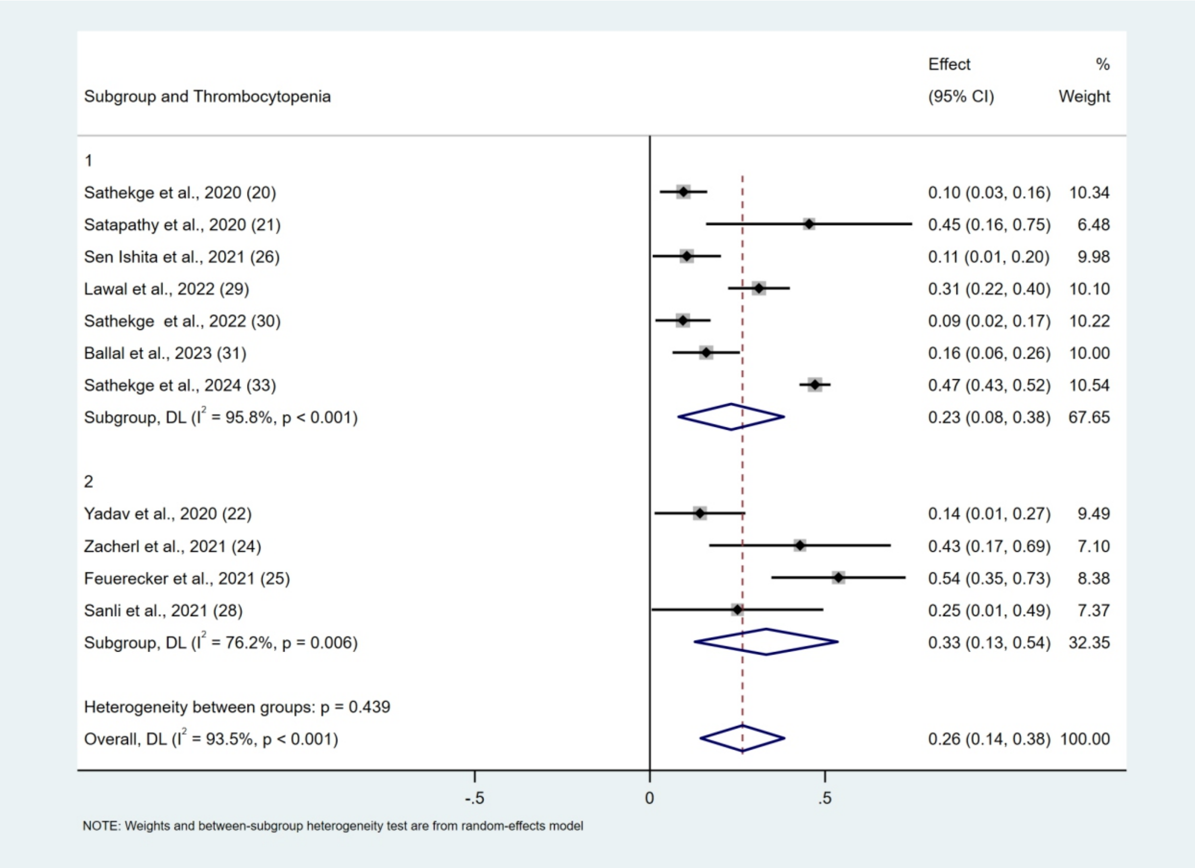

Figure 9. Forest plot for thrombocytopenia.

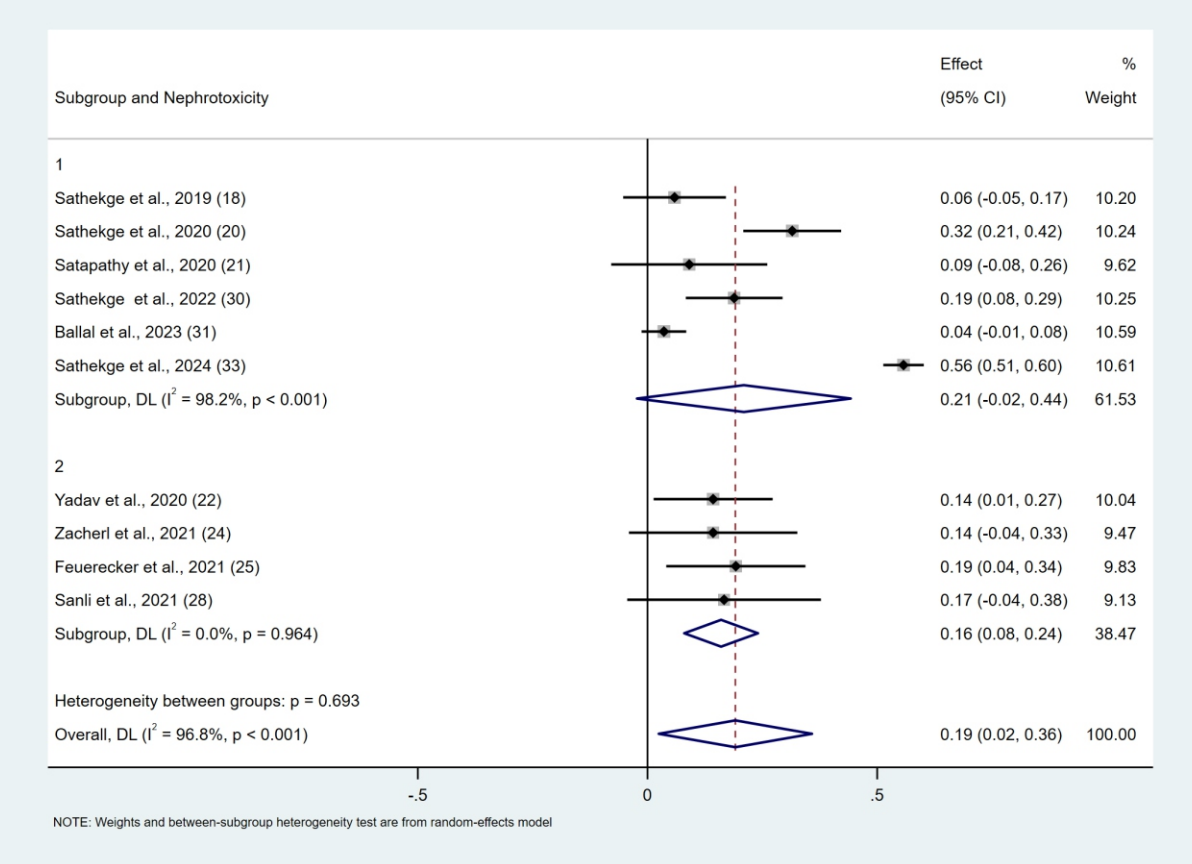

Figure 10. Forest plot for nephrotoxicity.

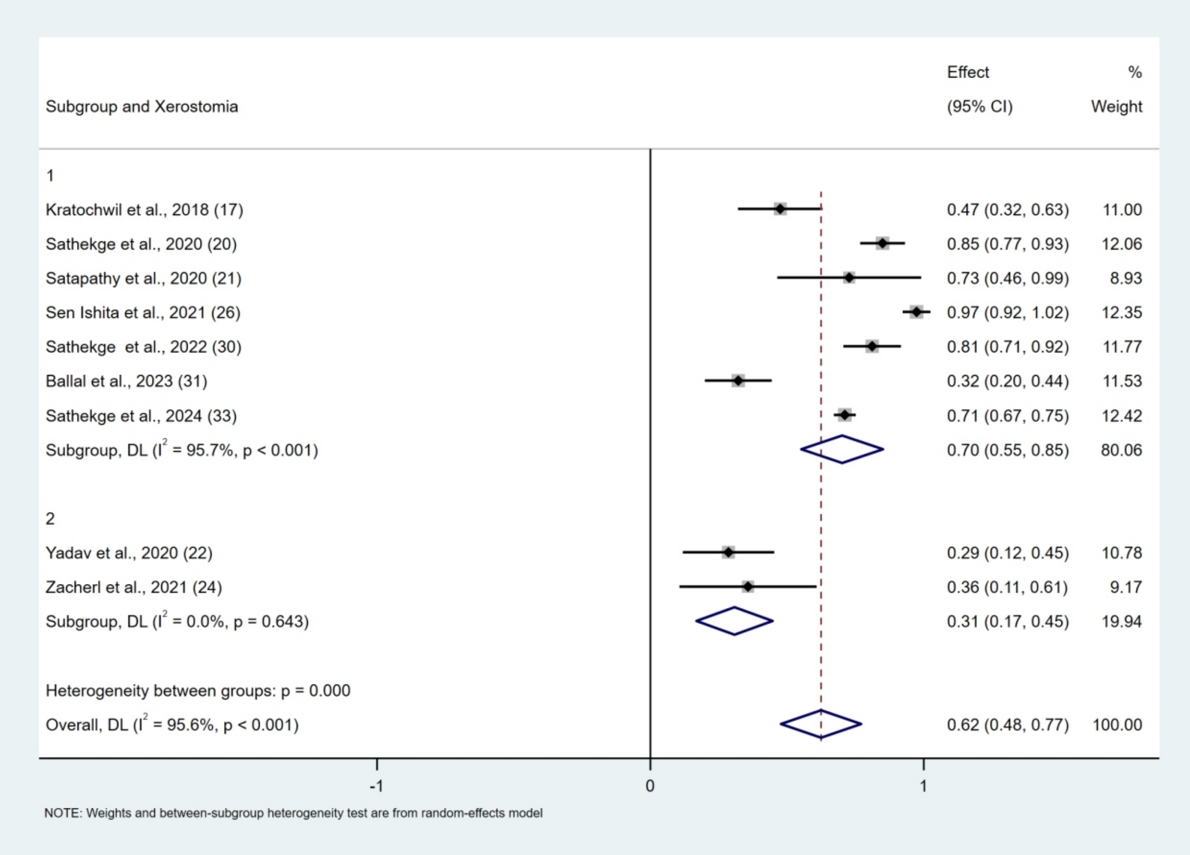

Figure 11. Forest plot for xerostomia.

and transient. The presence of severe xerostomia, hematologic toxicity, and renal toxicity in only a minority of patients suggests that this treatment modality is a viable option for mCRPC patients. Severe xerostomia may contribute to treatment discontinuation in some patients. Hence, some studies have explored methods to reduce salivary gland uptake, such as adding cold PSMA-11 [38] or substituting Glu in alternative pharmacophores [39].

Due to the potential influence of prior ^{177}Lu treatment on treatment outcomes [40], we conducted subgroup analyses to determine whether more than 50% of patients in the included studies had received ^{177}Lu treatment. Our analysis revealed a lower proportion of patients experiencing >50% PSA decrease in studies where more than 50% of patients had received ^{177}Lu treatment. Therefore, we speculate that prior ^{177}Lu treatment may impact the efficacy of targeted alpha therapy with ^{225}Ac. However, due to the limited number of studies included, we cannot confirm the validity of this hypothesis nor its potential impact on OS and PFS. Thus, more clinical research is needed to explore this issue further.

Furthermore, in our systematic review, we included two studies [19, 27] in which mCRPC patients were given ^{225}Ac-PSMA-617 and ^{177}Lu-PSMA-617 in the same cycle. One study [19] indicated that 90% of patients experienced a reduction in PSA to some extent, with a PFS of 19 months and an OS of 48 months. Sixty-five percent of patients experienced xerostomia. However, another study [27] showed only 59% of patients experiencing any level of PSA reduction, and a PFS of only 3.7 months. Anemia, leukopenia, thrombocytopenia, nephrotoxicity, and xerostomia appeared in 100%, 29%, 17%, 41%, and 29% of patients, respectively. As mentioned earlier, in single-agent ^{225}Ac treatment, the overall incidence of PSA reduction at any level is 85%, with PFS and OS values of 9.7 months and 13.8 months, respectively. The overall incidence of adverse reactions is as follows: anemia 59%, leukopenia 28%, thrombocytopenia 26%, nephrotoxicity 19%, and xerostomia 62%. Therefore, the results of these two studies taken together are not yet conclusive about efficacy and safety of concurrent ^{177}Lu/^{225}Ac therapy compared with single-agent ^{225}Ac therapy. Hence, further research is needed to explore the potential value of concurrent ^{177}Lu/^{255}Ac therapy in the treatment of mCRPC.

However, several limitations of the present study should be acknowledged. While we included one recent large-sample study, the majority of studies were small-sample and predominantly single-arm retrospective observational studies, which are associated with a higher risk of bias. Additionally, these studies had short follow-up periods, limiting the analysis of patient survival, and there were few studies assessing OS, PFS, and comprehensive molecular response. Consequently, the data available for synthesis were limited. Furthermore, not all studies reported all adverse reactions; some only reported one or a few specific adverse reactions. When analyzing the results, we assumed that if a study did not report a certain adverse reaction, it meant that the reaction did not occur in that study. However, this assumption may lead to an underestimation of the incidence of adverse reactions associated with ^{225}Ac-PSMA RLT, as it cannot be ruled out that some adverse reactions occurred in certain studies but were not reported. Lastly, there was heterogeneity across trials in terms of study design, inclusion of other diseases, prostate cancer progression, previous treatment modalities, and PSMA expression levels. Therefore, evaluating the efficacy and safety of ^{225}Ac-PSMA RLT still requires high-quality, multicenter, prospective, randomized controlled trials.

In conclusion, the treatment of mCRPC patients with ^{225}Ac-PSMA RLT appears to be a safe and effective option, demonstrating a relatively low incidence of treatment-related toxicities. Given these findings, it may serve as a promising therapeutic strategy for mCRPC patients who have progressed after other late-stage treatments. Furthermore, prior exposure to ^{177}Lu-PSMA therapy may influence PSA response rates in subsequent ^{225}Ac-PSMA treatment; however, additional high-quality clinical trials are needed to clarify its impact and underlying mechanisms.

Funding

This work was partially supported by Southwest Medical University (Funding No.2024ZKY046) and Luzhou Municipal People's Government (Funding No.070254).

Bibliography

1. Siegel RL, Miller KD, Wagle NS et al. Cancer statistics, 2023. *CA Cancer J Clin* 2023; 73: 17-48.
2. Zhu Y, Mo M, Wei Y et al. Epidemiology and genomics of prostate cancer in Asian men. *Nat Rev Urol* 2021; 18: 282-301.
3. Liu Z, Jiang Y, Fang Q et al. Future of cancer incidence in Shanghai, China: Predicting the burden upon the ageing population. *Cancer Epidemiol* 2019; 60: 8-15.
4. Parker C, Castro E, Fizazi K et al. Prostate cancer: ESMO Clinical Practice Guidelines for diagnosis, treatment and follow-up. *Ann Oncol* 2020; 31: 1119-34.
5. Sekhoacha M, Riet K, Motloung P et al. Prostate Cancer Review: Genetics, Diagnosis, Treatment Options, and Alternative Approaches. *Molecules* 2022; 27: 5730.
6. Teo MY, Rathkopf DE, Kantoff P. Treatment of Advanced Prostate Cancer. *Annu Rev Med* 2019; 70: 479-99.
7. Gourdin T. Recent progress in treating advanced prostate cancer. *Curr Opin Oncol* 2020; 32: 210-5.
8. Kessel A, Kohli M, Swami U. Current management of metastatic castration-sensitive prostate cancer. *Cancer Treat Res Commun* 2021; 28: 100384.
9. Achard V, Putora PM, Omlin A et al. Metastatic Prostate Cancer: Treatment Options. *Oncology* 2022; 100: 48-59.
10. Mansinho A, Macedo D, Fernandes I et al. Castration-Resistant Prostate Cancer: Mechanisms, Targets and Treatment. *Adv Exp Med Biol* 2018; 1096: 117-33.
11. Jang A, Kendi AT, Sartor O. Status of PSMA-targeted radioligand therapy in prostate cancer: current data and future trials. *Ther Adv Med Oncol* 2023; 15: 17588359231157632.
12. Wang F, Li Z, Feng X et al. Advances in PSMA-targeted therapy for prostate cancer. *Prostate Cancer Prostatic Dis* 2022; 25: 11-26.
13. Morgenstern A, Apostolidis C, Kratochwil C et al. An Overview of Targeted Alpha Therapy with ^{225}Actinium and ^{213}Bismuth. *Curr Radiopharm* 2018; 11: 200-8.
14. Alam MR, Singh SB, Thapaliya S et al. A Review of ^{177}Lutetium-PSMA and ^{225}Actinium-PSMA as Emerging Theranostic Agents in Prostate Cancer. *Cureus* 2022; 14: e29369.
15. Dhiman D, Vatsa R, Sood A. Challenges and opportunities in developingActinium-225 radiopharmaceuticals. *Nucl Med Commun* 2022; 43: 970-7.
16. Page MJ, McKenzie JE, Bossuyt PM et al. The PRISMA 2020 statement: an updated guideline for reporting systematic reviews. *BMJ* 2021; 372: n71.

17. Kratochwil C, Bruchertseifer F, Rathke H et al. Targeted α-Therapy of Metastatic Castration-Resistant Prostate Cancer with ^{225}Ac-PSMA-617: Swimmer-Plot Analysis Suggests Efficacy Regarding Duration of Tumor Control. *J Nucl Med* 2018; 59: 795-802.
18. Sathekge M, Bruchertseifer F, Knoesen O et al. ^{225}Ac-PSMA-617 in chemotherapy-naive patients with advanced prostate cancer: a pilot study. *Eur J Nucl Med Mol Imaging* 2019; 46: 129-38.
19. Khreish F, Ebert N, Ries M et al. ^{225}Ac-PSMA-617/^{177}Lu-PSMA-617 tandem therapy of metastatic castration-resistant prostate cancer: pilot experience. *Eur J Nucl Med Mol Imaging* 2020; 47: 721-8.
20. Sathekge M, Bruchertseifer F, Vorster M et al. Predictors of Overall and Disease-Free Survival in Metastatic Castration-Resistant Prostate Cancer Patients Receiving ^{225}Ac-PSMA-617 Radioligand Therapy. *J Nucl Med* 2020; 61: 62-9.
21. Satapathy S, Mittal BR, Sood A et al. Health-Related Quality-of-Life Outcomes with Actinium-225-Prostate-Specific Membrane Antigen-617 Therapy in Patients with Heavily Pretreated Metastatic Castration-Resistant Prostate Cancer. *Indian J Nucl Med* 2020; 35: 299-304.
22. Yadav MP, Ballal S, Sahoo RK et al. Efficacy and safety of ^{225}Ac-PSMA-617 targeted alpha therapy in metastatic castration-resistant Prostate Cancer Patients. *Theranostics* 2020; 10: 9364-77.
23. van der Doelen MJ, Mehra N, van Oort IM et al. Clinical outcomes and molecular profiling of advanced metastatic castration-resistant prostate cancer patients treated with ^{225}Ac-PSMA-617 targeted alpha-radiation therapy. *Urol Oncol* 2021; 39: 729.e7-729.e16.
24. Zacherl MJ, Gildehaus FJ, Mittlmeier L et al. First Clinical Results for PSMA-Targeted α-Therapy Using ^{225}Ac-PSMA-I&T in Advanced-mCRPC Patients. *J Nucl Med* 2021; 62: 669-74.
25. Feuerecker B, Tauber R, Knorr K et al. Activity and Adverse Events of Actinium-225-PSMA-617 in Advanced Metastatic Castration-resistant Prostate Cancer After Failure of Lutetium-177-PSMA. *Eur Urol* 2021; 79: 343-50.
26. Sen I, Thakral P, Tiwari P et al. Therapeutic efficacy of ^{225}Ac-PSMA-617 targeted alpha therapy in patients of metastatic castrate resistant prostate cancer after taxane-based chemotherapy. *Ann Nucl Med* 2021; 35: 794-810.
27. Rosar F, Hau F, Bartholomä M et al. Molecular imaging and biochemical response assessment after a single cycle of ^{225}Ac-PSMA-617/^{177}Lu-PSMA-617 tandem therapy in mCRPC patients who have progressed on ^{177}Lu-PSMA-617 monotherapy. *Theranostics* 2021; 11: 4050-60.
28. Sanli Y, Kuyumcu S, Simsek DH et al. ^{225}Ac-Prostate-Specific Membrane Antigen Therapy for Castration-Resistant Prostate Cancer: A Single-Center Experience. *Clin Nucl Med* 2021; 46: 943-51.
29. Lawal IO, Morgenstern A, Vorster M et al. Hematologic toxicity profile and efficacy of ^{225}Ac-PSMA-617 α-radioligand therapy of patients with extensive skeletal metastases of castration-resistant prostate cancer. *Eur J Nucl Med Mol Imaging* 2022; 49: 3581-92.
30. Sathekge M, Bruchertseifer F, Vorster M et al. mCRPC Patients Receiving ^{225}Ac-PSMA-617 Therapy in the Post-Androgen Deprivation Therapy Setting: Response to Treatment and Survival Analysis. *J Nucl Med* 2022; 63: 1496-502.
31. Ballal S, Yadav MP, Satapathy S et al. Long-term survival outcomes of salvage ^{225}Ac-PSMA-617 targeted alpha therapy in patients with PSMA-expressing end-stage metastatic castration-resistant prostate cancer: a real-world study. *Eur J Nucl Med Mol Imaging* 2023; 50: 3777-89.
32. Alan-Selcuk N, Beydagi G, Demirci E et al. Clinical Experience with ^{225}Ac-PSMA Treatment in Patients with ^{177}Lu-PSMA-Refractory Metastatic Castration-Resistant Prostate Cancer. *J Nucl Med* 2023; 64: 1574-80.
33. Sathekge MM, Lawal IO, Bal C et al. Actinium-225-PSMA radioligand therapy of metastatic castration-resistant prostate cancer (WARMTH Act): a multicentre, retrospective study. *Lancet Oncol* 2024; 25: 175-83.
34. Scher HI, Morris MJ, Stadler WM et al. Trial Design and Objectives for Castration-Resistant Prostate Cancer: Updated Recommendations From the Prostate Cancer Clinical Trials Working Group 3. *J Clin Oncol* 2016; 34: 1402-18.
35. Wahl RL, Jacene H, Kasamon Y et al. From RECIST to PERCIST: Evolving Considerations for PET response criteria in solid tumors. *J Nucl Med* 2009; 50: 122S-50S.
36. Freites-Martinez A, Santana N, Arias-Santiago S et al. Using the Common Terminology Criteria for Adverse Events (CTCAE - Version 5.0) to Evaluate the Severity of Adverse Events of Anticancer Therapies. *Actas Dermosifiliogr (Engl Ed)* 2021; 112: 90-2.
37. Langbein T, Kulkarni HR, Schuchardt C et al. Salivary Gland Toxicity of PSMA-Targeted Radioligand Therapy with ^{177}Lu-PSMA and Combined ^{225}Ac- and ^{177}Lu-Labeled PSMA Ligands (TANDEM-PRLT) in Advanced Prostate Cancer: A Single-Center Systematic Investigation. *Diagnostics (Basel)* 2022; 12: 1926.
38. Kalidindi TM, Lee SG, Jou K et al. A simple strategy to reduce the salivary gland and kidney uptake of PSMA-targeting small molecule radiopharmaceuticals. *Eur J Nucl Med Mol Imaging* 2021; 48: 2642-51.
39. Kuo HT, Lin KS, Zhang Z et al. What a difference a methylene makes: replacing Glu with Asp or Aad in the Lys-urea-Glu pharmacophore of PSMA-targeting radioligands to reduce kidney and salivary gland uptake. *Theranostics* 2022; 12: 6179-88.
40. Stangl-Kremser J, Ricaurte-Fajardo A, Subramanian K et al. Response to RL-^{225}Ac in prostate cancer: Effect of prior treatment with RL-^{177}Lu: A systematic review of the literature. *Prostate* 2023; 83: 901-11.

Comparative insights into mild cognitive impairment: A clinical case study with ^{18}F-FDG and amyloid PET imaging

Shiv Patil[1,2] MS,
Eric M Teichner[1,2] BA,
Robert C Subtirelu[1] MSc,
Arjun B Ashok[2] MD,
Talha Khan[1] BA,
Alexander Gerlach[1] BA,
Raj Patel[1],
Lancelot Herpin[1] BA,
Moein Moradpour[1] MD,
Thomas Werner[1] MSE,
Andrew Newberg[3,4] MD,
Mona Elisabeth-Revheim[5] MD, PhD,
Abass Alavi[1] MD

1. Department of Radiology, University of Pennsylvania, Philadelphia, PA, USA
2. Sidney Kimmel Medical College, Thomas Jefferson University, Philadelphia, PA, USA
3. Marcus Institute of Integrative Health, Thomas Jefferson University, Philadelphia, PA, USA
4. Department of Radiology, Thomas Jefferson University, Philadelphia, PA, USA
5. Institute of Clinical Medicine, Faculty of Medicine, University of Oslo, Oslo, Norway

Keywords: Mild cognitive impairment - Dementia - ^{18}F-FDG amyloid - PET

Corresponding author:
Abass Alavi MD, PhD
Department of Radiology,
University of Pennsylvania,
Philadelphia, PA 19104 USA
Telephone: 215-662-3069
E-mail: abass.alavi@uphs.upenn.edu

Received:
5 Jun 2025
Accepted revised:
30 Jun 2025

Abstract

Early detection of mild cognitive impairment (MCI) is crucial for initiating therapeutic interventions that may slow or prevent further cognitive deterioration. Mild cognitive impairment represents a transitional phase between normal cognitive aging and more severe forms of dementia, such as Alzheimer's disease (AD). Positron emission tomography (PET) can provide insight into the pathophysiology and progression of neurodegenerative processes associated with dementia and MCI using either fluorine-18 (^{18}F)-florbetapir, which detects beta-amyloid plaque burden, or ^{18}F-fluorodeoxyglucose (^{18}F-FDG), which measures glucose metabolism. However, there are limited comparative studies using the two radiotracers to quantify cognitive decline. This case study presents an 83-year-old female with a clinical diagnosis of MCI and a mini-mental state examination (MMSE) score of 26, at the lower boundary for normal cognitive function; she was assessed with PET/computed tomography (CT) using both radiotracers. Although global assessments did not reveal significant abnormalities, localized findings showed hypometabolism in key brain regions, such as the posterior cingulate cortex, and beta-amyloid plaque accumulation in the anterior cingulate cortex. These results highlight the limitations of conventional cognitive assessments, like the MMSE, and underscore the potential value of PET imaging as a complementary diagnostic tool. The study supports the role of ^{18}F-FDG as a stronger indicator of cognitive impairment due to its correlation with cognitive scores, while recognizing the need for further research to evaluate the predictive value of both PET tracers in early MCI detection and their potential to improve diagnostic accuracy.

Hell J Nucl Med 2025; 28(2): 168-172

Introduction

The identification of clinically significant cognitive decline in its early stages is increasingly recognized as vital. Simply distinguishing between dementia and the natural cognitive changes associated with aging is insufficient for detecting the onset of cognitive disorders. The clinical evaluation of patients with potential Alzheimer's disease (AD) now extends beyond dementia to include mild cognitive impairment (MCI), which represents a transitional phase from the expected cognitive decline of aging to severe forms of dementia. Mild cognitive impairment is particularly significant because it offers an opportunity for early intervention with therapeutic strategies that may slow or prevent further cognitive deterioration [1, 2]. Studies on MCI have highlighted specific brain regions with reduced metabolism, such as the frontal-medial areas, including the precentral gyrus and pars triangularis. This hypometabolism, especially in medial components, may be associated with progressive supranuclear palsy (PSP), making these regions focal points for understanding MCI pathology [3].

Molecular imaging with positron emission tomography (PET) has enabled the diagnosis and characterization of neurodegenerative processes associated with dementia and MCI. For instance, fluorine-18 (^{18}F)-florbetapir is a radiotracer used to detect beta-amyloid plaques [4]. Concurrently, ^{18}F-fluorodeoxyglucose (^{18}F-FDG) measures glucose metabolism, reflecting functional activity in brain regions and thereby aiding in the assessment of neurodegenerative disorders like MCI. Although both tracers can provide insights into the pathophysiology and progression of MCI, there is a notable lack of literature comparing the two modalities. This gap highlights the need for thorough research to identify the best approach for evaluating and diagnosing MCI [5].

Regional brain changes are increasingly considered crucial biomarkers for cognitive impairment progression in MCI, pinpointing the specific neurological areas impacted by the condition [3]. This case report details a patient whose ^{18}F-FDG PET scans show statistically significant hypometabolism in critical regions [6]. The patient's mini-mental state examination (MMSE) scores, which are essential for monitoring MCI progression, correlate with the observed regional metabolic variations [7]. The standardized uptake volume (SUV) values are notably higher than those typically predicted for someone within this MMSE score range. This discrepancy emphasizes the complexity of MCI and the necessity for more sophisticated diagnostic tools [8]. The present report provides a case that challenges traditional diagnostic parameters and underscores the potential of radiotracer imaging to improve our understanding of MCI and its clinical manifestations.

Case Report

An 83-year-old female with a clinical diagnosis of MCI and a MMSE score of 26 was selected from a trial approved by the Thomas Jefferson University Institutional Review Board. The MMSE scores range from 0 to 30, indicating severe dementia to normal cognitive function respectively [7]. This particular patient was included in the study because her risk factors for MCI, such as having a body mass index (BMI) of 27kg/m^2 - which classifies her as overweight - correlate with an increased risk of cognitive decline [9].

The diagnosis of MCI in this patient was based upon the following criteria [10]:

1. A self-reported complaint of memory or cognitive decline, which was corroborated by an informant.
2. A clinical dementia rating (CDR) global score of 0.5, indicating a level of decline not categorizable as dementia [11].
3. Objective evidence of cognitive impairment or marginally normal cognition with a documented history of higher cognitive performance.
4. Absence of any obvious neurological or medical cause for the cognitive impairment, such as encephalopathy, nephropathy, head trauma, or stroke.
5. Normal activities of daily living.

Upon enrollment, the patient underwent a thorough evaluation that included brain computed tomography (CT) scans and PET scans with both ^{18}F-florbetapir and ^{18}F-FDG. All imaging procedures were performed after the patient had fasted overnight for at least eight hours, ensuring that blood glucose concentrations were below 8mmol/L.

Low-dose CT imaging was conducted to provide attenuation correction and anatomical context. The parameters for the CT scan were 140kV, with a current of 30-110mA, a noise index of 25, a rotation time of 0.8 seconds, and a slice thickness of 3.75mm. The reliability and accuracy of the neuroimaging data were verified by correcting the scans for scatter, attenuation, and dead time.

The ^{18}F-FDG PET scan protocol was aligned with the Alzheimer's disease neuroimaging initiative [12]. Participants received an injection of approximately 185MBq (5mCi) of ^{18}F-FDG. Imaging commenced around 30 minutes post-administration, with a total acquisition time of 30 minutes. A subsequent transmission scan was conducted for attenuation correction.

The ^{18}F-florbetapir PET scans adhered to established protocols [13]. A dose of approximately 370MBq (10mCi) of ^{18}F-florbetapir was administered to the subjects, with the scan starting around 50 minutes after injection. The acquisition time for the ^{18}F-florbetapir PET scan was 10 minutes, which was also followed by a transmission scan for attenuation correction.

Analysis

Analysis of the regional brain uptake of both ^{18}F-florbetapir and ^{18}F-FDG was performed using MIMneuro version 7.1.5 (MIM Software, Inc., Cleveland, Ohio). The analysis utilized validated methods. Positron emission tomography data were mapped on a voxel-by-voxel basis to a standardized brain template designed for comparison against an integrated anatomical brain atlas, which includes predefined regions of interest (ROI). For the ^{18}F-FDG workflow, MIMneuro analyzed 70 predefined regions (Figure 1), and for the florbetapir analysis, 16 predefined regions were assessed (Figure 2). Following this mapping, the software exported cross-sectional z-scores for each predefined ROI. These z-scores represent the number of standard deviations a patient's ^{18}F-FDG uptake or amyloid burden is from the control group's mean value, utilizing age-matched normal controls as a benchmark. Additionally, the mean standardized uptake value (SUVmean) was calculated by the software to quantify the overall metabolic activity and global amyloid burden. The employment of MIMneuro for this rigorous analytical process facilitated the precise quantification of regional metabolic uptake in the brain.

Results and Discussion

This case report presents an 83-year-old female clinically diagnosed with MCI who was included in our study due to preexisting risk factors for cognitive decline. The global brain assessment with ^{18}F-florbetapir (SUVmean=0.59) and ^{18}F-FDG PET/CT (SUVmean=3.83) did not reveal a significant presence of beta-amyloid plaques or global hypometabolism, respectively. However, localized imaging identified several brain regions with a substantial presence of either beta-amyloid plaques or hypometabolism. Moreover, the patient's MMSE score of 26 places her at the lower boundary of the normal cognition range (26-30). The disparity between the imaging findings, the clinical diagnosis of MCI, and the MMSE score underscores the limitations of the MMSE and the necessity for more sophisticated diagnostic tools to complement the existing techniques for evaluating MCI.

While the MMSE is known for its specificity in diagnosing dementia, it lacks the sensitivity to effectively distinguish between normal cognition, MCI, and dementia [14]. Mini-mental state examination scores can be influenced by confounding variables such as the patient's age or educational level; for instance, a study reported that individuals with a me-

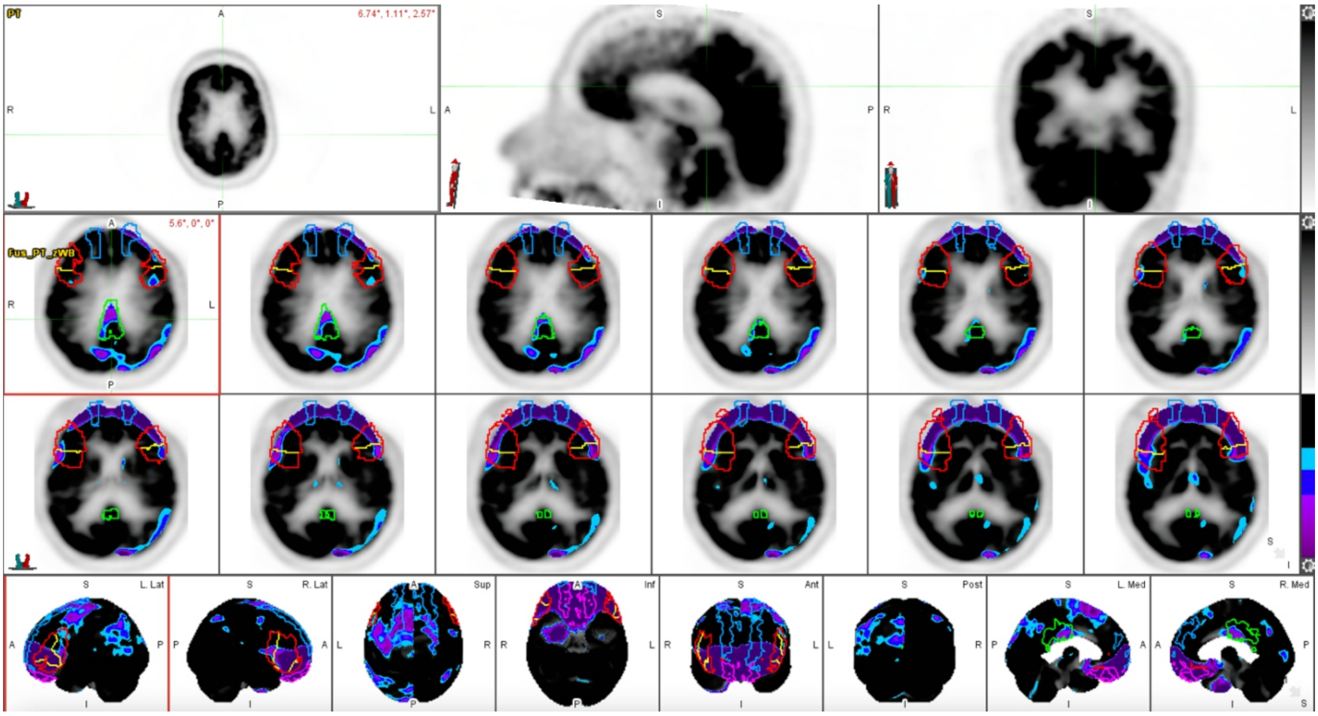

Figure 4. Evaluation of ^{18}F-FDG PET through quantitative analysis using MIMneuro version 7.1.5 (MIM Software, Inc., Cleveland, OH, USA). Low ^{18}F-FDG uptake is represented by purple and blue contours. The medial orbital gyrus (pink), and inferior frontal gyrus (red), inferior frontal gyrus, pars orbitalis (light blue), inferior frontal gyrus, pars triangularis (yellow), superior frontal gyrus (blue), and posterior cingulate gyrus (green) have been delineated as regions of interest in this patient.

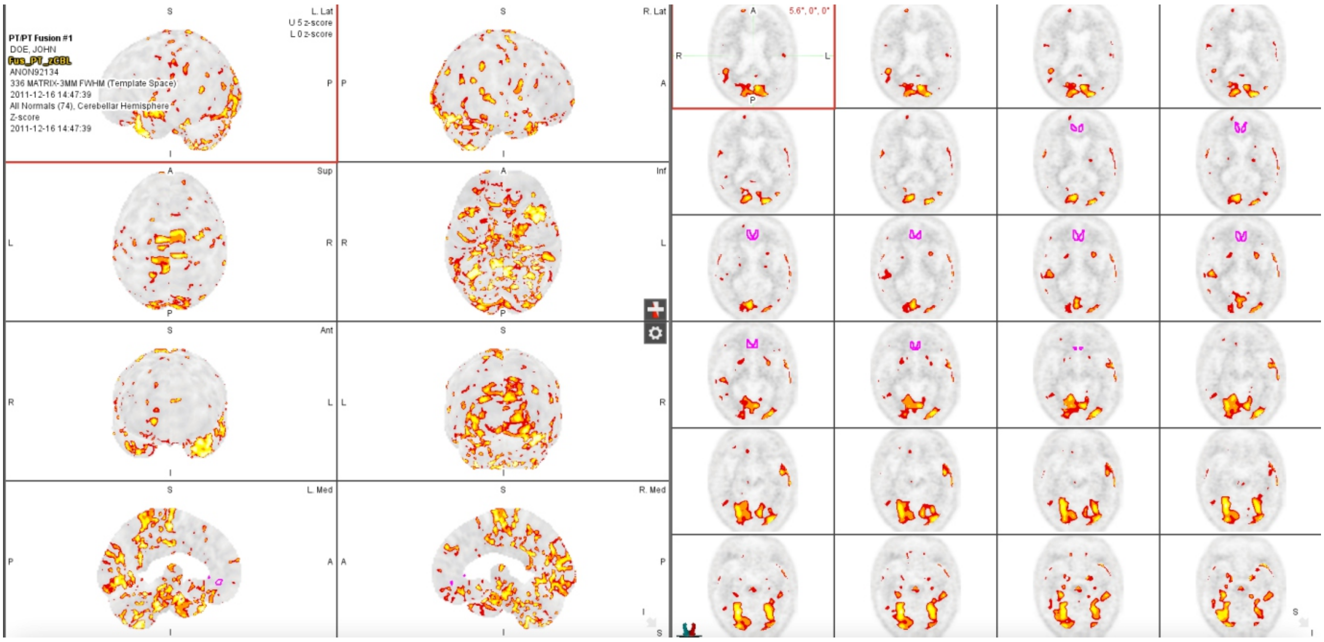

Figure 5. Evaluation of ^{18}F-florbetapir through quantitative analysis using MIMneuro version 7.1.5 (MIM Software, Inc., Cleveland, OH, USA). Increased ^{18}F-florbetapir uptake is represented by yellow and red contours. The anterior cingulate gyrus (pink) has been delineated as a region of interest in this patient.

dian age of 70 and over seven years of education had a median MMSE score of 29, in contrast to a median score of 23 among those with the same median age but only three years of education [14]. This study also indicated that the AB cognitive screen (ABCS) was less affected by patient-related factors and offered better clinical utility [14]. Jia et al. (2021) found that the Montreal cognitive assessment (MoCA) was more sensitive for detecting MCI than the MMSE, suggesting that MoCA is a superior measure of cognitive function [15]. Zhuang et al. (2021) recommend employing a combination of sensitive cognitive assessment tools for initial MCI screening and highly specific tools for secondary screening, excluding the MMSE from their recommendations [16]. However, these cognitive assessments rely on subjective interpretation and can be influenced by various external factors within the healthcare delivery process. Our patient's normal MMSE score, despite imaging and clinical evidence of cognitive decline, accentuates the potential value of objective data from PET imaging to aid in the evaluation and diagnosis of MCI.

A key area of interest showing hypometabolism is the posterior cingulate gyrus (z= -3.17) within the posterior cingulate cortex (PCC), which is crucial for early AD identification [17]. The PCC is involved in episodic memory tasks, including autobiographical memory, future imagination, spatial navigation, and scene processing [17]. Impairment in these areas is a hallmark of AD and can indicate MCI depending on the severity. Posterior cingulate cortex hypometabolism is one of the earliest markers in AD and serves as an indicator of the progression from MCI to AD [18-23]. Fluorine-18-FDG PET studies suggest that hypometabolism in the PCC is highly prevalent among amnestic MCI cases [3, 23, 24].

Other regions exhibiting hypometabolism are the superior frontal gyrus (SFG) (z= -3.95), middle frontal gyrus (MiFG) (z= -2), and inferior frontal gyrus (IFG) (z= -5.56). The SFG is associated with working memory and higher cognitive functions, while the MiFG is believed to play a significant role in numeracy and literacy. The IFG is implicated in speech processing and response inhibition [25]. Hypometabolism in the IFG sub-regions, pars orbitalis (z= -9.87), and pars triangularis (z= -5.73), can contribute to the symptoms of MCI, such as memory loss and word-finding difficulties. These findings align with various studies identifying these regions as susceptible to metabolic changes in MCI [26-28]. Specifically, the IFG was highlighted as a strong predictor for AD development in MCI patients carrying the APOE genotype [29]. Notably, hypometabolism in the anterior cingulate cortex (ACC) is commonly observed in MCI cases but was not present in this patient (z= 0.34) [26-28, 30, 31]. However, ^{18}F-florbetapir PET imaging indicated a significant accumulation of beta-amyloid plaques in the ACC (z=2.14), a finding aligned with studies differentiating healthy controls from AD subjects using ^{18}F-florbetapir SUV which were significantly higher in the AD group (P= 0.003) with respect to the ACC [30].

Despite existing studies on how ^{18}F-FDG and amyloid PET tracers evaluate MCI, research comparing the two types of radiotracers remains scarce. A recent study [32] demonstrated that both ^{18}F-florbetapir and ^{18}F-FDG could effectively distinguish MCI and AD subjects from normal controls but were less effective at differentiating between MCI and AD subjects. Fluorine-18-FDG was found to be a more potent indicator of cognitive impairment due to its stronger correlation with MMSE scores compared to ^{18}F-florbetapir. Although limited, our case findings support these observations. As indicated by prior research [17-28], regions of interest in cognitive impairment include the precuneus, ACC, PCC, inferior parietal lobe, superior/middle temporal gyrus, SFG, MiFG, and IFG. Hypometabolism measured by ^{18}F-FDG was identified in four of the nine regions. Fluorine-18-florbetapir imaging analyzed only five of the nine regions of interest, with a significant presence of beta-amyloid plaques observed in only one. It is noteworthy that no regions showed overlap in significant hypometabolism or beta-amyloid plaque presence. Amyloid PET tracers have higher sensitivity but relatively lower specificity compared to ^{18}F-FDG PET [32]. However, the presence of amyloid plaques in healthy individuals [33] has been reported, indicating that amyloid presence alone is insufficient for an AD diagnosis.

There is a wealth of literature on the predictive value of ^{18}F-FDG PET for dementia development and the transition from MCI to AD. However, research on ^{18}F-FDG PET ability to predict the progression from normal cognition to MCI is limited. Early detection of MCI is critical as it is associated with an increased risk of progressing to dementia. Early identification allows for timely support, monitoring of disease progression, and an earlier diagnosis of dementia. In the future, this could facilitate the initiation of preventive treatments to slow the progression to dementia. In the case of the MCI patient observed, hypometabolic regions such as the PCC, SFG, MiFG, and IFG were noted, mirroring patterns seen in other MCI and dementia cases. The ACC, another region of interest, showed high levels of beta-amyloid plaques. Further research is needed to determine whether the metabolic patterns observed and the presence of amyloid plaques in these regions are reliable indicators of the transition from normal cognition to MCI.

The study is limited by the small number of regions assessed with ^{18}F-florbetapir and the lack of baseline brain region observations from when the patient had normal cognitive function before developing MCI. Future studies, particularly longitudinal studies, should compare the diagnostic and prognostic utility of ^{18}F-FDG and ^{18}F-florbetapir PET to evaluate their effectiveness in assessing disease severity and progression.

In conclusion, global and regional analysis of ^{18}F-FDG PET uptake in the brain reveals distinct patterns of hypometabolism indicative of MCI. Understanding these changes may improve clinical diagnosis and prediction of disease progression. Areas of ^{18}F-florbetapir uptake did not overlap with regions of hypometabolism, indicating that the two radiotracers detect distinct pathologies occurring in MCI. Further research is warranted to determine the clinical efficacy of ^{18}F-FDG and ^{18}F-florbetapir PET in the early detection and management of MCI.

Acknowledgements

The authors thank the study coordinators for their valuable contributions.

Bibliography

1. Petersen RC. Mild Cognitive Impairment. *Continuum (Minneap Minn)* 2016; 22 (2 Dementia): 404-18.
2. Petersen R. C. Clinical practice: Mild cognitive impairment. *N Engl J Med* 2011; 364(23): 2227-34.
3. Mosconi L. Brain glucose metabolism in the early and specific diagnosis of Alzheimer's disease. ^{18}F-FDG-PET studies in MCI and AD. *Eur J Nucl Med Mol Imaging* 2005; 32(4): 486-510.
4. Barthel H, Sabri O. Clinical use and utility of amyloid imaging. *J Nucl Med* 2017; 58(11): 1711-7.
5. Tripathi M, Tripathi M, Sharma R et al. Functional neuroimaging using ^{18}F-FDG PET/CT in amnestic mild cognitive impairment: A preliminary study. *Indian J Nucl Med* 2013; 28(3): 129-33.
6. Cera N, Esposito R, Cieri F, Tartaro A. Altered Cingulate Cortex Functional Connectivity in Normal Aging and Mild Cognitive Impairment. *Front Neurosci* 2019; 13: 857.
7. Gluhm S, Goldstein J, Loc K et al. Cognitive performance on the mini-mental state examination and the montreal cognitive assessment across the healthy adult lifespan. *Cogn Behav Neurol* 2013; 26(1): 1-5.
8. Perini G, Rodriguez-Vieitez E, Kadir A et al. Clinical impact of ^{18}F-FDG-PET among memory clinic patients with uncertain diagnosis. *Eur J Nucl Med Mol Imaging* 2021; 48(2): 612-22.
9. Nguyen JC, Killcross AS, Jenkins TA. Obesity and cognitive decline: role of inflammation and vascular changes. *Front Neurosci* 2014; 8: 375.
10. Petersen RC, Smith GE, Ivnik RJ et al. Apolipoprotein E status as a predictor of the development of Alzheimer's disease in memory-impaired individuals. JAMA 1995; 273(16): 1274-8. Erratum in: *JAMA* 1995; 274(7): 538.
11. Berg L. Clinical Dementia Rating. *Br J Psychiatry* 1984; 145: 339.
12. Langbaum JBS, Chen K, Lee W et al. Alzheimer's Disease Neuroimaging Initiative Categorical and correlational analyses of baseline fluorodeoxyglucose positron emission tomography images from the Alzheimer's Disease Neuroimaging Initiative (ADNI). *Neuroimage* 2010; 45: 1107-16.
13. Clark CM, Schneider JA, Bedell BJ et al. Use of florbetapir-PET for imaging beta-amyloid pathology. *JAMA* 2011; 305: 275-83.
14. Molloy DW, Standish TI, Lewis DL. Screening for mild cognitive impairment: comparing the SMMSE and the ABCS. *Can J Psychiatry* 2005; 50(1): 52-8.
15. Jia X, Wang Z, Huang F et al. A comparison of the Mini-Mental State Examination (MMSE) with the Montreal Cognitive Assessment (MoCA) for mild cognitive impairment screening in Chinese middle-aged and older population: a cross-sectional study. *BMC Psychiatry* 2021; 21(1): 485.
16. Zhuang L, Yang Y, Gao J. Cognitive assessment tools for mild cognitive impairment screening. *J Neurol* 2021; 268(5): 1615-22.
17. Leech R, Sharp DJ. The role of the posterior cingulate cortex in cognition and disease. *Brain* 2014; 137(Pt 1): 12-32.
18. Mosconi L. Glucose metabolism in normal aging and Alzheimer's disease: Methodological and physiological considerations for PET studies. *Clin Transl Imaging* 2013; 1(4): 10.1007/s40336-013-0026-y.
19. Drzezga A, Grimmer T, Riemenschneider M et al. Prediction of individual clinical outcome in MCI by means of genetic assessment and ^{18}F-FDG PET. *J Nucl Med* 2005; 46: 1625-32.
20. Minoshima S, Giordani B, Berent S et al. Metabolic reduction in the posterior cingulate cortex in very early Alzheimer's disease. *Ann Neurol* 1997; 42: 85-94.
21. Silverman DH, Small GW, Chang CY et al. Positron emission tomography in evaluation of dementia: Regional brain metabolism and long-term outcome. *JAMA* 2001; 286(17): 2120-7.
22. Nobili F, De Carli F, Frisoni GB et al. (2009) SPECT predictors of cognitive decline and Alzheimer's disease in mild cognitive impairment. *J Alzheimers Dis* 2009; 17: 761-72.
23. Chételat G, Desgranges B, de la Sayette V et al. Mild cognitive impairment: Can ^{18}F-FDG-PET predict who is to rapidly convert to Alzheimer's disease? *Neurology* 2003; 60(8): 1374-7.
24. Nestor PJ, Fryer TD, Smielewski P, Hodges JR. Limbic hypometabolism in Alzheimer's disease and mild cognitive impairment. *Ann Neurol* 2003; 54: 343-51.
25. Uecker A. (2014). Developmental neuropsychology. In *Elsevier eBooks*.
26. Small GW, Ercoli LM, Silverman DH et al. Cerebral metabolic and cognitive decline in persons at genetic risk for Alzheimer's disease. *Proc Natl Acad Sci USA* 2000; 97: 6037-42.
27. Reiman EM, Caselli RJ, Chen K et al. Converting brain activity in cognitively normal apolipoprotein E epsilon 4 heterozygotes: a foundation for using positron emission tomography to efficiently test treatments to prevent Alzheimer's disease. *Proc Natl Acad Sci USA* 2001; 98: 3334-9.
28. de Leon MJ, Convit A, Wolf OT et al. Prediction of cognitive decline in normal elderly subjects with 2-[(^{18}F]-fluoro-deoxy-D-glucose/positron-emission tomography (FDG/PET). *Proc Natl Acad Sci USA* 2001; 98: 10966-71.
29. Mosconi L, Perani D, Sorbi S et al. MCI conversion to dementia and the APOE genotype: a prediction study with ^{18}F-FDG-PET. *Neurology* 2004; 63(12): 2332-40.
30. Rosenberg PB, Wong DF, Edell SL et al. Cognition and amyloid load in Alzheimer disease imaged with florbetapir ^{18}F (AV-45) positron emission tomography. *Am J Geriatr Psychiatry* 2013; 21(3): 272-8.
31. Bao W, Xie F, Zuo C et al. PET Neuroimaging of Alzheimer's Disease: Radiotracers and Their Utility in Clinical Research. *Front Aging Neurosci* 2021; 13: 624330.
32. Khosravi M, Peter J, Wintering NA et al. ^{18}F-FDG Is a Superior Indicator of Cognitive Performance Compared to ^{18}F-Florbetapir in Alzheimer's Disease and Mild Cognitive Impairment Evaluation: A Global Quantitative Analysis. *J Alzheimers Dis* 2019; 70(4): 1197-207.
33. Baker-Nigh A, Vahedi S, Davis EG et al. Neuronal amyloid-β accumulation within cholinergic basal forebrain in ageing and Alzheimer's disease. *Brain* 2015; 138(Pt 6): 1722-37.

The role of splenic scintigraphy in the diagnosis of thoracic nodules

Hamdi Afşin[1] MD,
Emine Afsin[2] MD,
Billur Çalışkan[1] MD

1. Department of Nuclear Medicine, AbantIzzetBaysal University, Bolu, Turkey
2. Department of Chest Diseases, AbantIzzetBaysal University, Bolu, Turkey

Keywords: Splenic scintigraphy
- Thoracic nodules
- Thoracic splenosis - Splenectomy

Corresponding author:
EmineAfsin MD,
Department of Chest Diseases,
AbantIzzetBaysal University, Bolu,
Turkey
Phone: +903742534656
emineafsin@yahoo.com

Received:
2 February 2025
Accepted revised:
4 Jul 2025

Abstract

Thoracic splenosis is the presence of acquired ectopic splenic tissue within the thoracic cavity, typically following thoracoabdominal trauma or surgery. It is mostly asymptomatic and detected incidentally on radiography or tomography. A 64-year-old man was admitted with exertional dyspnea without any other respiratory complaints. The patient had a history of diabetes mellitus and hypertension and had undergone bilateral lung surgery and splenectomy due to a traffic accident 30 years ago. Thoracic computed tomograph (CT) revealed an 11x7mm nodular lesion in the posterobasal lower lobe of the left lung, multiple millimetric nodular lesions in the pleura corresponding to the left lung operation site, a focal defect in the right diaphragm, and liver herniation in this area. The diagnosis of 'thoracic splenosis' was made by splenic scintigraphy.

Hell J Nucl Med 2025; 28(2): 173-175 *Epub ahead of print: 4 August 2025* *Published online: 30 August 2025*

Introduction

A 64-year-old male presented to our outpatient clinic with chronic exertional dyspnea. The patient was a non-smoker and reported no additional respiratory or cardiac symptoms. His medical history included diabetes mellitus and hypertension. He also had a history of bilateral lung surgery and splenectomy following a traffic accident 30 years ago. There was no family history of malignancy, nor did the patient report asbestos exposure. His physical examination was unremarkable, and respiratory function tests were within normal limits. Thoracic computed tomography (CT) revealed an 11 ×7mm nodular lesion in the posterobasal segment of the left lower lobe, multiple millimetric nodules in the pleura near the site of the left lung operation, a focal defect in the right diaphragm, and herniation of the liver through this defect. The absence of malignancy-related symptoms, a family history of cancer, or smoking history, combined with the patient's splenectomy, raised the suspicion of thoracic splenosis. Spleen scintigraphy and single photon emission computed tomography (SPECT) imaging using heat-denatured erythrocyte-labeled technetium-99m (^{99m}Tc) confirmed the diagnosis. The imaging showed intense fusiform activity uptake extending vertically across 3-4 rib spaces at the upper ribs on the posterolateral side of the left chest wall and focal activity in 3-4 areas in the splenic region. Based on these findings, the patient was diagnosed with thoracic splenosis and placed under follow-up care.

Thoracic splenosis is the presence of acquired ectopic splenic tissue within the thoracic cavity, typically following thoracoabdominal trauma or surgery. It is mostly asymptomatic and detected incidentally on radiography or tomography. The mean interval between trauma and detection of thoracic splenosis is 21 years, ranging from 3 to 45 years [1].

Intrathoracic splenosis develops with the simultaneous rupture of the diaphragm and spleen, migration of splenic tissue into the hemithorax, and proliferation on the serous surface of the pleura [2]. Splenic implants are usually observed as benign, round, smooth, sessile pleural-based nodules in the left hemithorax [3]. On CT, the attenuation of the lesions resembles the normal splenic appearance. Scintigraphic imaging techniques, such as those using indium-111 labeled platelets, denatured erythrocytes, or ^{99m}Tc labeled sulfur colloid, are effective for detecting ectopic splenic tissue, including splenosis and accessory spleens. Among these, splenic scintigraphy with ^{99m}Tc labeled denatured erythrocytes is commonly favored due to its greater availability compared to indium-111 [4].

Following the administration of the radiopharmaceutical, ^{99m}Tc labeled denatured erythrocytes are selectively sequestered by splenic tissue, allowing for a highly accurate and specific diagnosis [5]. Single photon emission computed tomography or hybrid SPECT/CT imaging, when used alongside planar imaging, reduces activity overlap seen in planar images and offers additional three-dimensional cross-sectional localization of the focus [4]. In our case, to aid in the differential diagnosis of suspicious nodular lesions detected on thoracic CT scans, we performed SPECT imaging at our institution. The scintigraphic planar images and SPECT images were compared with the thoracic CT images for interpretation.

In cases of pleural nodules, a history of thoracoabdominal trauma or surgery should raise suspicion for a diagnosis of thoracic splenosis. Confirming the diagnosis through splenic scintigraphy can prevent the patient from undergoing unnecessary biopsies or surgeries, along with the associated risks and complications [6]. Additionally, it is important to note that thoracic splenosis carries a high risk of bleeding during surgical procedures due to the presence of functional splenic tissue lesions [7].

Thoracicsplenosis is usually a slow-growing and non-invasive condition. If splenic tissue is large, it may lead to symptoms such as shortness of breath, hemoptysis, and chest pain. Asymptomatic surgical resection is generally not recommended. In splenosis, splenic tissue is active and receives blood from surrounding tissues, potentially contributing to immune defense.

The authors declare that they have no conflicts of interest.

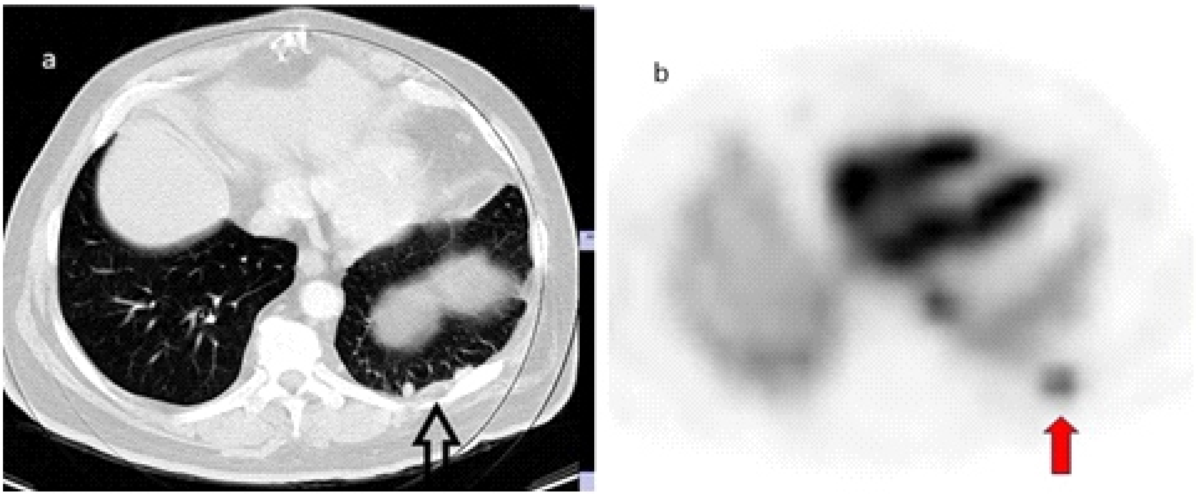

Figure 1. a) Thoracic CT shows a multiple nodular lesion measuring 11×7mm in the pleura adjacent to the posterobasal segment of the left lower lobe of the lung (arrow). b) Selective spleen scintigraphy SPECT transaxial section reveals focal activity (red arrow) beneath the costal margin, located in the pleura adjacent to the posterobasal segment of the left lower lung lobe.

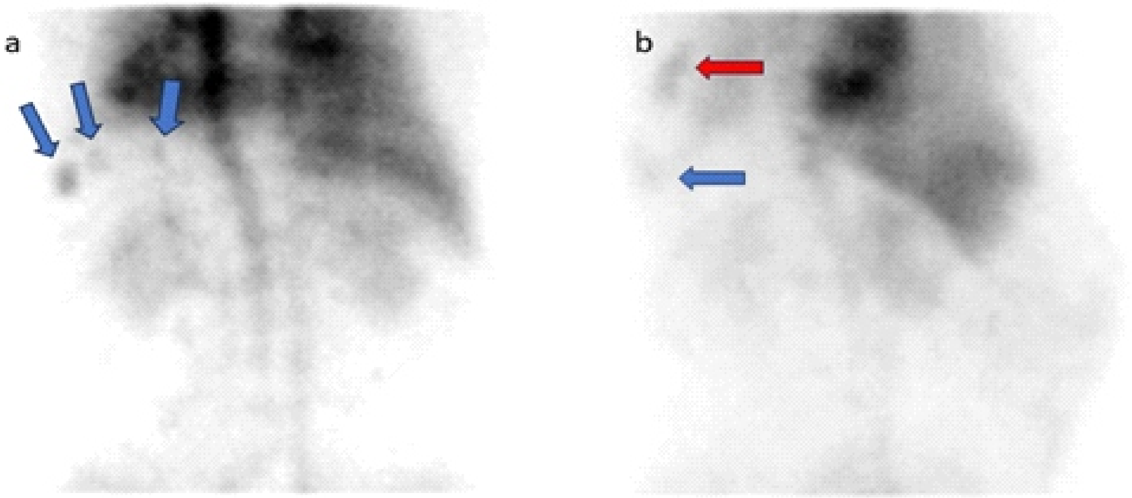

Figure 2. Selective spleen scintigraphy using heat-denatured erythrocyte-labeled technetium-99m: a) Posterior planar image shows focal activity uptake in three distinct foci within the splenic region (blue arrows). b) Lateral planar image reveals fusiform activity uptake extending vertically across 3-4 rib spaces beneath the pleura adjacent to the posterolateral segment of the left chest wall (red arrow) and focal activity uptake in the splenic region (blue arrow).

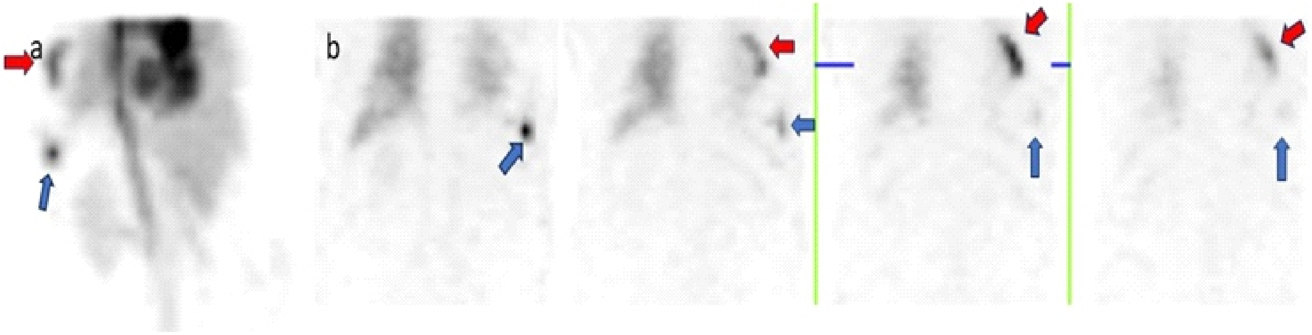

Figure 3. Selective spleen scintigraphy SPECT images using heat-denatured erythrocyte-labeled technetium-99m: a)Posterolateral image. b) Coronal view across four consecutive slices shows fusiform activity uptake (red arrow) extending vertically over 3-4 rib spaces beneath the pleura adjacent to the posterolateral segment of the left chest wall, along with focal activity uptake (blue arrow) in the splenic region.

Bibliography

1. Yammine JN, Yatim A, Barbari A. Radionuclide imaging in thoracic splenosis and a review of the literature. *Clin Nucl Med* 2003; 28: 121-3.
2. Alaraj AM, Chamoun RB, Dahdaleh NS et al. Thoracic splenosis mimicking thoracic schwannoma: case report and review of the literature. *Surg Neurol* 2005; 64:185-8; discussion 188.
3. Malik UF, Martin MR, Patel R et al. Parenchymal thoracic splenosis: history and nuclear imaging without invasive procedures may provide diagnosis. *J ClinMed Res* 2010; 2: 180.
4. Yavuz H, Tamer F, Çinkooğlu A et al. A case of thoracic splenosis diagnosed with spleen scintigraphy. *Res Case Rep* 2023; 12(1): 15-8.
5. Williams G, Rosen MP, Parker JA et al. Splenic implants detected by SPECT images of Tc-99m labeled damaged red blood cells. *Clin Nucl Med* 2006; 31(8): 467-9.
6. Chen J, Russo R, Yung G et al. False positive metastatic disease due to combined thoracic and subcutaneous splenosis. *Radiol Case Rep* 2023; 19: 872-5.
7. Harb N, Fattore J, Saththianathan M et al. Thoracic splenosis: Precision medicine can prevent thoracic surgery. *Respirol Case Rep* 2024; 12(11): e70067.

Usefulness and reliability of ^{131}I-6-β-iodomethyl- nor cholesterol (NP-59), adrenal cortex scintigraphy in discrimination between adenoma and hyperplasia in case of a patient with primary hyperaldosteronism (PH) without discontinuation of antihypertension therapy

Evangelos Karathanos[1] PhD,
Irini Giagourta[2] MD,
Agaristi Kaspiri[3] MD

1. Department of Nuclear Medicine, Sotiria Hospital, Athens Greece
2. Department of Endocrinology, Gennimatas Hospital, Athens Greece
3. Department of Nuclear Medicine, University Hospital, Ioannina, Greece

Abstract

Clear iodine-131 (^{131}I)-6-β-iodomethyl- norcholesterol aldosterinoma finding, proven on biopsy, without prior discontinuation of spironolactone (due to high blood pressure) reveals no changes on scintigraphic sensitivity

Hell J Nucl Med 2025; 28(2): 176-180

Keywords: Adrenal cortex scintigraphy
- Primary hyperaldosteronism
- Adenoma - Spironolactone

Corresponding author:
Evangelos Karathanos PhD,
Department of Nuclear Medicine,
Sotiria Hospital, Athens Greece
Mob: +30 6934439443
karathanos@yahoo.com

Received:
23 Apr 2025
Accepted revised:
15 May 2025

Case Report

An abdominal computed tomography (CT) performed on a 72 years old woman with a long history of stable hypertension (over 22 years), revealed incidentally 3 adrenal masses characterized as benign adenomas. (Two on the left adrenal gland of 2.2cm and 18cm in diameter and 1 on the right of 18cm, respectively) (Figure 1).

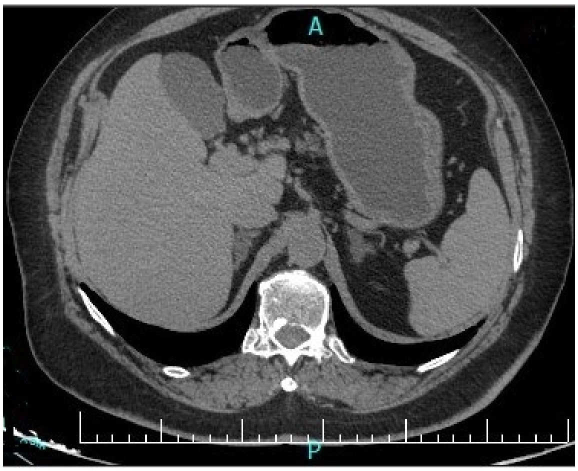

Figure 1. Abdominal CT findings: benign adenomas on both adrenal glands.

Despite multiple antihypertensive regimens, blood pressure (measuring at physician's office and at home) was consistently high and above target (<140/90mm Hg). Treatment with perindopril (10mg), amlodipine (2.5mg), indapamide (5mg), monoxidine (0.6mg/day), nebivolol 5mg/day and spironolactone (25mg) was followed. On physical examination, body weight was measured at 97kg, height at 170cm, (Body mass index: 33.6kg/m^2), blood pressure at 180/102mmHg and heart rate at 83bpm (supine position). Systemic findings were normal. Serum electrolytes showed severe hypokalemia (K^+: 2.3mEq/L). Twenty four-hour urinary potassium values were elevated (K^+: 36.40mEq/24h, Na^+: 83.2 mEq/24h). Due to persistent hypokalemia, intravenously and orally K^+ was added and spironolactone dose was increased. Complete blood count, liver and renal function tests and basal adrenocorticotropic hormone (ACTH) and cortisol levels were normal. Aldosterone baseline values were high (1217pmol/L), renin values were low (renin 5.1pg/mL), leading to a high baseline aldosterone to renin ratio (ARR): 132. Overnight dexamethasone test (2mg) was strongly suspicious for autonomous cortisol secretion (cortisol: 62.2nmol/L radioimmunoassay (RIA) {10-60nmol/L} and ACTH <5pg/mL). Due to chronic elevated blood pressure, renin-angiotensin- aldosterone axis test was not performed, as it would be dangerous to discontinue anti-hypertension drug therapy. However, PH was considered, based on the combination of adrenal glands adenomas, severe hypertension with hypokalemia, high aldosterone levels and high aldosterone-renin (ARR) ratio. In order to discriminate adrenal adenoma from hyperplasia, NP-59 scintigraphy was performed under the following technique: To protect thyroid gland against iodine-131 (^{131}I) radioactivity, the patient was encouraged for oral administration of lugol solution (3x3 drops daily) 2 days before, up to 7 days after the radiopharmaceutical i.v. injection. As it was unable to control blood pressure, scintigraphy was carried out without discontinuation or modification of high spironolactone dose (200 mg/day). A dexamethasone-suppression protocol was implemented (4mg/day divided in 4 doses, beginning 7 days before i.v. injection) as inhibition of ACTH secretion is crucial for best imaging discrimination between adenoma and hyperplasia in case of PH. Thirty seven MBq (1mCi) of NP-59, were slowly (over 30sec) injected i.v. One day before imaging, the patient was told to empty the colon using a mild laxative, in order to avoid overlapping bowel activity. A dual head gamma camera equipped with high energy, parallel-hole collimator was used, and imaging (80KeV window centered around 364KeV) was carried out at 48h, 72h and 6 days p.i. (whole body, anterior/posterior abdomen planar of 50,000 counts) (Figure 2) and single photon emission computed tomography (SPECT) acquisition - step and shoot protocol, 2° orbit, 20sec/step, filter-back projection analysis. Because of bowel activity, relative low count rate and high energy photon of ^{131}I, SPECT summed images - by two - as well as cine-mode display were helpful for better visualization) (Figure 3). Prominent left adenoma was revealed, confirming left side aldosterinoma scintigraphic diagnosis. Late Imaging at 6th day was normal - as (often) expected (Figure 4).

According to scintigraphic findings and due to persistent hypertension, successful left adrenalectomy was carried out and biopsy revealed a typical adenoma (Figure 5). Two days later, blood pressure (130/80 mmHg) and serum K^+ (4.0mEq/L) returned to normal values.

Discussion

Although CT is a sensitive imaging modality in detecting adenomas, its sensitivity for bilateral hyperplasia is quite limited. Scintigraphy as a functional, non-invasive, and potentially

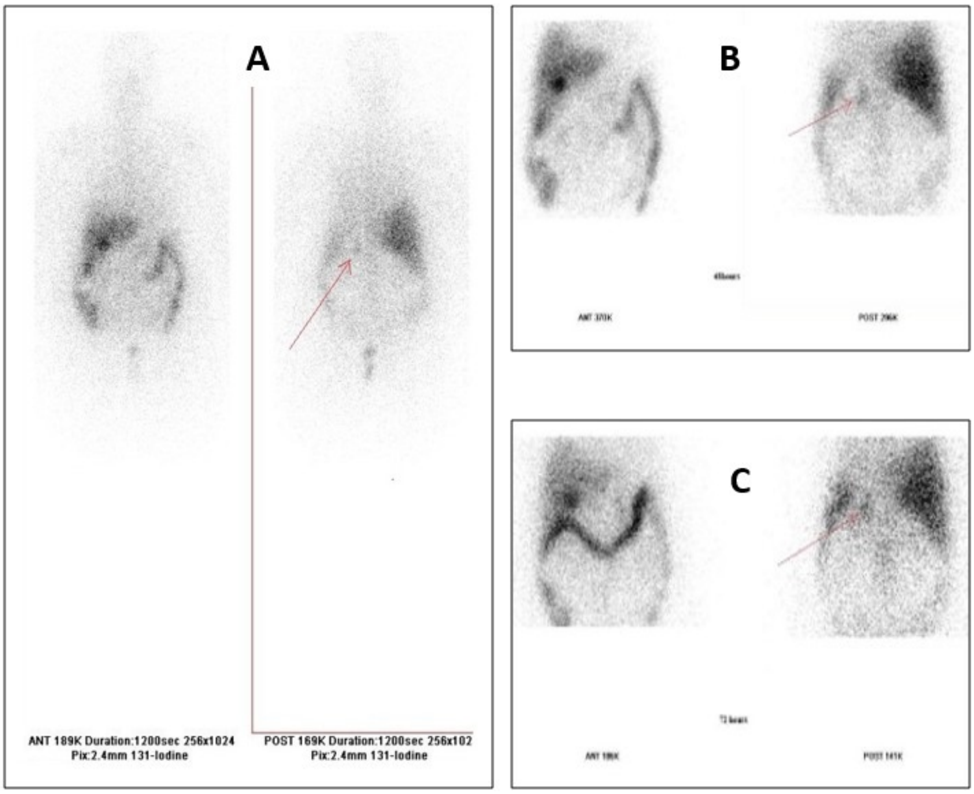

Figure 2. Whole body scintigraphy at 48h: Imaging of left adrenal cortex, at posterior view (arrow). Notice the intense hepatic uptake, the hot spot sign (gallbladder) at the Anterior view and the diffuse presence of radiopharmaceutical into the bowel (normal bio-distribution and enterohepatic excretion) (A). Planar acquisition at 48h (B) and 72 h (C): Left adrenal cortex best seen at posterior view (arrow).

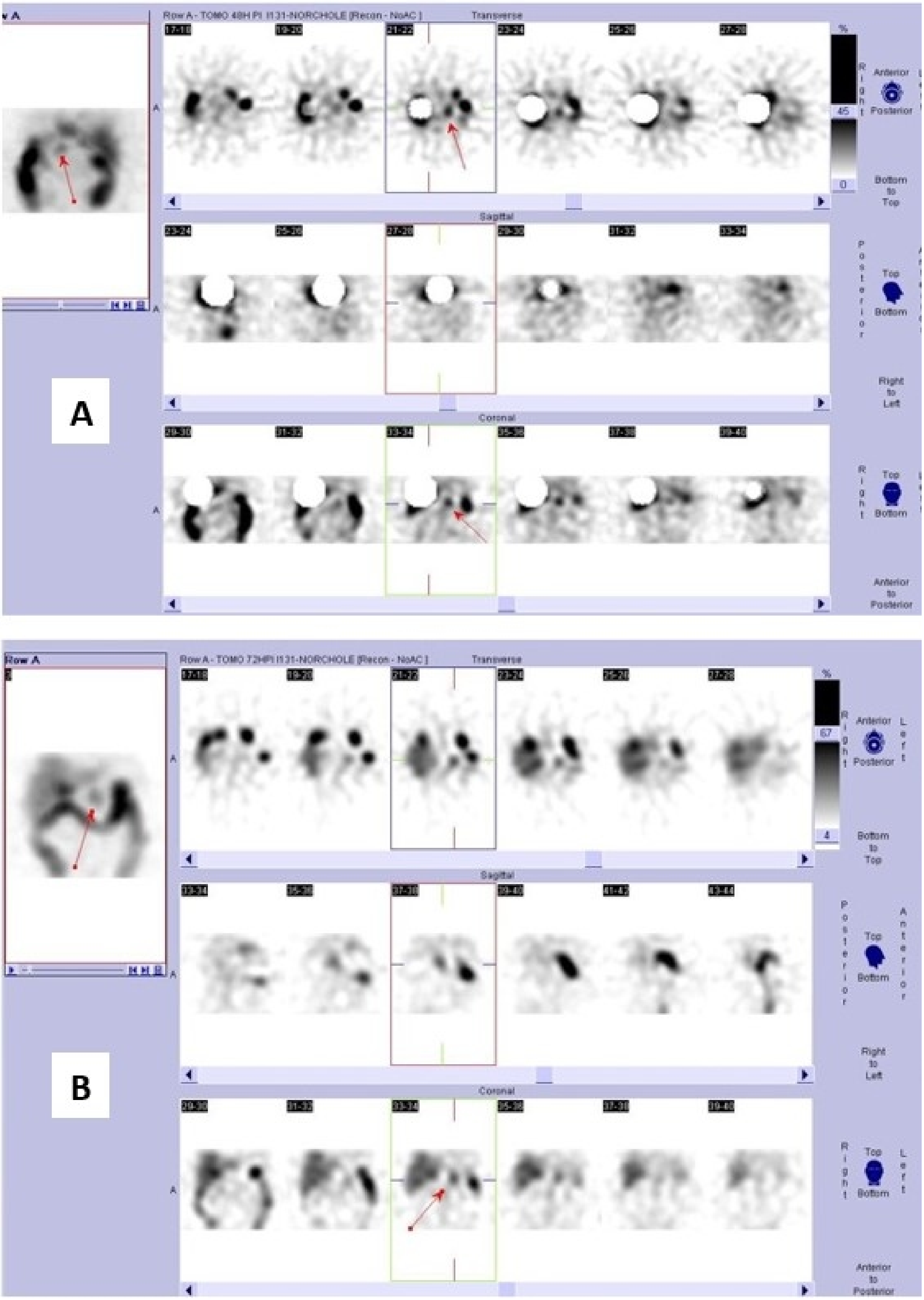

Figure 3. Single photon emission computed tomography at 48h (A): At transverse and coronal slices as well as at cine-mode snapshot (left outer image) the pointed hot spot sign (arrow) represents the visualized left adrenal cortex (adenoma). In order to enhance the contrast, partial masking of liver has been applied. Single photon emission computed tomography at 72h (B): At coronal slices as well as at cine-mode snapshot (left outer image), the pointed hot spot sign (arrow) represents the visualized left adrenal cortex (adenoma). Notice that gallbladder still remains visible, but comparing to SPECT imaging at 48h, left adrenal cortex (adenoma) is better seen, because of more fainted hepatic background. This justifies the value of late imaging, as well as that of SPECT acquisition in order to have an optimum imaging result (without underlying background, and/or normal overlapping structures – e.g. gallbladder).

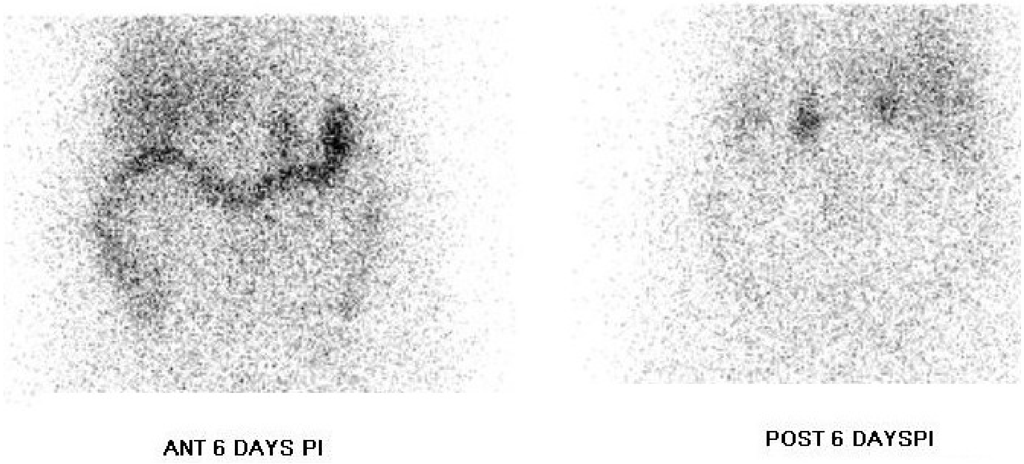

Figure 4. Planar imaging at 6th day: Bilateral visualisation of both adrenal glands (better seen on posterior image). After 5th day p.i. this is a normal finding (see Discussion). For PH under dexamethasone suppression, scintigraphic findings between 48h and 5th day confirm or not the presence of adenoma or hyperplasia.

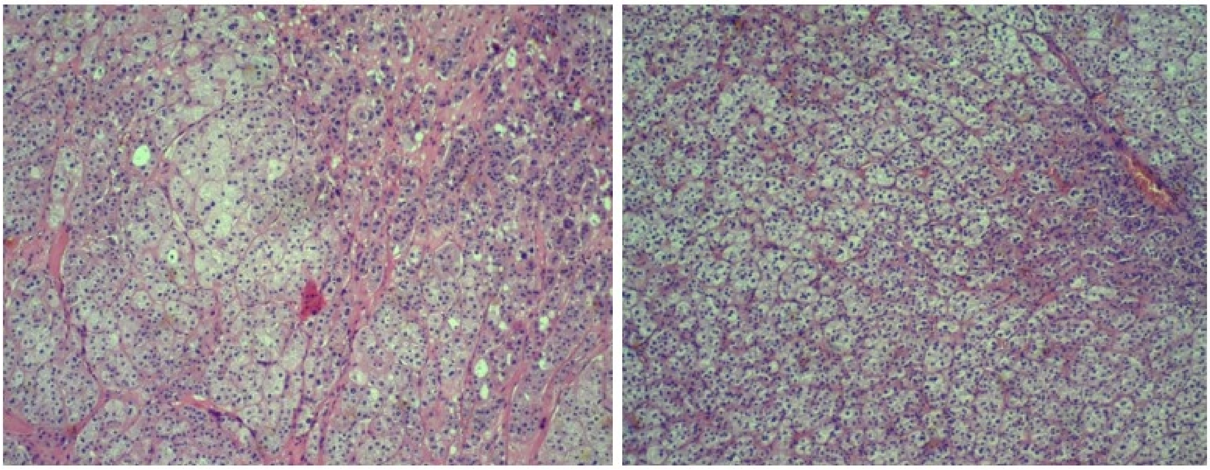

Figure 5. Microscopic appearance of adrenal adenoma hematoxylin/eosin staining (x50).

quantifiable method for adrenocortical imaging, is a safe and accurate imaging procedure for discrimination between adenoma and hyperplasia in case of PH [1-3]. Histologically, adrenal cortex consists of three distinct layers (zones): the outer or glomerulosa zone (for mineralocorticoid production, mainly aldosterone), the middle or fasciculata zone (for glucocorticoid production, mainly cortisol) and the inner or reticulata zone (for sex hormone production). Aldosterone biosynthesis is mediated by renin-angiotensin-aldosterone axis, and cholesterol (normally derived from low-density-lipoproteins - LDL) is the substrate for the above synthesis. The aforementioned biochemical pathway justifies the use of radiolabeled Cholesterol-analogues in order to depict adrenal cortex. So far, three radiopharmaceuticals have been widely used for adrenocortical scintigraphy: ^{131}I-19-iodocholesterol, ^{131}I-6-β-iodomethyl-norcholesterol (NP-59), and ^{75}Se-6-β-selenomethyl- norcholesterol. NP-59 has greater affinity (x5) for adrenocortical uptake, greater in vivo stability, less deiodination with diminished thyroid uptake of free ^{131}I than ^{131}I-19-iodocholesterol [4-7] and a relative lower absorbed radiation dose/injected mCi to adrenal cortex than the other two agents [3, 8]. Radiolabeled cholesterol-analogues are incorporated in LDL, enter adrenocortical cells, where esterification, (as it happens with native cholesterol) takes place, but are not further metabolized. Taken up by liver LDL receptors, these analogues are excreted to bile acid and subject enterohepatic circulation, leading to an increased background colonic radioactivity. To avoid overlapping activity, the use of a soft laxative is recommended one day before examination [4, 7, 8]. In case of PH, oral administration of dexamethasone suppresses the ACTH-dependent component of NP-59 uptake in the (middle) fasciculata zone, facilitating its uptake in the outer cortex layer, and hence, offering an accurate visualization of glomerulosa zone. Early unilateral adrenal visualization (before 5th day) suggests presence of a solidary adenoma, whereas early bilateral visualization (before 5th day) suggests bilateral hyperplasia. Late (after 5th day) adrenal visualization is a normal finding, although the same pattern has been found in some unusual cases of dexamethasone-suppressible hyperaldosteronism [4]. This advantage of NP-scintigraphy (compared to 75Se-6-β-selenomethyl - norcholesterol with longer half-life and hence possible later imaging pathologic findings -up to14 days) findings, makes NP-59 the agent choice for most nuclear medicine departments.

In our case, unilateral imaging of left adrenal adenoma was visualised early (3th and 4th day) whereas (as usually expected) at late imaging (6th day), both adrenals were well and equally depicted [10]. Before scintigraphy, patient preparation must take into account thyroid protection against ^{131}I, as well as factors that may deteriorate the final imaging result, interfering either with the axis (hypothalamic - pituitary -adrenal/renin-angiotensin-aldosterone) or with high cholesterol levels (unwanted competition with NP-59). So far, guidelines strongly suggest blockage of thyroid with potassium perchlorate and discontinuance of certain agents (e.g. spironolactone, ketoconazole, diuretics, oral contraceptives, etc.) in order to achieve optimum NP-59 uptake [1]. If any of the above agents (e.g. spironolactone) are essential for blood pressure control, then the discontinuation decision is up to the clinician team and Scintigraphy can be carried out with potentially reduced sensitivity. Chia-Hui Chang et al. (2018) studied a cohort of 34 patients with PH without discontinuation or modification of antihypertensive medication, and concluded that NP-59 scintigraphy provide safe and accurate lateralization of the lesion [9]. Following the same method, NP-59 scintigraphy of the presented case was done under spironolactone treatment (as it was crucial for blood pressure control) and the final result (unilateral intense imaging), not only justified our choice, but also served as a hallmark for left adrenal gland surgical removal, leading impressively to blood pressure improvement. In conclusion, NP-59 adrenal cortex scintigraphy, remains a reliable and useful tool in depicting adenomas in case of PH, without the need of spironolactone cessation.

Bibliography

1. Rubello D, Bui C, Casara D et al. Functional scintigraphy of adrenal gland. Review. *Eur J Endocrinol* 2002; 147: 13-28
2. Gross MD, Falke THM, Shapiro B. Adrenal glands. Endocrine Imaging pp 271-349, Eds MD Sandler, JA Patton, MD Gross, B Shapiro &THM Falke, Connecticut: Appleton & Lange, 1992.
3. Shapiro B, Fig LM, Gross MD, Khafagi F. Radiochemical diagnosis of adrenal disease. *Crit Rev Clin Lab Sci* 1989; 27(3): 265-98.
4. Avram AM, Fig LM, Gross MD. Adrenal gland scintigraphy. *Semin Nucl Med 2006*; 36(3): 212-27.
5. Sarkar SD, Beierwaltes H, Ice RD et al. A new and superior adrenal scanning agent, NP-59. *J Nucl Med* 1975; 16(11): 1038-42.
6. Thrall JH, Freitas JE, Beierwaltes WH. Adrenal scintigraphy. *Semin Nucl Med* 1978; 8(1): 23-41.
7. Freitas JE. Adrenal cortical and medullary imaging. *Semin Nucl Med* 1995; 25: 235-50.
8. Lynn M D, Gross M D, Shapiro B. Enterohepatic circulation and distribution of I-131-6-iodomethyl-19-norcholesterol (NP-59). *Nucl Med Comm* 1986; 7: 625-30.
9. Chang CH, Yang SS, Tsai YC et al. Surgical outcomes of patients with primary aldosteronism lateralized with I-131-6 β-iodomethyl-norcholesterol single photon emission/computed tomography without discontinuation or modification of antihypertensive medications. *Tzu Chi Med J* 2018; 30(3): 169-75.
10. Spyridonidis TJ, Apostolopoulos DJ. Is there a role for Nuclear Medicine in diagnosis and management of patients with primary aldosteronism? *Hell J Nucl Med* 2013; 16(2): 134-9.

^{68}Ga-FAPI PET/CT for diagnosing multifocal head-neck and liver paragangliomas

Abstract

This report presents a case of a 51-year-old woman who was admitted to our hospital with incomplete closure of the left eyelid and a crooked right corner of the mouth. She was diagnosed with multifocal head-neck and liver paragangliomas that were confirmed by pathological tests and gallium-68-fibroblast activation protein inhibitor (^{68}Ga-FAPI) positron emission tomography/computed tomography (PET/CT) imaging. The findings of this case suggest that ^{68}Ga-FAPI PET/CT may be a potential diagnostic tool for paragangliomas.

Hell J Nucl Med 2025; 28(2): 181-182 *Epub ahead of print: 4 August 2025* *Published online: 30 August 2025*

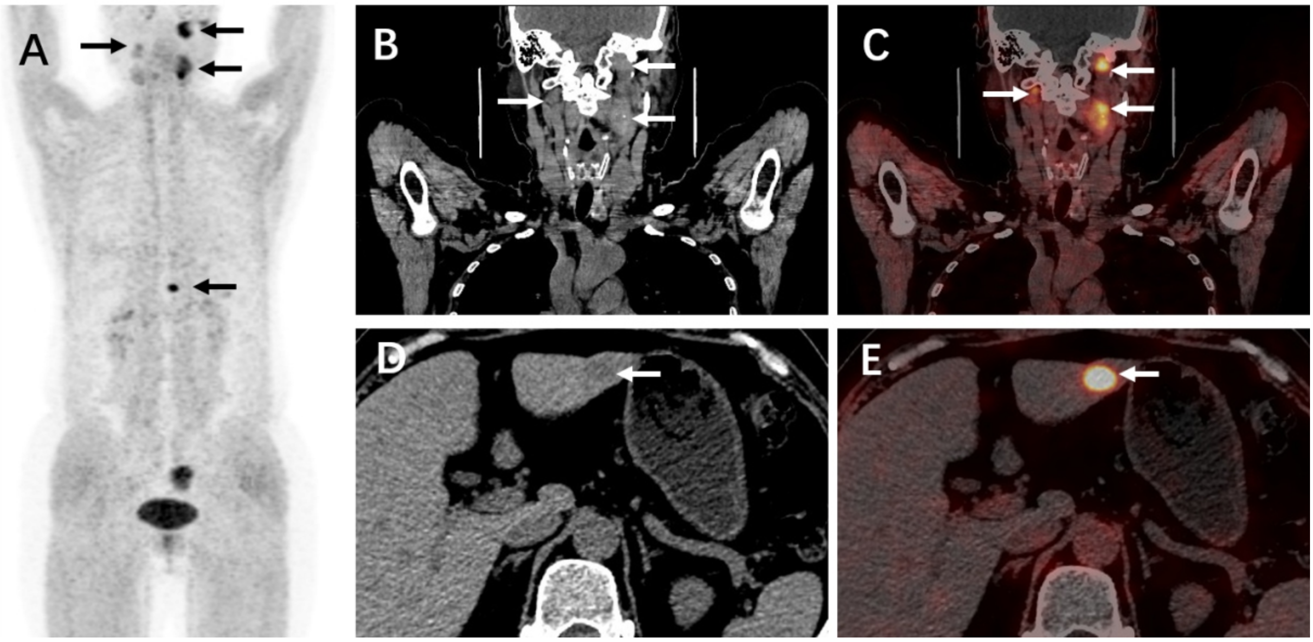

Figure 1. A 55-year-old woman was admitted to our hospital with incomplete closure of the left eyelid and crooked right corner of the mouth persisting for 7d. The catecholamine test results were negative. Enhanced computed tomography (CT) revealed soft tissue density nodules and mass in the left jugular foramen area (29×17mm), the bifurcation of the left common carotid artery (37×23mm), and the starting segment of the right internal carotid artery (18×16mm). All lesions exhibited significant enhancement and non-enhanced necrotic areas. A gallium-68-fibroblast activation protein inhibitor (^{68}Ga-FAPI) positron emission tomography (PET)/CT showed these three lesions with increased ^{68}Ga-FAPI uptake in the head and neck, as evident in the maximum intensity projection (MIP) image (A, black arrows in the head and neck), axial CT (B, white arrows) and PET/CT fusion imaging (C, white arrows) of the ^{68}Ga-FAPI PET/CT scan; the respective maximum standardized uptake values (SUVmax) values we-re 10.0, 9.7, and 4.4. These imaging techniques revealed a slightly low-density nodular with unclear boundaries and approximately 14×10mm in size (SUVmax: 10.3) (A, black arrow in the abdomen and D, E, white arrows). Subsequently, the patient underwent tumor resection surgery in the head, left neck, and liver; all tumors were patho-logically confirmed as paragangliomas. Additionally, although the lesion on the right neck was not removed surgically, we suspected it was a paraganglioma, based on en-hanced CT findings. Paragangliomas are pheochromocytomas located outside the adrenal gland, and are rare neuroendocrine tumors [1, 2]. The occurrence of multiple paragangliomas throughout the body is rare and is often associated with genetic mutations or inheritance [3]. Paragangliomas originating from the sympathetic nervous system are commonly found in the chest, abdominal, and pelvic cavities, and are often accompanied by an increase in catecholamines [4]. It is often discovered owing to symptoms such as paroxysmal hypertension, headache, palpitations, and sweating [5]. Paragangliomas originating from the parasympathetic nervous system are com-monly found in the skull base and neck, and usually do not produce catecholamines. Therefore, they are rarely detected based on symptoms of catecholamine excess. Para-gangliomas are usually revealed through the presence of neck masses or symptoms such as hearing loss, pulsatile tinnitus, dysphagia, and cerebral nerve paralysis caused by the compression or infiltration of adjacent structures [6, 7]. Primary paragangliomas of the liver are also relatively rare, with only approximately 13 cases reported so far [8]. Currently, previous literature suggests that single-photon emission CT/CT or PET/CT should be used to comprehensively evaluate the condition of patients with para-gangliomas. Commonly used imaging agents include iodine-123 (^{123}I)-metaiodobenzylguanidine, fluorine-18-fluorodeoxyglucose (^{18}F-FDG), 3,4-dihydroxy-6-[^{18}F]fluoro-l-phenylalanine, ^{68}Ga-dodecanetetraacetic acid, and somatostatin assay [1, 2, 9-11]. Currently, ^{68}Ga-FAPI is less commonly used for neuroendocrine tumors, including pa-ragangliomas [12]. In this case, ^{68}Ga-FAPI was used to comprehensively and accurately evaluate the patient's condition, highlighting the potential use of ^{68}Ga-FAPI as a pro-mising imaging agent for neuroendocrine tumors.

The authors declare that they Funding no conflicts of interest.

Funding

This study was supported by the construction project of Chongqing Key Clinical Specialty and Medical Science and Technology Innovation Center in Fuling District of Chongqing (Molecular Imaging Precision Medical Science and Technology Innovation Center in the East of Chongqing), Chongqing regional medical key discipline construction project (zdxk201920), Technology Innovation and Application Development Project of Science and Technology Bureau in Fuling District of Chongqing (FL KJ, 2022BAN2035), China.

Bibliography

1. Lenders JW, Duh QY, Eisenhofer G et al. Pheochromocytoma and paraganglioma: an endocrine society clinical practice guideline. *J Clin Endocrinol Metab* 2014; 99: 1915-42.
2. Lenders JWM, Kerstens MN, Amar L et al. Genetics, diagnosis, management and future directions of research of phaeochromocytoma and paraganglioma: a position statement and consensus of the Working Group on Endocrine Hypertension of the European Society of Hypertension. *J Hypertens* 2020; 38: 1443-56.
3. Kimura N, Takayanagi R, Takizawa N et al. Pathological grading for predicting metastasis in phaeochromocytoma and paraganglioma. *Endocr Relat Cancer* 2014; 21(3): 405-14.
4. DeLellis R, Lloyd R, Heitz P et al. Pathology and Genetics of Tumours of Endocrine Organs. Lyon, France: IARC Press 2004.
5. Lenders JWM, Kerstens MN, Amar L et al. Genetics, diagnosis, management and future directions of research of phaeochromocytoma and paraganglioma: a position statement and consensus of the Working Group on Endocrine Hypertension of the European Society of Hypertension. *J Hypertens* 2020; 38(8): 1443-56.
6. Williams MD, Tischler AS. Update from the 4th Edition of the World Health Organization Classification of Head and Neck Tumours: Paragangliomas. *Head Neck Pathol* 2017; 11: 88-95.
7. Taieb D, Kaliski A, Boedeker CC et al. Current approaches and recent developments in the management of head and neck paragangliomas. *Endocr Rev* 2014; 35: 795-819.
8. Vella I, De Carlis R, Lauterio A et al. Extremely rare presentation of primary nonfunctioning hepatic paraganglioma. *Dig Liver Dis* 2022; 54(6): 838-39.
9. Taïeb D, Wanna GB, Ahmad M et al. Clinical consensus guideline on the management of phaeochromocytoma and paraganglioma in patients harbouring germline SDHD pathogenic variants. *Lancet Diabetes Endo* 2023; 11(5): 345-61.
10. Taïeb D, Hicks RJ, Hindié E et al. European Association of Nuclear Medicine Practice Guideline/Society of Nuclear Medicine and Molecular Imaging procedure standard 2019 for radionuclide imaging of phaeochromocytoma and paraganglioma. *Eur J Nucl Med Mol Imaging* 2019; 46: 2112-37.
11. Amodru V, Guerin C, Delcourt S et al. Quantitative ^{18}F-DOPA PET/CT in pheochromocytoma: the relationship between tumor secretion and its biochemical phenotype. *Eur J Nucl Med Mol Imaging* 2018; 45: 278-82.
12. Kosmala A, Serfling SE, Schlötelburg W et al. Impact of ^{68}Ga-FAPI-04 PET/CT on Staging and Therapeutic Management in Patients With Digestive System Tumors. *Clin Nucl Med* 2023; 48(1): 35-42.

Jing Zhou[1*] MD, Longlan Chen[2*] MD, Ruyan Liu[3] MD, Yigang Zhao[1] MD

1. Department of Nuclear Medicine, Chongqing University Fuling Hospital, No. 2 Gaosuntang Road, Fuling District, Chongqing 408000, People's Republic of China. 2. Department of Nuclear Medicine, Chongqing University Cancer Hospital, No. 181 HanYu St, Shapingba District, Chongqing 400030, People's Republic of China. 3. Department of Radiotherapy, Chongqing University Fuling Hospital, No. 2 Gaosuntang Road, Fuling District, Chongqing 408000, People's Republic of China.

Corresponding author: *Ruyan Liu MD, Department of Radiotherapy, Chongqing University Fuling Hospital, No. 2 Gaosuntang Road, Fuling District, Chongqing 408000, People's Republic of China. E-mail: 277472539@qq.com. Yigang Zhao MD, Department of Nuclear Medicine, Chongqing University Fuling Hospital, No. 2 Gaosuntang Road, Fuling District, Chongqing 408000, People's Republic of China. Email: hyxkzyg@163.com*

Gastric signet ring cell carcinoma with ureteral metastasis as the first manifestation detected by ^{68}Ga-FAPI PET/CT

Hell J Nucl Med 2025; 28(2): 183-184 *Epub ahead of print: 4 August 2025* *Published online: 30 August 2025*

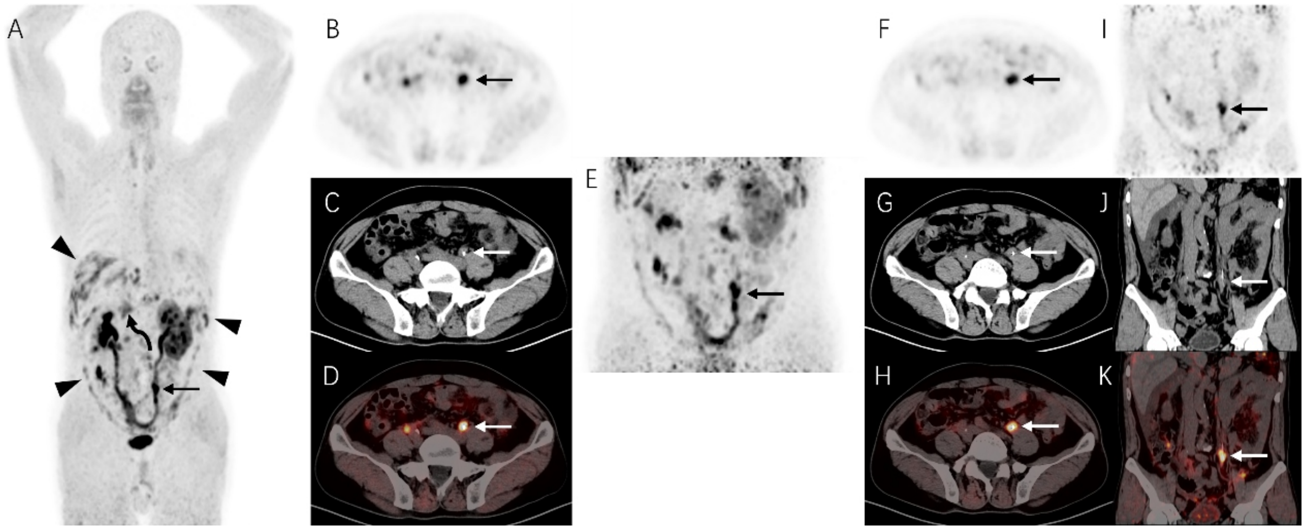

Figure 1. A 55-year-old man was admitted to the hospital due to left back pain for 2 weeks. Enhanced abdominal computed tomography (CT) suggested inhomogeneous thickening of the left ureteral wall with obvious enhancement, as well as peritoneal thickening, which suggested the possibility of left ureteral malignancy with peritoneal metastasis. However, the ureteroscopic biopsy was suggestive of signet ring cell carcinoma. With the consent of the patient, we enrolled him in a clinical trial of gallium-68-labeled fibroblast activation protein inhibitor 4 (^{68}Ga-FAPI-04) study in tumors. The maximum intensity projection (MIP) (A) and axial images (B-D) revealed increased FAPI uptake in the left ureteral wall (solid arrows; maximum standardized uptake value (SUVmax) of 14.1). Delayed images (E) after furosemide (intravenous injection, 10 mg) showed a clearer display of left ureteral lesion (solid arrows; SUVmax of 14.3) with less urinary impact (F-H: axial images; I-K: sagittal images). In addition, multiple thickenings of the peritoneum showed increased FAPI uptake (arrowheads; SUVmax of 13.8). Furthermore, a focus of elevated activity in the middle abdomen (curved arrows) was also noted on the MIP image.

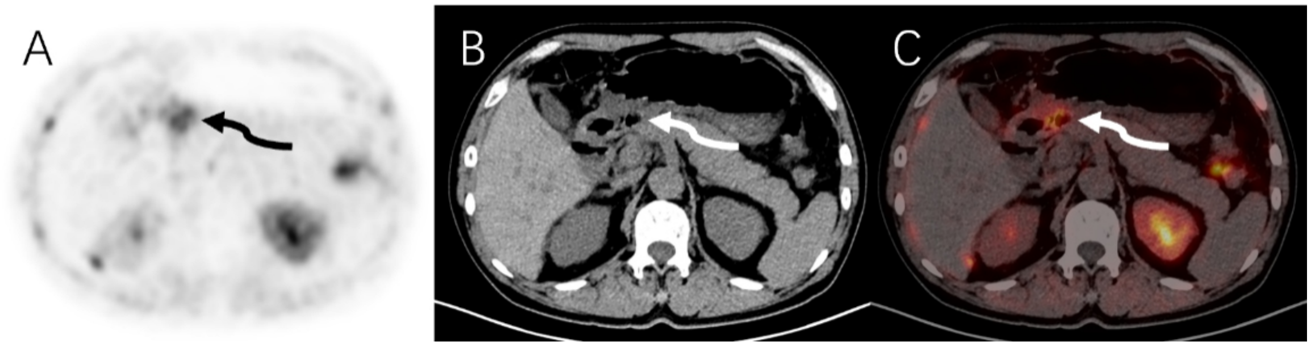

Figure 2. On the selected axial images of abdomen (A-C) (left, positron emission tomography (PET); middle, CT; right, fusion image), the activity (curved arrows) corresponded to the thickened gastric wall at the gastric antrum (SUVmax of 6.9). Based on the PET/CT findings, gastric cancer with peritoneal and ureteral metastases was suspected. Subsequent gastroscopy showed an ulcer in the gastric antrum. Finally, the pathologic diagnosis was a gastric signet ring cell carcinoma (GSRCC). Gastric signet ring cell carcinoma is a poorly cohesive pathological type of gastric cancer, has a poor prognosis [1]. It is very rare for GSRCC metastasize to the ureter as the first manifestation, and it is very difficult to distinguish from primary ureteral tumors. It is well known that fluorine-18-fluorodeoxyglucose (^{18}F-FDG) uptake is low in GSRCC, leading to misinterpretation of lesions in sometimes [2]. Studies have shown ^{68}Ga -FAPI PET/CT to be a promising imaging modality for the detection of primary and metastatic disease in GSRCC[3]. Our case demonstrates that for metastatic signet ring cell carcinoma, ^{68}Ga-FAPI might be helpful in finding the primary lesion. In addition, delayed imaging is also helpful in the detection of ureteral lesions.

The authors declare that they have no conflicts of interest.

Bibliography

1 Erickson LA. Gastric Signet Ring Cell Carcinoma. *Mayo Clin Proc* 2017; 92: e95-e6.

2. Dondi F, Albano D, Giubbini R, Bertagna F. ^{18}F-FDG PET and PET/CT for the evaluation of gastric signet ring cell carcinoma: a systematic review. *Nucl Med Commun* 2021; 42: 1293-300.

3. Beyhan E, Cermik TF, Erol Fenercioglu O et al. The Contribution of ^{68}Ga-FAPI-04 PET/CT to Staging and Prognosis in Gastric Cancer. *Clin Nucl Med* 2024; 49: e485-e91.

Yuhong Liu[1] MD, Jia Deng[2,3,4,5] MD, PhD, Yue Chen[2,3,4,5] MD, Huipan Liu[2,3,4,5*] MD, PhD, Jianwen Zhang[1*] MD

1. Department of Oncology, Affiliated Hospital of Southwest Medical University, 2. Department of Nuclear Medicine, Affiliated Hospital of Southwest Medical University, 3. Nuclear Medicine and Molecular Imaging Key Laboratory of Sichuan Province, 4. Laboratory for Targeted Radiopharmaceuticals Creation, 5. Institute of Nuclear Medicine, Southwest Medical University, No. 25, Taiping St., Luzhou, Sichuan, PR China. 646000

***Corresponding author:** Huipan Liu, MD, PhD and Jianwen Zhang MD, The Affiliated Hospital, Southwest Medical University, No. 25 TaiPing St, Jiangyang District, Luzhou, Sichuan, PR China. 646000. Tel: +86-830-3165722. E-mail of Huipan Liu: liuhuipan1573@163.com. E-mail of Jianwen Zhang: zhangjianwen66@126.com*